Rules for the Design of Patchy Particles using Self-Assembled Monolayers

by

Inés C. Pons-Siepermann

A dissertation submitted in partial fulfillment
of the requirements for the degree of
Doctor of Philosophy
(Chemical Engineering)
in the University of Michigan
2013

Doctoral Committee:
Professor Sharon C. Glotzer, Chair
Professor Nicholas A. Kotov
Professor Ronald G. Larson
Assistant Professor Anish Tuteja

Acknowledgments

I thank my advisor Prof. Sharon Glotzer for her support during these past five years. She provided me with all the resources I could have asked for, including financial support and the opportunity to attend many conferences and seminars. Her great advice and ideas were not only pivotal for my development as a researcher, but also an inspiration for my work with student organizations like SWE and ASEE.

I would also like to thank our collaborator, Dr. Francesco Stellacci, for his great work and insights into our systems; and his group member, Dr. Javier Reguera, with whom I had the pleasure of working closely with for the past two years. I also thank other Stellacci group members with whom I've collaborated, Miao Yu, Quy Ong, Stephen Schrettl, and Jin Young Kim.

I would also like to express my gratitude to my committee members, Prof. Ronald G. Larson, Prof. Nicholas A. Kotov and Prof. Anish Tuteja for their time, useful suggestions, and encouraging discussions.

I thank our group manager, Karen Coulter. Her hard work and dedication have made my journey so much easier, providing great resources and help along the way.

I thank Drs. Hao Jiang and Chetana Singh for many useful discussions about my simulations and the systems I studied. I thank all the other Glotzer group members for offering their great insight during group meetings and discussions, and specially Antonio, Pablo, Ryan, Ben, Eric I, Carolyn, Eric J, and Aaron K. for their friendship during these past five years. I would also to give special thanks to Kiersten, Gülin

and Ayako for all the lovely coffee hours and girls nights. You have made my time here in Michigan so much more special.

I would also like to thank the Graduate Society of Women Engineers and all its members for the past five years, especially my fellow officers. They helped me get through all the ups and downs of graduate school and provided a great space for personal growth and improvement outside of research.

I thank my parents and brothers for their love and support. And I thank specially my husband, Dr. Nick Stuckert. Not only was he been there for me every single step of the way offering encouragement and love; but he also listened to me think out-loud and practice my talks innumerable times, with infinite patience and always offering great advice and ideas to improve my work.

Table of Contents

List of Figures

List of Tables

Abstract

This thesis centers on the design of patchy particles and their self-assembly into ordered structures. Patchy particles have a patterned surface consisting of sticky and repulsive patches. These patches can be exploited to arrange the particles into ordered structures. In this thesis, the patchy particles are formed using monolayer protected metal nanoparticles (MPMNPs) consisting of a gold substrate coated by a self-assembled monolayer (SAMs) of thiol surfactants. The structure and patterning of the SAM can be controlled by tuning parameters like NP size and monolayer composition (variable number of surfactants in the monolayer with different length, immiscibility, and concentration). The patterned monolayer governs the interactions of the nanoparticle (NP) with its environment and other NPs. Binary SAMs were previously studied in the Glotzer group through molecular simulations. It was found that the MPMNPs could form Janus and striped particles based on sufficient entropic gains at the interfaces between immiscible surfactants.

Coarse-grained simulations performed in this study have added additional surfactants to the monolayer to find a variety of new patterns (decorated Janus, decorated Cerberus, Neapolitan, decorated stripes, alternating stripes and tetrahedral particles to name a few). These patterns can be further modified by changing the ordering of the surfactants, adding additional patchiness, or changing the coverage of the patches.

This work also introduces a new way of producing small Janus NP by using SAMs of surfactants with equal end groups but sufficient length difference. The long surfactants tend to crystallize on the surface of the NP leading to macrophase separation. These Janus NPs can be further functionalized to form dimers and other

interesting structures. The molecular dynamics results obtained in this study are in good agreement with experimental observations.

Finally, ordered structures obtained using patterned MPMNPs are also studied. Ordering of binary MPMNPs has been observed experimentally, and this study reproduces this behavior through computer simulations and extrapolates the findings to other mixed SAMs patterns.

Chapter 1. Introduction

1.1. Motivation

Self-assembly has emerged as a novel and reliable way to produce nano and microstructures in relative large quantities and with relatively low defects. The "atoms" and "molecules" of self-assembly are the building blocks that will arrange themselves into the final structures based on the interactions between them with or without the help of external fields.[1] Thus far, studies have mostly focused on what structures will form given a set of building blocks (forward self-assembly), to understand the interactions and learn about the self-assembly process. However, what we are really after are the design rules that will allow us to determine what building blocks would self-assemble into the desired structure (backward self-assembly).

The assembly potential of the building block depends directly on it's anisotropy. As shown in Figure 1, that anisotropy can be derived from the shape of the building block (branched, spherical, faceted, elongated, or flat) or from the patterning on its surface. The relative size and strength of this anisotropy with respect to the size of the building block (from micro to nanoparticle) will determine the strength of the interactions and the way the building blocks will self-assemble.

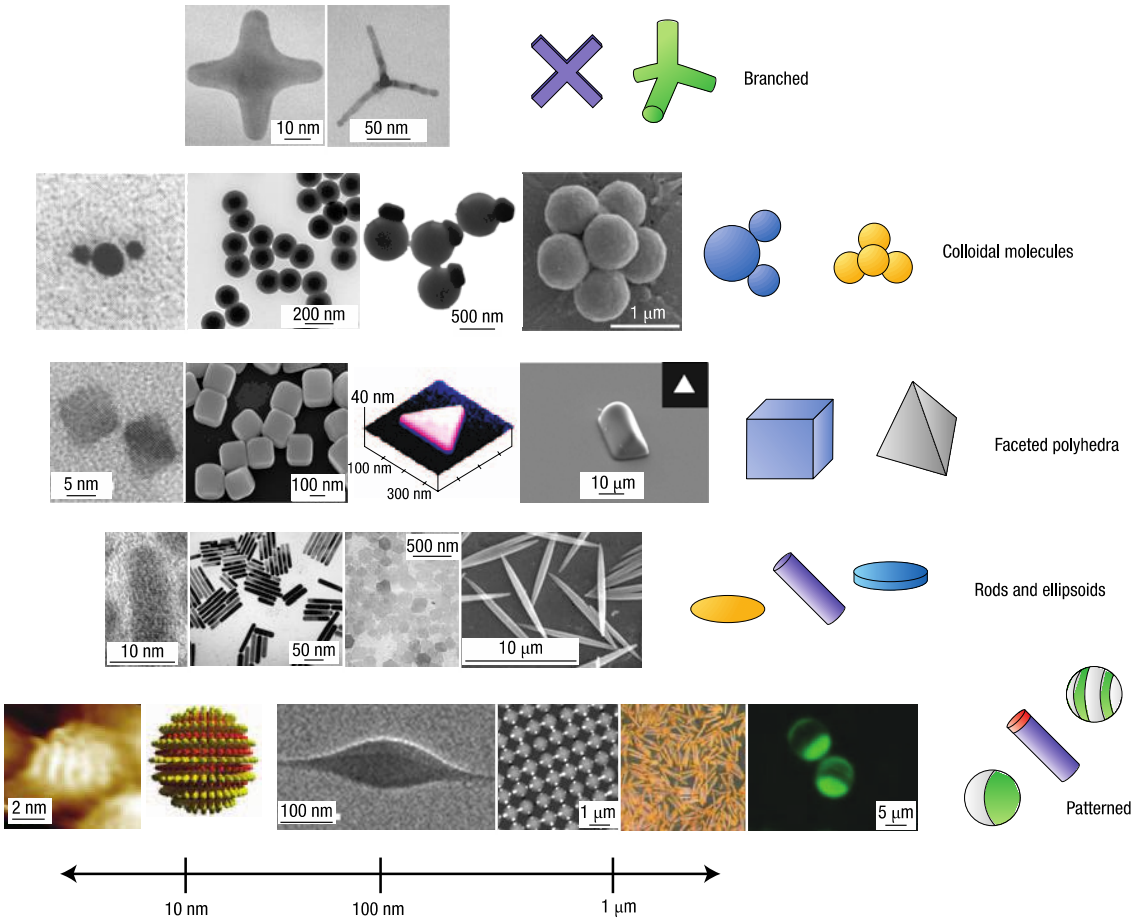

Figure 1 Recent examples of anisotropic building blocks of varying size (left to right) and anisotropy type (top to bottom).[1]

As shown in Figure 1, there are many way of experimentally producing different types of building blocks and exploiting their self-assembly into ordered structures. For example, the Pine group studies the directionally directed assembly of colloidal particles. This directionality can come from specific bonds, like the case of particles functionalized with sticky DNA strands (Figure 2a),[2] or be derived from the shape of the particles. One example of shape-guided assembly is the lock-and-key interactions between oil droplets with dimples (Figure 2b),[3] that can assemble by depletion into clusters when the size and depth of the dimple in the lock particles allows for the complimentary key particles to position themselves in the desired arrangement. Another example is the formation of crystals of cubic symmetry by cubic colloids shown in Figure 2c.[4]

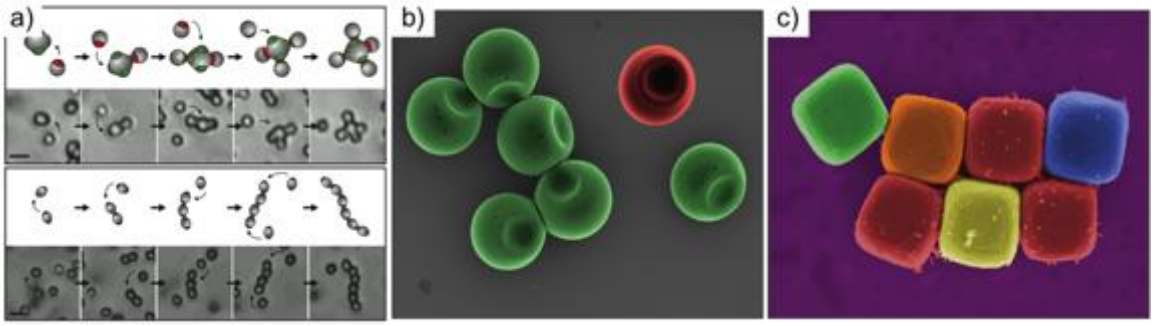

Figure 2 a) Schematic images (top panels) and snapshots from videos (bottom pales) showing step-by step reactions between colloidal atom,[2] b) Lock and key colloids,[3] and c) Cube crystallization[4]

Similar to the first example of colloids functionalized with DNA strands, the Mirkin group has been able to assemble different types of superlattices by functionalizing gold nanoparticles with hollow DNA spacers[5].

Within the many building blocks summarized in Figure 1, patchy particles seem to be one of the most promising. These particles have discrete interaction points (or patches) in their surface, that determine the interactions between them and with their environment, and ultimately their self assembled structure.[6] For example, the Granick group demonstrated how charged Janus microparticles with opposite electric charge on both hemispheres could assemble into clusters of different sizes and shapes depending on the number of particles interacting (Figure 3).[7] This Janus pattern is the simplest pattern possible on the surface of particles. The types of assembled structures could be expanded by changing the pattern on the particles, and by combining it with other dimensions of anisotropy, such as changing the shape of the particle as well. One way of expanding the types of patterns on the surface of the particles is by utilizing self-assembled monolayers of surfactants on top of the particles.

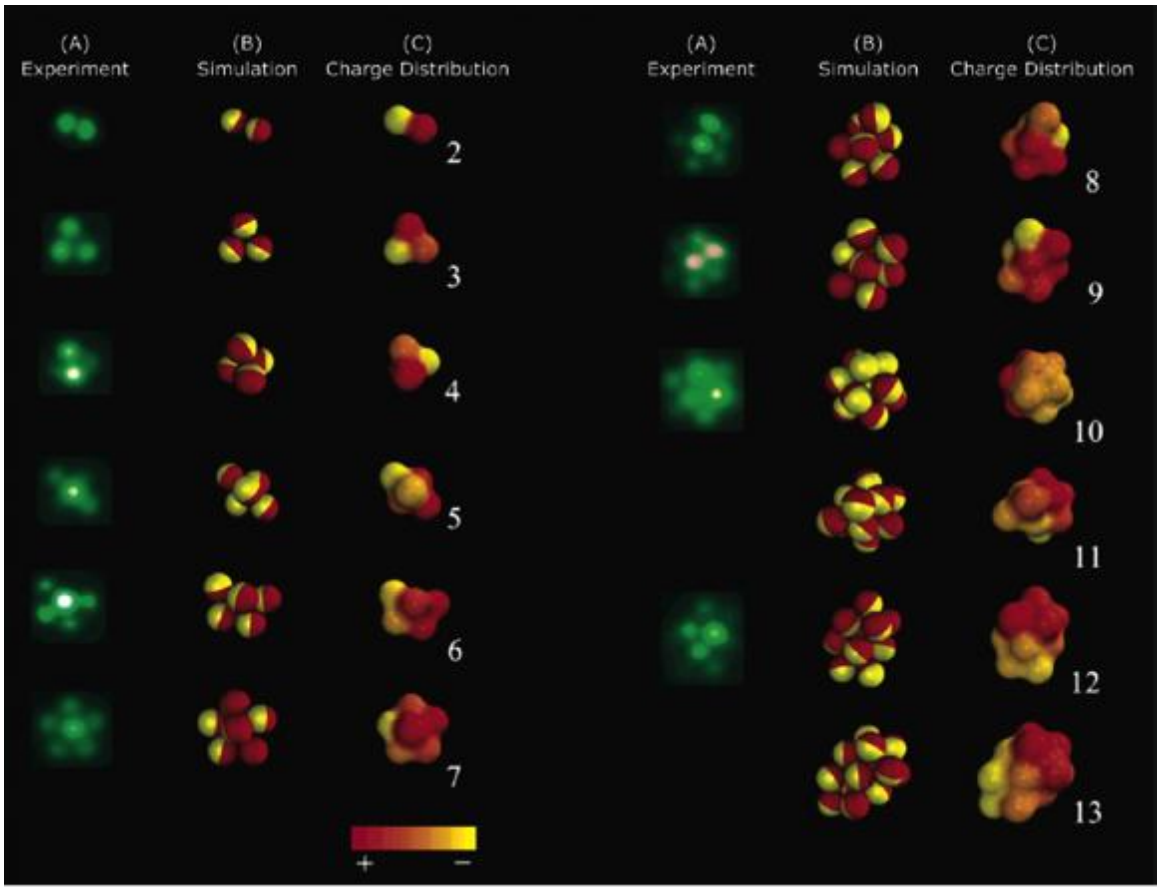

Figure 3 Comparison of clusters of Janus particles observed in experiments and Monte Carlo simulations.[7]

1.2. Self-assembly of surfactants

Monolayer protected metal nanoparticles (MPMNPs) are a type of patchy particle which consist of a gold substrate (with radius between 3 and 8 nm) stabilized by a self-assembled monolayer (SAM) of alkane thiols. It was shown that when the nanoparticle (NP) is coated with a binary mixture of immiscible surfactants (different end-groups to the alkane chain) of different length, it was possible to obtain either Janus particles or stripes (Figure 4) on the surface of the NP. It was possible to tune the width of the stripes by varying the composition of the binary SAM.[8] Computer simulations showed that the stripes form because of entropic gains

due to length and bulkiness mismatch between the surfactants.[9] They also predicted the formation of patterns on cylinders and flat surfaces.[10]

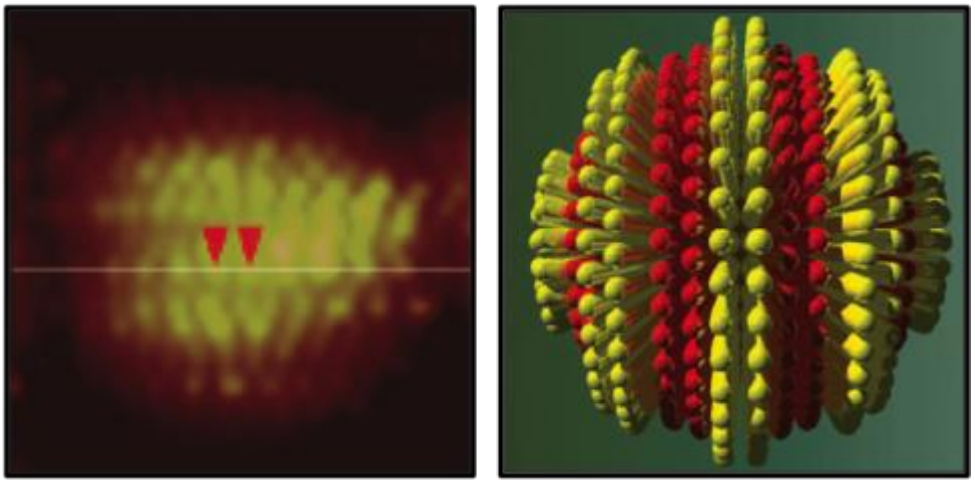

Figure 4 STM image (left) and schematic representation (right) of a striped MPMNP.[8]

To explore the many possibilities of self-assembled patterns offered by these patchy particles, it is possible to distinguish two levels of self-assembly. The first one is the assembly of the patterns on the surface of the NP (*i.e.*, the formation of stripes vs. Janus). The second one is the structures these NPs will self-assemble into. A first example was seen for the striped particles that form unidirectional chains of linked NPs.[11] Therefore, if one can understand and utilize the rules to design patterns on the SAM, one can also control the self-assembly process of the MPMNPs into a larger structure.

To exploit these two levels of assembly, it is first necessary to exploit the types of patterns that can be found on the monolayer. It is a natural step to increase the number of surfactants in the SAM. Experimental studies have demonstrated that it is possible to synthesize MPMNPs with up to five different thiol functional groups on their surface,[12] which opens up the possibility of forming more complex and diverse patterns.

Once the possible monolayer patterns have been identified, it will be possible to study the interactions between the different types of patterned NPs. This will allow us to identify the types of structures that can be formed with MPMNPs and to understand how the patterns of the SAMs define the self-assembled structure of the NPs.

1.3. Objectives

The objectives of this work are to:

1. Perform computer simulations of phase separation in grafted ternary and quaternary monolayers of surfactants.
2. Provide design rules to obtain desired patchy patterns on experiments.
3. Perform computer simulations of two-dimensional arrangements of multiple patchy nanoparticles.

1.4. Thesis organization

This thesis is organized as follows:

Chapter 1 describes the motivation and objectives of this work.

Chapter 2 provides the details of the methods and models used in this work. This includes dissipative particle dynamics (DPD), molecular dynamics (MD), polymer models and constrained dynamics. This chapter also covers the assumptions made to apply these methods, and a literature review of other systems for which these methods have been used.

Chapter 3 presents a comprehensive literature review of previous studies (both experimental and computational) of self-assembled monolayers of different

composition (homoligand and binary) on different substrates (flat surfaces and nanoparticles of different shapes).

Chapter 4 discusses in detail the different types of patchy patterns that can be obtained through mixed self-assembled monolayer of spherical nanoparticles. The patterns are classified in different families: tetrahedral, Brahma, Cerberus, Janus, and spotted. A discussion about the effects of symmetry breaking and a comparison between binary, ternary and quaternary patterns is also presented.

Chapter 5 introduces the results from performing dissipative particle dynamics simulations of ternary and quaternary monolayers on spherical surfaces. It presents a comprehensive study of the different parameters considered: nanoparticle radius, immiscibility between surfactants, length difference between surfactants, and stoichiometry of self-assembled monolayer. Phase diagrams for all these parameters are presented.

Chapter 6 presents results from performing molecular dynamics simulations of long surfactants with the same end group (miscible) on spherical nanoparticles. It is shown both through experiments and computer simulations that given a sufficient length difference, the surfactants will crystallize and macrophase separate in a Janus pattern. The effect of nanoparticle radius, length difference between surfactants, stoichiometry of self-assembled monolayer and degree of immiscibility between surfactants is studied for this system.

Chapter 7 describes the interactions of multiple patchy particles on an interface. The two-dimensional arrangement of patterned nanoparticles is studied through dissipative particle dynamics simulations.

Chapter 8 summarizes the contributions of this thesis to the field. It also introduces related projects being studied by other group members, and presents directions in which this field of research could be extended in the future.

Chapter 2. Simulation methods and models

This chapter provides the details of the methods used, taking particular care in explaining the choice of parameters for each system. Two methods have been employed in this thesis. The first one, dissipative particle dynamics (DPD), is a coarse-grained algorithm that overlooks the chemical details of the surfactants and allows for faster simulations based only on the geometry of the system and the length, flexibility, and immiscibility of the surfactants. The second method, molecular dynamics (MD), introduces chemical details about the structure of the alkane chains and the interactions between molecules. It allows to reproduce some specific behaviors that cannot be observed using DPD, but it requires longer computation times.

The models presented include the representation of a MPMNP by a gold shell and surfactant chains attached to it, and the simulation of a two-dimensional interface populated by multiple MPMNPs.

2.1. Dissipative particle dynamics

Dissipative particle dynamics (DPD)[13] is a coarse grained algorithm that simulates the behavior of fluids using interacting beads that move in a continuous space during discrete time steps in the NVT ensemble. Mass and momentum are conserved throughout the system, which is in thermal equilibrium and satisfies the fluctuation-dissipation theorem.[14] The microscopic details of the interactions are

disregarded, making the simulation more computationally efficient while still providing a good approximation for the behavior of the fluid on mesoscopic length scales.[15] The repulsive nature of the force between beads favors the modeling of phase separation of immiscible surfactants in which the net effective interaction between unlike surfactants is repulsive. DPD has been used successfully to model block copolymers,[16] amphiphilic mesophases,[17] surfactant,[18] and polymer phase separations,[19] as well as the assembly of patchy patterns on binary MPMNPs.[9]

In DPD, the interaction between beads is derived from a soft repulsive force. The beads act like fluid elements that diffuse through each other instead of colliding when they come close together. This allows them to move farther in a given time step than they would in equivalent molecular dynamics (MD) simulations. Compared to MD, DPD allows for larger time steps to be employed, and particles can have displacements of about one mean free path per time step.[20] The stochastic forces acting on each of the beads are approximated by a sum of the interactions of that bead with its closest neighbors. The effect of the implicit fluid is modeled by a friction factor and a random force.

2.1.1. Bonded interactions

The bonded interactions between beads of the same surfactant are simulated through a simple harmonic spring as shown in Equation 1. If bead *i* and *j* are bonded to each other, then they each feel a force of the same magnitude and opposite direction that is directly proportional to the distance between them (Equation 2).

$$\vec{f}_{ij} = C\,\vec{r}_{ij} \qquad \textbf{Equation 1}$$

Where:

$$\vec{r}_{ij} = \vec{r}_i - \vec{r}_j$$ **Equation 2**

The scaling constant *C* determines the flexibility of the ligand. Larger *C* will cause the surfactants to be more rigid, while a smaller *C* will allow the surfactants to be more elongated and flexible.

2.1.2. Non-bonded interactions

The forces acting on the DPD beads can be calculated as a function of three pairwise additive terms as shown in Equation 3: a conservative force $\left(\vec{f}^{\,C}\left(\vec{r}_{ij}\right)\right)$, a drag force $\left(\vec{f}^{\,D}\left(\vec{r}_{ij},\vec{v}_{ij}\right)\right)$, and a random force $\left(\vec{f}^{\,R}\left(\vec{r}_{ij}\right)\right)$.

$$\vec{F}_i = \sum_{j \neq i}\left[\vec{f}^{\,C}\left(\vec{r}_{ij}\right) + \vec{f}^{\,D}\left(\vec{r}_{ij},\vec{v}_{ij}\right) + \vec{f}^{\,R}\left(\vec{r}_{ij}\right)\right]$$ **Equation 3**

2.1.2.1. Conservative force

The conservative force felt by the DPD beads is a soft repulsive force defined by Equation 4.

$$\vec{f}^{\,C}\left(\vec{r}_{ij}\right) = \begin{cases} a_{ij}\left(1 - r_{ij}\right)\hat{r}_{ij} & r_{ij} < r_{cut} \\ 0 & r_{ij} \geq r_{cut} \end{cases}$$ **Equation 4**

This force is proportional to the distance between two interacting beads, r_{ij}. The cutoff radius is set to unity ($r_C = 1$). This means that the force is always positive, which makes it a repulsive force without any attractive wells. The parameter a_{ij} determines the strength of the repulsion, which is always finite as shown in Figure 5. Since the repulsion between beads is finite, they can overlap at any point during the simulation. This possibility of overlapping beads is what makes this a soft force.

Physically, this can be explained because the DPD beads represent fluid elements and not specific atoms or molecules, so therefore they are allowed to flow through each other. This overlapping of beads is what allows DPD to take larger time steps than other simulation methods.

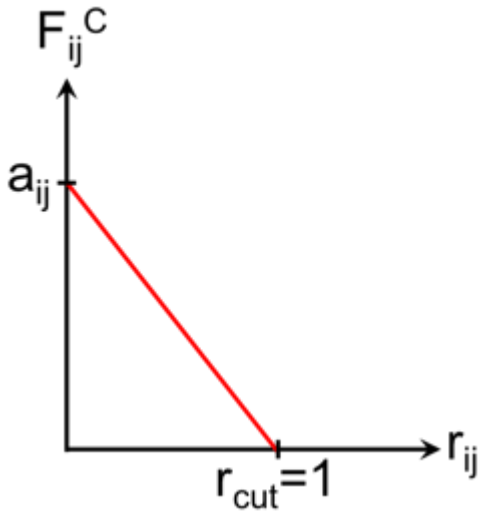

Figure 5 Soft repulsion potential as a function of the distance between two beads i and j.

The beads' diameter is also set to *1* (like the cutoff radius), which means that a bead will only interact with overlapping beads. Therefore the density of the system has to be higher than *1* to guarantee that the beads can feel each other and move in the system.

Since all interactions between beads are repulsive, different surfactants will need to have different relative repulsions, *i.e.* different a_{ij} parameters. To simulate immiscibility between surfactants A and B, we choose $a_{AA} = a_{BB} < a_{AB}$. The base repulsion between beads of the same surfactant is set to $a_{ii} = 25$.[16] The repulsion between unlike surfactants can be increased to model increasing degree of immiscibility between surfactants.

2.1.2.2. Dissipative force

In DPD simulations, the solvent is kept implicit to reduce computation time and avoid having to keep track of all the solvent particles in the system. The dissipative force represents the drag that the DPD beads would feel from the solvent, and is defined in Equation 5.

$$\vec{f}^{\,D}\left(\vec{r}_{ij},\vec{v}_{ij}\right) = -\gamma\,\omega^{D}\left(r_{ij}\right)\left(\vec{v}_{ij}\cdot\vec{r}_{ij}\right)\hat{r}_{ij} \qquad \textbf{Equation 5}$$

Where:

$$\vec{v}_{ij} = \vec{v}_{i} - \vec{v}_{j} \qquad \textbf{Equation 6}$$

The parameter γ controls the strength of the frictional force between the beads, and $w^D(r_{ij})$ is a weight function that will be defined in section 2.2.3.

2.1.2.3. Random force

The random force is also used to represent the effect of the implicit solvent. This force simulates the effects of random fluid particles colliding with the DPD beads.

$$\vec{f}^{\,R}\left(\vec{r}_{ij}\right) = \sigma\,\omega^{R}\left(r_{ij}\right)\varepsilon_{ij}\,\hat{r}_{ij} \qquad \textbf{Equation 7}$$

In Equation 7, σ is the noise level of the system. $w^R(r_{ij})$ is a weight function that will be defined in the next section. ε_{ij} is a random number with uniform distribution and unit variance, with $\varepsilon_{ij} = \varepsilon_{ji}$.

2.1.3. Thermostat

The dissipative and random forces defined in 2.1.2.2 and 2.1.2.3 respectively, are coupled through their weight functions as shown in Equation 8.

$$\omega^{D}(r_{ij}) = [\omega^{R}(r_{ij})]^{2} = \begin{cases} (1 - r_{ij})^{2} & r_{ij} < r_{cut} \\ 0 & r_{ij} \geq r_{cut} \end{cases} \qquad \textbf{Equation 8}$$

They are also couple through the parameters γ and σ, and strongly dependent on the temperature of the system, as shown in Equation 9.

$$\sigma^{2} = 2k_{B}T\gamma \qquad \textbf{Equation 9}$$

This strong coupling and dependence in the temperature of the system makes these two forces act like a thermostat and can be tuned to keep the temperature fluctuations of the system at a minimum. In the DPD system, $k_BT = 1$, $\sigma = 3$, and $\gamma = 1/2$.[16] Because all the forces between beads is applied in an equal and opposite manner, DPD conserves linear as well as angular momentum and can be used to simulate hydrodynamic phenomena.[21]

2.1.4. Integration method

Each time step, the forces acting on every bead in the system are calculated as a sum of interactions between each bead and its neighbors within a cutoff radius of one bead diameter (Equation 3). The force acting on a bead is used to calculate its new position and velocity for the next time step by numerically integrating Newton's equations of motion using a modified velocity-Verlet algorithm. This algorithm is defined by the following equations:

$$\vec{r}_i(t+\Delta t) = \vec{r}_i(t) + \Delta t\vec{v}_i(t) + \frac{1}{2}\Delta t^2 \vec{f}_i(t) \qquad \textbf{Equation 10}$$

$$\tilde{\vec{v}}_i(t+\lambda\Delta t) = \vec{v}_i(t) + \lambda\Delta t\,\vec{f}_i(t) \qquad \textbf{Equation 11}$$

$$\vec{f}_i(t+\Delta t) = \vec{f}_i(\vec{r}_i(t+\Delta t), \tilde{\vec{v}}_i(t+\lambda\Delta t)) \qquad \textbf{Equation 12}$$

$$\vec{v}_i(t+\Delta t) = \vec{v}_i(t) + \frac{1}{2}\Delta t\left(\vec{f}_i(t) + \vec{f}_i(t+\Delta t)\right) \qquad \textbf{Equation 13}$$

In Equation 10, the position of the beads in the system is updated as a function of the positions, velocities and forces from the previous step. In Equation 11, an intermediate velocity is guessed as a weighted average between the velocity from the previous step and the forces from the previous time steps integrated in time. This step is necessary because the dissipative force depends on the velocity of the particles (Equation 5). With the guessed velocity and the updated positions, the new forces of the system can be calculated with Equation 12. Once the forces have been calculated, the new velocity of the system can be calculated as defined in Equation 13. After each time step, the physical properties (temperature, kinetic and potential energy) of the system are calculated. This iterative procedure is continued until equilibrium has been reached.

2.1.5. Validation and assumption

Studies were conducted to determine the optimal surface density of beads that would allow the surfactants to microphase separate without unnecessarily increasing the number of particles that had to be simulated. Surface density was set to *6 beads/σ^2* for spheres and cylinders, and to *3 beads/σ^2* for flat surfaces. Spheres and cylinders need a higher surface density because the radius of curvature

increases the available space so that not enough beads are interacting with each other. Doubling the surface density with respect to flat surfaces allows for a sufficient number of interactions between beads for the system to evolve.

Independence from time step was also determined by running simulations at a time step 10 times smaller than the one being used and verifying validity of results.

Since DPD is a coarse-grained algorithm, selected patterns were verified by comparing them to the patterns obtained by running more detailed molecular dynamics simulations.

2.2. Molecular dynamics

Similar to DPD, MD is an algorithm for molecular simulations in which the particles of the system are moved in discrete time steps in a continuum space. However, the MD particles are not soft, meaning that, unlike DPD beads, they are not allowed to overlap with each other. The system is less coarse-grained than DPD, in that the MD particles represent actual atoms or molecules, rather than abstract fluid elements.

The united-atom OPLS (Optimized Potentials for Liquid Simulations) force field[22,23] was used to simulate the interactions between particles in the system. The united-atom configuration simplifies the system to reduce the computation time by grouping atoms into CH_2 and CH_3 groups. This reduces the number of particles in the system, while still providing a good approximation of the behavior of the surfactants. This force field has been successfully used previously to simulate homo and mixed-ligand mixtures of surfactants on spherical NPs.[9,24] The details of this force field are described in the following sections for non-bonded (2.2.1) and bonded interactions (2.2.2).

The MD simulations presented in this thesis were conducted in the NVT ensemble, and the temperature of the system was regulated using a Nosé-Hoover thermostat (section 2.2.3). The integration method used was similar to Velocity-Verlet

algorithm used for DPD (section 2.1.4). The surface density was 21.6 Å^2 per surfactant chain.[24]

2.2.1. Non-bonded interactions

Different types of potentials are used to represent the interactions between different atoms and molecules pairs. Figure 6 shows the different shapes and scaling of the potentials as defined by the united-atom OPLS force field for our system. Intramolecular non-bonded interactions are only counted for atoms three or more bonds apart.

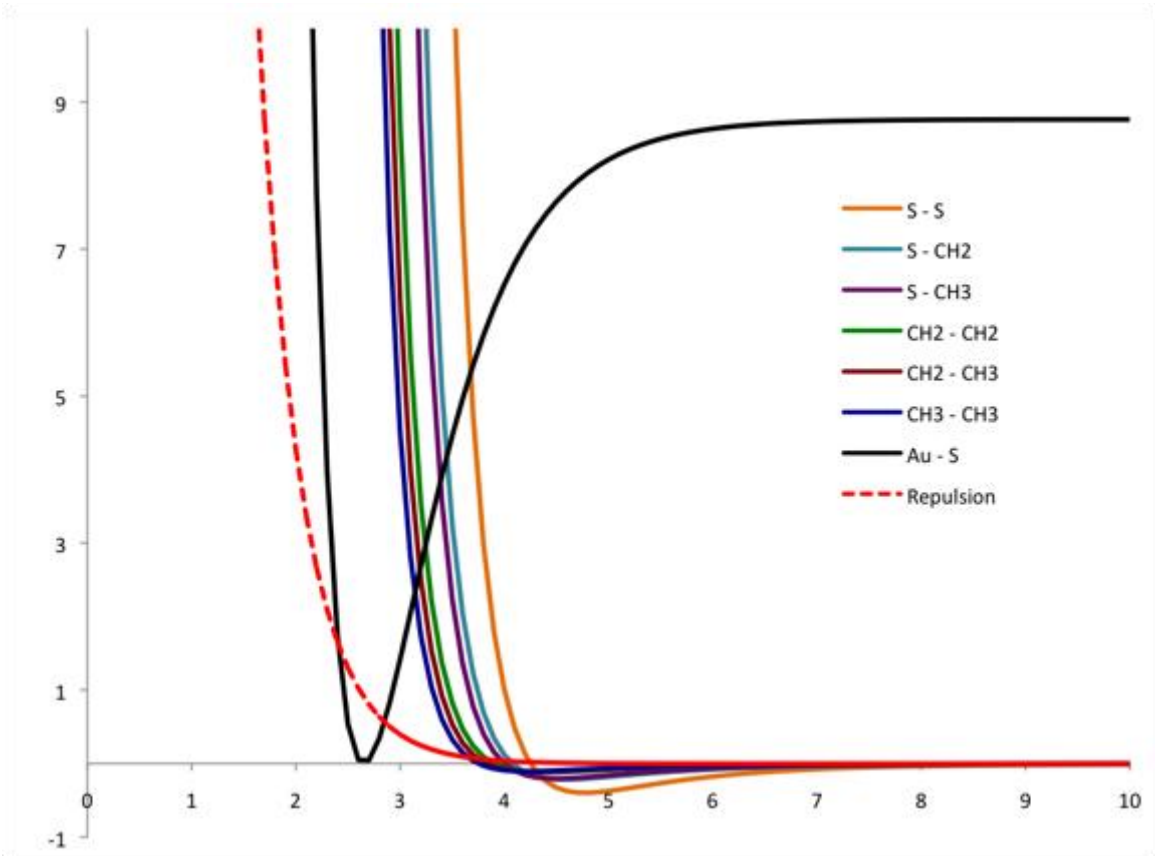

Figure 6 Non-bonded interactions for a binary SAM according to the united-atom OPLS force field.

2.2.1.1. Lennard-Jones potential

The Lennard-Jones potential is defined in Equation 14. This potential is employed to represent the interactions between the sulfur heads and the alkane tails of the surfactants. It has a short range repulsion and long range attraction centered around σ, the equilibrium distance at which the two particles would rather sit from each other. The short-range repulsion describes the Pauli repulsion of overlapping electron orbitals, and the long-range attraction is due to van der Waals forces.

$$V\left(r_{ij}\right) = 4\varepsilon\left[\left(\frac{\sigma}{r_{ij}}\right)^{12} - \left(\frac{\sigma}{r_{ij}}\right)^{6}\right] \qquad \textbf{Equation 14}$$

The Lennard-Jones parameters used in this thesis are summarized in Table 1.[24, 25]

Table 1 Lennard-Jones potential parameters

Atom	σ (Å)	ε (kcal/mol)
S	4.250	0.39743
CH (sp2)	3.800	0.11500
CH_2 (sp2)	3.850	0.14000
CH_2 (sp3)	3.905	0.11800
CH_3 (sp3)	3.905	0.17500
Au	2.935	0.03900

The combination rules for these parameters are presented in Equation 15 for the equilibrium distance, σ, and in Equation 16 for the depth of the potential well, ε.

$$\sigma_{ij} = \sqrt{\sigma_{ii} \cdot \sigma_{jj}} \qquad \textbf{Equation 15}$$

$$\varepsilon_{ij} = \sqrt{\varepsilon_{ii} \cdot \varepsilon_{jj}} \qquad \textbf{Equation 16}$$

2.2.1.2. Morse potential

The Morse potential is used to model the interactions between the gold atoms of the NP and the sulfur heads of the ligands. It is described by Equation 17.

$$V\left(r_{ij}\right) = E_0\left[\left\{1 - \exp\left(-k\left(r_{ij} - r_0\right)\right)\right\}^2\right] \qquad \textbf{Equation 17}$$

The parameters that describe the gold-thiol interaction are presented in Table 2. [24]

Table 2 Morse potential parameters

Atoms	E_0 (kcal/mol)	r_0 (Å)	α (Å^{-1})
Au – S	8.763	2.65	1.47

As can be seen in the black curve in Figure 6, the Morse potential has a very sharp well that defines the distance at which the two atoms should sit from each other. This sharp well is the best way of describing the precise distance in which the thiol heads should be from the gold NP, preventing them from getting either too close or too far away.

2.2.1.3. Modified Buckingham potential

The Buckingham potential without the attractive terms is defined in Equation 18.

$$V\left(r_{ij}\right) = A\exp\left(\frac{-r}{\sigma_S}\right) \qquad \textbf{Equation 18}$$

This modified form of the Buckingham potential is used to model the additional repulsion between unlike surfactants and between the surfactants tails and the gold NP to prevent the tails from penetrating the shell. This sharp short-range repulsion is shown by the dashed red line in Figure 6. The parameters used for the modified

Buckingham potential are summarized in Table 3, and are all the same for all interacting pairs of particles.

Table 3 Modified Buckingham potential parameters

A (kcal/mol)	σ_S (Å)
500	0.4

2.2.2. Bonded interactions

Bonded interactions are also more complex than the ones used for DPD to correctly model the zigzagging carbon backbone in alkane chains. Interactions between two, three, and four consecutives atoms are therefore required.

2.2.2.1. Bond potential

The bonds between two consecutive atoms are modeled via a harmonic bond as described in Equation 19.

$$V\left(r_{ij}\right) = \frac{1}{2} k \left(r_{ij} - r_0\right)^2 \qquad \textbf{Equation 19}$$

The parameters for this bonded interaction are presented in Table 4. [24, 26]

Table 4 Bond potential parameters

Bond	r_0 (Å)	k (kcal/mol)
S – CH_2 –	1.81	222
– CH_2 – CH_2 –	1.54	260
– CH_2 – CH_3	1.50	260
– CH = CH_2	1.34	260

2.2.2.2. Angle potential

The angle between three consecutive united-atoms (Figure 7) is modeled using the harmonic angle potential shown in Equation 20.

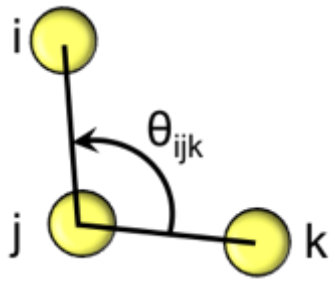

Figure 7 Schematic of angle interactions

$$V\left(\theta_{ijk}\right) = \frac{1}{2} k \left(\theta_{ijk} - \theta_0\right)^2 \qquad \textbf{Equation 20}$$

The parameters for this interaction are summarized in Table 5. [24, 26]

Table 5 Angle potential parameters

Angel	θ_0 (Å)	k (kcal/mol)
S – CH_2 – CH_2 –	114.40	62.5
– CH_2 – CH_2 – CH_2 –	109.47	63.0
– CH_2 – CH_2 – CH_3	109.47	63.0
– CH_2 – CH = CH_2	124.00	63.0

2.2.2.3. Dihedral angle potentials

The torsion interactions between four consecutive particles (Figure 8) are modeled using triple cosines as shown in Equation 21 as a function of the angle between two planes, Φ_{ijkn}.

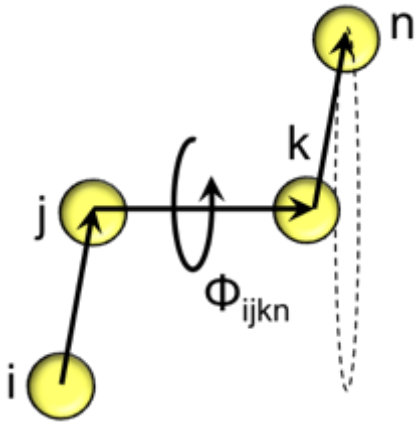

Figure 8 Schematic of dihedral interactions between four consecutive united-atoms

$$V\left(\phi_{ijkn}\right) = \frac{1}{2}A_1\left(1 + \cos\left(\phi_{ijkn}\right)\right) + \frac{1}{2}A_2\left(1 - \cos\left(2\phi_{ijkn}\right)\right) + \frac{1}{2}A_3\left(1 + \cos\left(3\phi_{ijkn}\right)\right) \qquad \textbf{Equation 21}$$

The parameters used to model the triple cosine dihedral potential are shown in Table 6.

Table 6 Torsion potential parameters

Dihedral	A_1 (kcal/mol)	A_1 (kcal/mol)	A_2 (kcal/mol)	A_3 (kcal/mol)
S – CH_2 – CH_2 – CH_2 –	0.0000	1.4119	–0.27187	3.147029
– CH_2 – CH_2 – CH_2 – CH_2 –	0.0000	1.4119	–0.27187	3.147029
– CH_2 – CH_2 – CH_2 – CH_3	0.0000	1.4119	–0.27187	3.147029
– CH_2 – CH_2 – CH = CH_2	0.2072	0.3728	–0.47390	1.21850

2.2.3. Thermostat

To keep the temperature of the system constant, the Nosé-Hoover thermostat was used. This thermostat acts by introducing a heat bath associated with an artificial mass to the system. The Nosé-Hoover thermostat modifies Newton's equations of motion as shown in Equation 22 and Equation 23:

$$\frac{d\vec{r}(t)}{dt} = \vec{v}(t) \qquad \textbf{Equation 22}$$

$$\frac{d\vec{v}(t)}{dt} = \frac{\vec{f}(t)}{m} - \chi(t)\vec{v}(t) \qquad \textbf{Equation 23}$$

The friction coefficient, χ, is defined by Equation 24 as follows:

$$\frac{d\chi(t)}{dt} = \frac{N_f k_B}{Q}(\tau(t) - T_{ext}) \qquad \textbf{Equation 24}$$

Q, the effective mass of the thermostat, is defined by Equation 25:

$$Q = N_f k_B T_{ext} \tau_T^2 \qquad \textbf{Equation 25}$$

τ_T is a time constant and N_f is the number of degrees of freedom in the system. $\tau(t)$ is the instantaneous temperature of the system at time t.

2.3. Simulation model

This section described the models used to represent the surfactants, the nanoparticles, and the two dimensional interfaces in which the nanoparticles can self-assemble.

2.3.1. Surfactants

The surfactants are represented as chains of beads connected by simple harmonic springs as shown in Figure 9.[27]

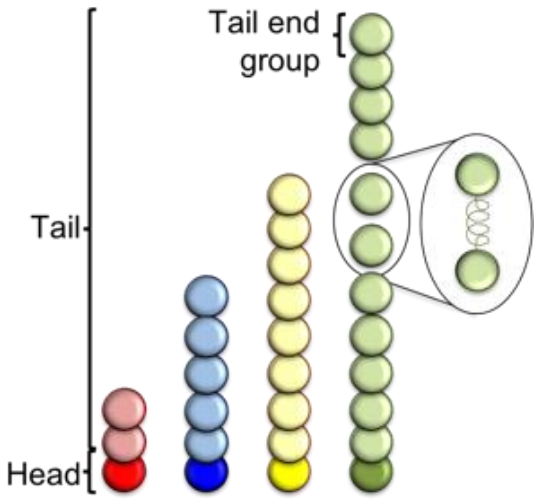

Figure 9 Bead and chain model to represent thiol alkane surfactants.

The head of the surfactants represents the thiol group that adsorbs into the gold surface. The tail is the alkane chain, and the tail end group is the functional group at the end of the thiol alkane (for example, a methyl group, an alcohol, or a carboxylic acid). The immiscibility between different surfactants comes from the interactions between different tail end groups. For most of the results presented in this thesis, only the head group is shown in the figures to simplify identifying the patterns formed by the surfactants (Figure 10). Only in Chapter 6 will the tails be shown, because their conformation is relevant to the formation of the patterns.

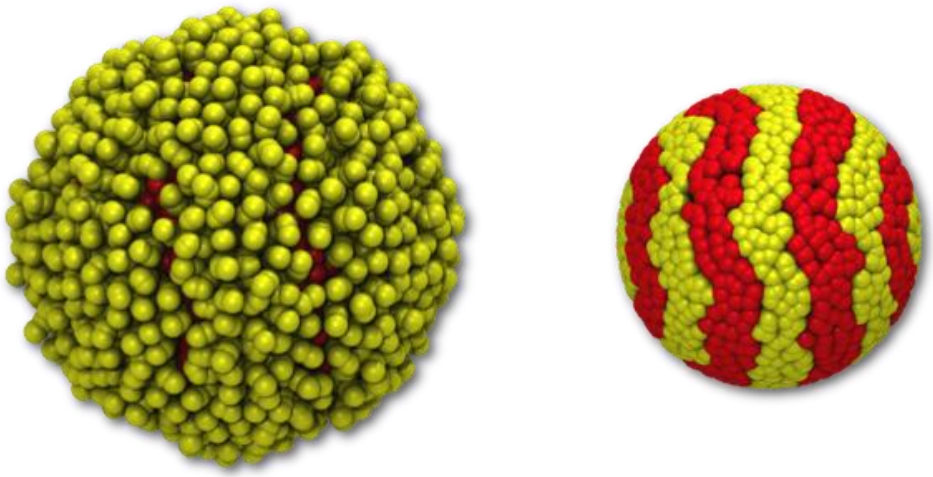

Figure 10 Striped NP with (left) and without (right) surfactant tails.

2.3.2. Nanoparticles

To model a MPMNP, beads are distributed over the surface of the spherical NP (Figure 11) with an initial configuration, which will be discussed in section 2.3.2.1. The gold NP is represented by a hollow shell described in section 2.3.2.2. The thiol heads are directly adjacent to the surface of the NP and restricted to the surface using constrained dynamics (section 2.3.2.3).

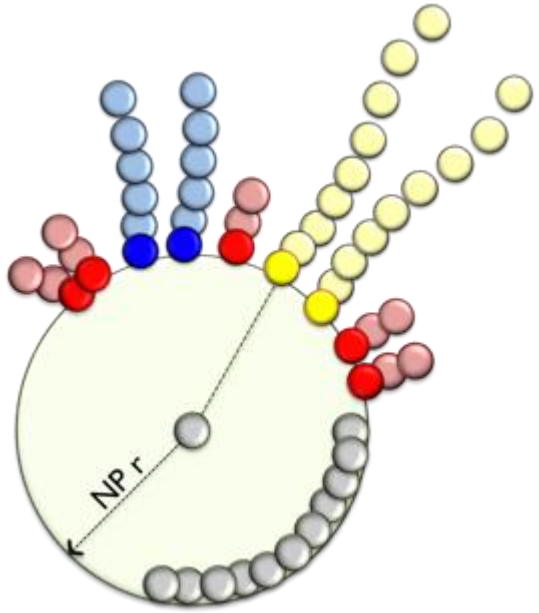

Figure 11 Schematic representation of a spherical nanoparticle with a monolayer of surfactants.

2.3.2.1. Initial configurations

To assert that the patterns correspond to the equilibrated state of the system, independence of thermodynamic path was confirmed by initializing all simulations from different initial configurations (Figure 12 for DPD and Figure 13 for MD simulations).

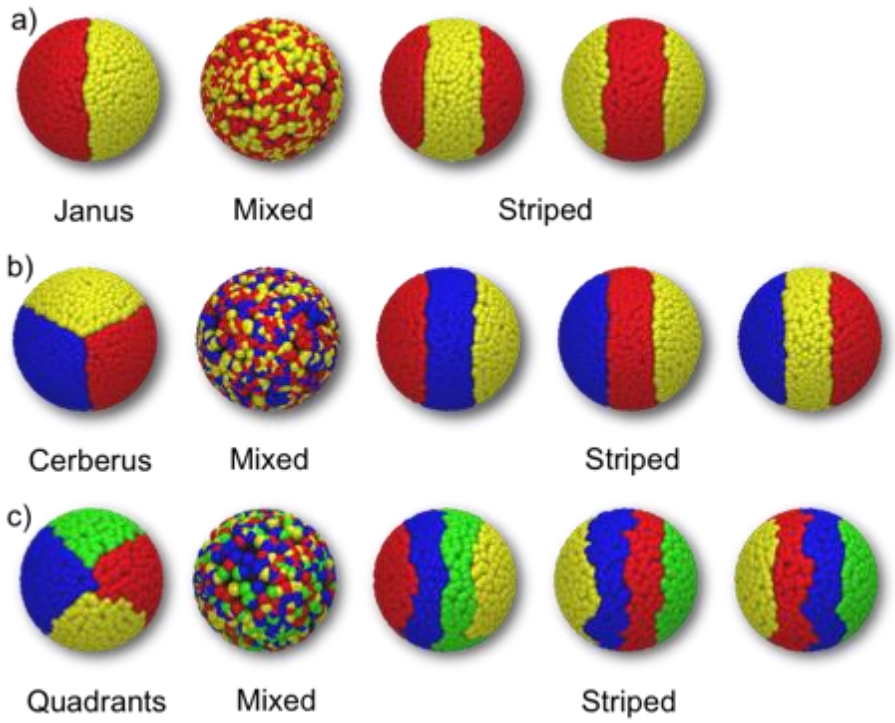

Figure 12 Initial configurations for a) binary, b) ternary and c) quaternary MPMNPs. Tails not shown. Red: short, blue: medium, green: long, yellow: longest surfactant.

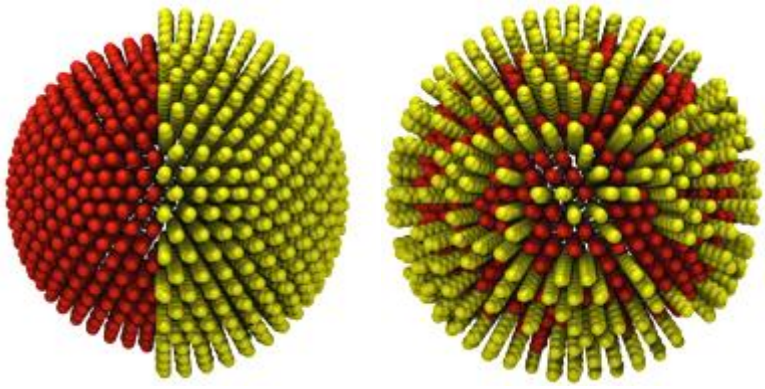

Figure 13 Initial configurations for MD simulations. Left: Janus configuration, and right: randomly mixed. Short surfactant: red, and long: yellow. Tails shown.

For each set of parameters studied in this thesis, the simulation was initialized from all the different initial configurations considered (as shown in Figure 14 for a particular ternary case). After running for a sufficiently long number of time steps,

the results from all the independent simulations were compared to verify that the resulting pattern was the same (within statistical differences), and therefore independent of initial configuration. This indicates that the final pattern obtained is the equilibrium pattern for the given set of parameters. For the purpose of this thesis, only one equilibrated pattern is shown and it is implicit that several independent simulations were run to verify said pattern.

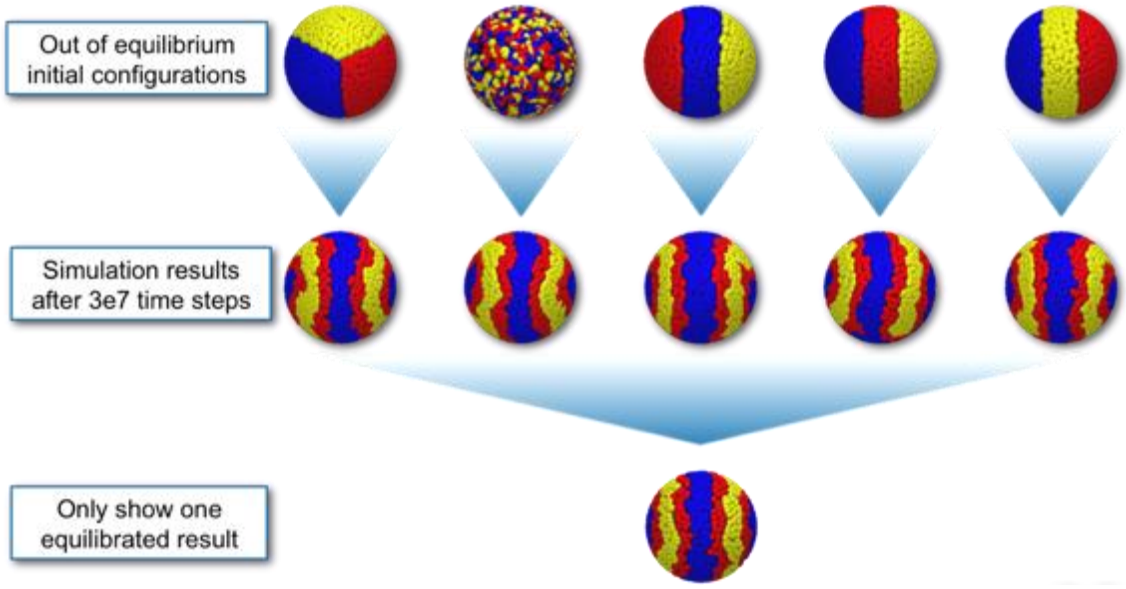

Figure 14 Example of simulation from five different initial configurations to verify equilibrium pattern. Tails not shown.

2.3.2.2. Gold shell

The gold shell is necessary to prevent the surfactant tails from penetrating the NP. An artificial repulsion between the surfactant beads and the gold atoms is added for that purpose. For MD simulations, the interactions between the thiol heads and the gold atoms are also important to capture the correct tilt angle of the surfactants. Figure 15 shows a gold NP from which a fraction has been removed to show the empty interior.

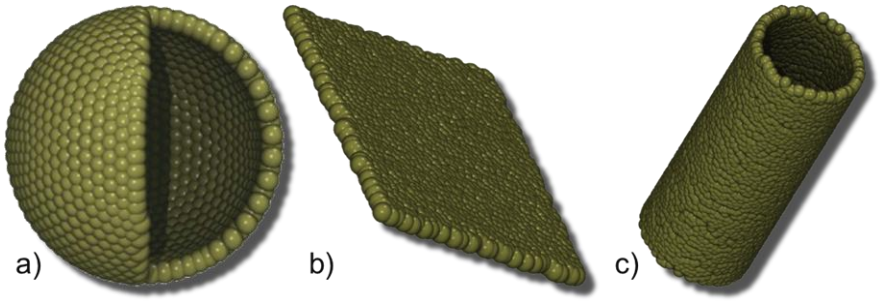

Figure 15 View of gold shells for a) spheres, b) flat surfaces and c) cylinders. The sphere (a) has been sliced to show the empty interior.

For DPD simulations, the configuration of the gold NP does not affect the patterns formed by the monolayer, as long as the surface density is enough to prevent the ligand tails from penetrating it. For MD simulations however, it was important to use the right parameters. The gold atoms were distributed with a surface density of 10.4 Å^2/Au.[24] The NP shell was relaxed first at 0K using a Lennard-Jones potential to model the interaction between the gold atoms (Table 1). The sphericity of the NP was kept using constrained dynamics. For simulations including the surfactants, the gold atoms were frozen in their equilibrium positions to reduce computation costs.

2.3.2.3. Constrained dynamics

This algorithm works by allowing the beads to move each time step like they were not constrained to a spherical surface. After the particles have been moved, a correction is applied to modify their un-constrained position to the desired *R* distance from the center of the NP. The algorithm is defined by Equation 26 and Equation 27[27]:

$$\vec{F}_{constrained}(t) = \vec{F}(t) - \frac{\lambda \vec{r}(t)}{(\Delta t)^2} \qquad \textbf{Equation 26}$$

$$\vec{r}(t + \Delta t) = \vec{r}_u(t + \Delta t) - \frac{\lambda}{m}\vec{r}(t) \qquad \textbf{Equation 27}$$

With λ defined in Equation 28 as follows:

$$\lambda = \frac{\vec{r}(t)\cdot\vec{r}_u(t+\Delta t) - \sqrt{\left[\vec{r}(t)\cdot\vec{r}_u(t+\Delta t)\right]^2 - R^2\left[r_u^2(t+\Delta t) - R^2\right]}}{\frac{R^2}{m}} \qquad \textbf{Equation 28}$$

The previous equations can be used to constrain beads to both spheres and cylinders. In the case of cylinders, however, the equations are only applied in two dimensions, while periodic boundary conditions are applied on the third dimension. This means the cylinders essentially behave like they are infinitely long.

For flat surfaces, the beads are constrained to a plane defined by $z = R$, Equation 26 and Equation 27 still apply, but λ is now defined by Equation 29:

$$\lambda = \frac{z_u(t+\Delta t) - R}{\frac{z(t)}{m}} \qquad \textbf{Equation 29}$$

Constraint dynamics are implemented through the SHAKE algorithm[29] when used in conjunction with the Velocity-Verlet integration method.

2.3.3. Two-dimensional interfaces

Two-dimensional interfaces were used to simulate the assembly of multiple NPs (Chapter 7). The pattern on the NPs was frozen and the ligands were not allowed to move on the surface of the NP, to reduce computing times. Therefore, all the beads in a MPMNP were treated as a rigid body (2.3.3.1) for each of the NPs. Periodic boundary conditions were allowed in two-dimensions, but wall constrains (2.3.3.2) were utilized in the third dimension to guarantee that the NPs stayed on the interface and arranged in a single layer.

2.3.3.1. Rigid bodies

The rigid body constrains allow to main rigid bonds between beads, so that they do not change position with respect to each other. For the simulations of multiple NPs, the positions of the beads within one particle are kept fixed to allow the pattern to remain unaltered throughout the simulation. Each rigid body is described by a center of mass moving with a certain velocity. The angular momentum and a normalized quaternion represent the orientation of the body. The net force and torque acting on the body are the sums of the individual forces and torques resulting from the particle-particle interactions.[33]

2.3.3.2. Wall constrains

Periodic boundary conditions are used in all directions and wall constrains are necessary to keep the NPs confined to a two-dimensional interface as shown in Figure 16. The NPs are arranged in the *xy* plane, and two walls are added directly above and below them (shown in black shades in Figure 16). The box size on the *z*-direction is larger than the cutoff radius so that the NPs are not interacting through that dimension, guarantying that the NPs truly behave as a single monolayer.

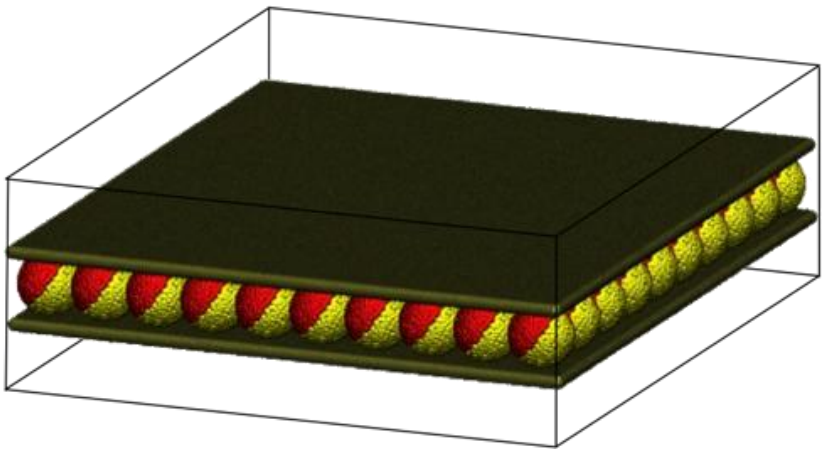

Figure 16 Simulation box used for two-dimensional interfaces. Janus NPs shown in the middle. The black lines represent the simulation box. The brown surfaces represent the walls constraining the NPs.

For MD simulations, the wall constrains are modeled through a Lennard-Jones potential without the attractive well, as shown in Equation 30. A coefficient of $\varepsilon = 1$ is enough to keep the NPs constrained to the desired plane.

$$V(r) = \begin{cases} 4\varepsilon\left(\frac{\sigma}{r}\right)^{12} & r < r_{cut} \\ 0 & r \geq r_{cut} \end{cases} \qquad \textbf{Equation 30}$$

For DPD simulations, the walls are made of DPD beads distributed at a density of *1* bead per σ^2 with and interbead repulsion between all beads in the system and the wall beads of $a_{iw} = 300$.

2.4. Computational tools

In this section we describe the modeling packages used to perform the simulations presented in this thesis.

2.4.1. HOOMD-blue

HOOMD-blue[30, 31] is a Highly Optimized Object-oriented Molecular Dynamics open source code developed and maintained by the Glotzer group. The code utilizes the massively parallel architecture of GPUs to speed-up molecular simulations. This package was used for all DPD simulations,[32] including both the assembly of ternary and quaternary monolayers, and also the assembly of patchy NPs in an interface by utilizing the rigid body functionality.[33] HOOMD-blue was also used to perform MD simulations of the binary system.

Figure 17[32] shows the speed-up gained by using HOOMD-blue for DPD simulations on a single GPU compared to the LAMMPS[34] parallel code on multiple CPU cores.

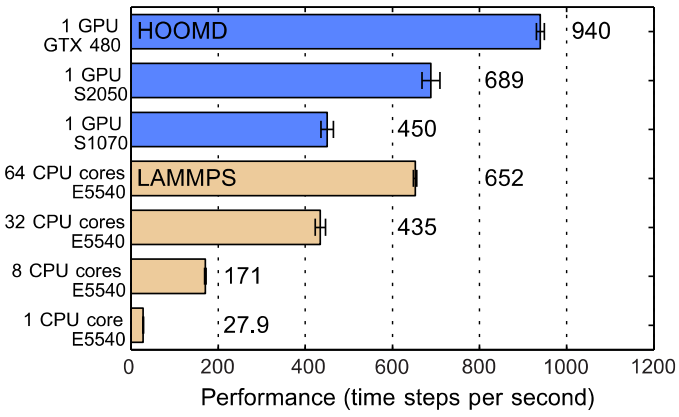

Figure 17 Benchmarks comparing the speed-up achieved for DPD by using HOOMD-blue on one GPU compared to other parallel codes for multiple CPU cores

Figure 18[33] shows the speed-up gained by using HOOMD-blue for rigid bodies simulations on a single GPU compared to the LAMMPS[34] parallel code on multiple CPU cores.

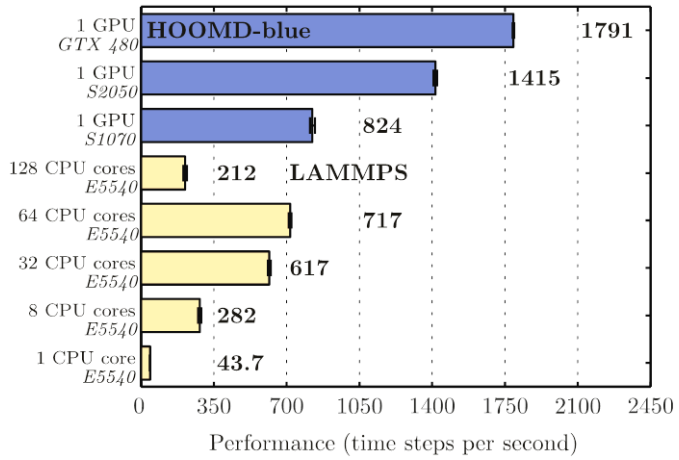

Figure 18 Benchmarks comparing the speed-up achieved for rigid bodies by using HOOMD-blue on one GPU compared to other parallel codes for multiple CPU cores

2.4.2. DLPoly

DLPoly[35] is a parallel molecular dynamics simulation package available free under license. The code is developed at the Daresbury Laboratory in the Imperial College of London. This package was used for the original binary MPMNPs simulations,[9] so it

was used again now to verify the validity of the results obtained using HOOMD-blue in two ways:

- Select ternary and quaternary systems (Chapter 4) were simulated using MD to verify the results obtained using DPD. This was done to guarantee that the coarse-graining introduced by the DPD method was still a good representation of the actual equilibrium state of the system. Once this was established, the bulk of the ternary and quaternary simulations were conducted using DPD to reduce the computing times and resources, which would have been prohibitive otherwise.
- The crystallization results for binary systems of long surfactants (Chapter 6) were also verified using both DLPoly and HOOMD-blue to determine that the results were independent of the code used.

Chapter 3. Previous work

In this chapter we explore previous experimental and computational studies on the structure and composition of SAMs of alkane thiols on gold surfaces. We review results for both homo and mixed ligand monolayers on different substrates, like flat surfaces and nanoparticles of different shapes (spheres, rods, and faceted polyhedra).

3.1. Homoligand self-assembled monolayers

Gold is a relatively inert metal, but has a strong specific interaction with sulfur that allows the formation of the monolayers in presence of many other functional groups. Colloidal gold is usually synthesized in a liquid medium. A self-assembled monolayer of thiol-alkanes is used to stabilize the size of the colloids and prevent them from clumping together.[36] The thiol head (SH) of the surfactant adsorbs on the gold surface, with the alkane tails pointing outwards towards the solvent. Once the first layer of thiol heads has adsorbed on the gold and occupied the entire available surface, no more layers can deposit on top of it, effectively forming a single monolayer of thiol alkanes. This monolayer is densely packed and crystalline. The distance between gold atoms is 2.8 – 3.1Å, and the sulfur heads are 2.2 – 2.6Å from the gold atoms.[37] The thiol groups arrange in a $(\sqrt{3}x\sqrt{3})R30°$ lattice and have a tilt angle between 20° and 30° with respect to the gold surface. Shorter alkyl chains (less than 10 carbons in the surfactant tail) form a more disordered structure with

lower packing density and coverage.[38, 39] The types of interactions which are most relevant to these structural aspects include the bonding interactions between the head group and the substrate, and the intermolecular interactions between adjacent adsorbate molecules. The greater the mismatch between the van der Waals radii of the tail groups and the head groups, and between these quantities and the substrate lattice parameters, the greater the tendency fro the monolayer to deviate from well-arranged structures and to exhibit structural disorder and defects.[38]

It has been shown that the wetting properties of the monolayer depend on the terminal group of the thiol surfactants.[40]

3.1.1. On flat surfaces

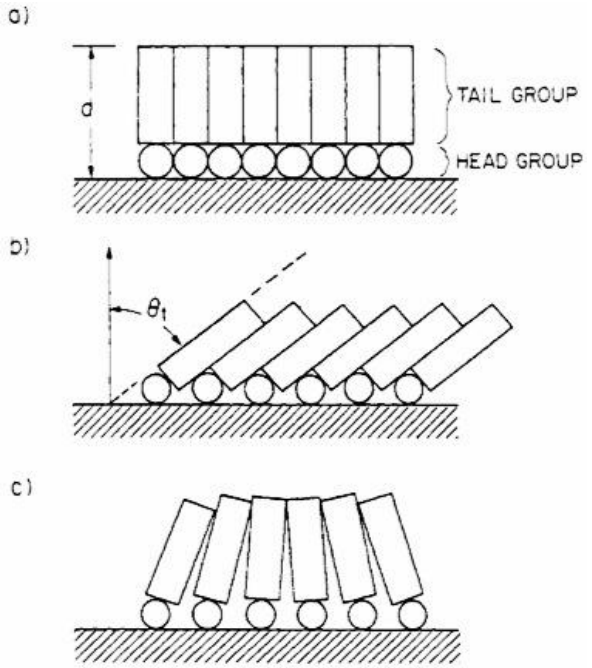

Figure 19 Structural models of SAM in closed packed configurations with tail groups oriented normal to the surface (top) or tilted (middle) or with a distribution of tilted angles (bottom).[38]

Figure 19 shows the possible configurations for the closed-packed monolayers of alkane thiols on a flat surface. The surfactants adsorb on the (111) gold surface. The

experimental observations were confirmed as well by molecular dynamics[41] and Monte Carlo[42] simulations, which were able to reproduce the closed-packed and tilt angle of the ordered surfactant chains. Solvent explicit simulations were also carried out to model the wetting behavior of long-chain SAMs with $-CH_3$ and –OH end groups exposed to water.[43]

3.1.2. On nanoparticles

Gold NPs have been extensively studied because of their chemical stability,[44] optical properties,[45] biological applications,[46] and catalytic activity.[47] The surfactant shell defines most of the properties and interactions of the MPMNP with its environment (i.e. stability, solubility, assembly and electronic properties).[48]

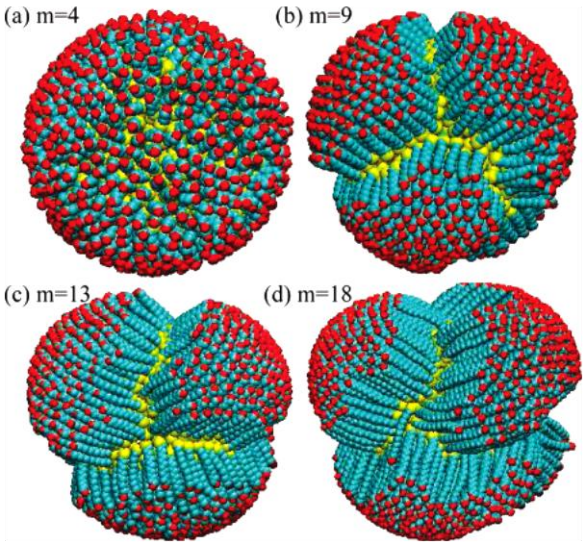

Figure 20 Homoligand alkanethiol [SH-$(CH_2)_m$-CH_3] SAMs for different tail lengths. a) m = 4, b) m = 9, c) m = 13, d) m = 18.[24]

Computational studies of SAMs on spherical gold NPs have been performed using implicit[24] and explicit solvent[49] MD simulations. Figure 20 shows the result form implicit solvent simulation of monolayers of different lengths. Analogous to the results found for flat surfaces, it was shown that a minimum length (>= 9 carbons)

was necessary for the surfactants to form a crystalline structure. Figure 20a shows a disordered monolayer of alkanes that is too short to crystallize. Because of the curvature of the NP, the crystallized ligands shown in Figure 20b-d separate into "bunches" or regimes in which the surfactants are pointed in different directions, much like grains in a crystal. The tilt angle of the surfactants on spherical NPs is larger (20° – 50°) than the tilt angle found on flat surfaces. [24]

3.2. Mixed self-assembled monolayers

Mixed SAMs are formed by combinations of surfactants of different length, tail end group, or both. They were first studied on flat surfaces and their structure was hard to identify. The "islands" or irregular features observed in the monolayer were time dependent and hard to characterize. However, it was understood that the longer surfactants could bend their tails on top of the shorter ones[50] (Figure 21).

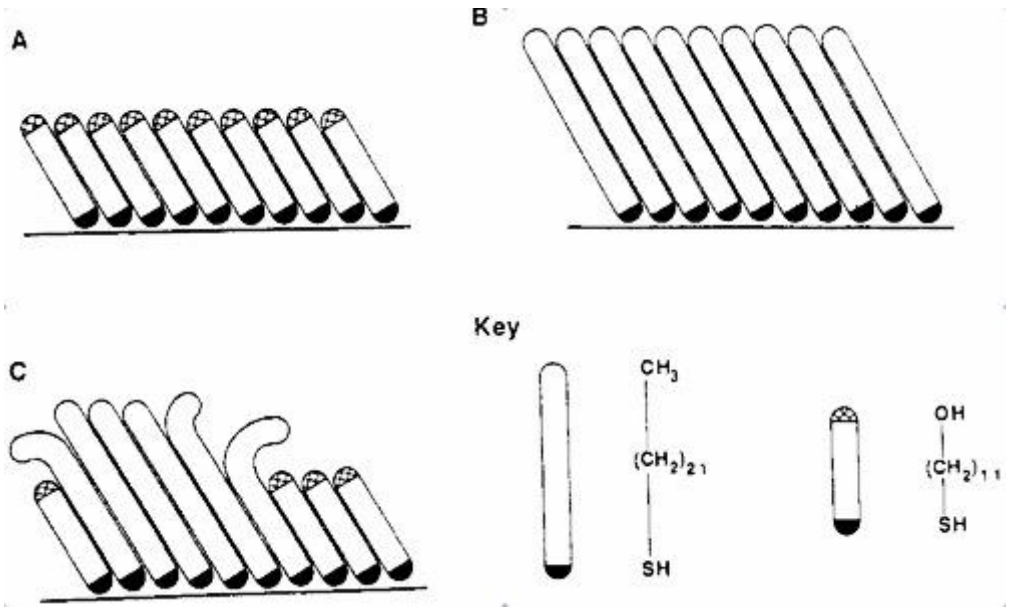

Figure 21 Schematic illustrations of monolayer structures for a) pure HS-$(CH_2)_{11}$-OH, b) pure HS-$(CH_2)_{21}$-CH_3, and c) a mixture of the two thiols[50]

Computer simulations eventually confirmed the separation of the unlike surfactants into disordered and ordered domains,[51] opening the door for the research done by the Stellacci group to fully understand and explain the system of mixed SAMs.

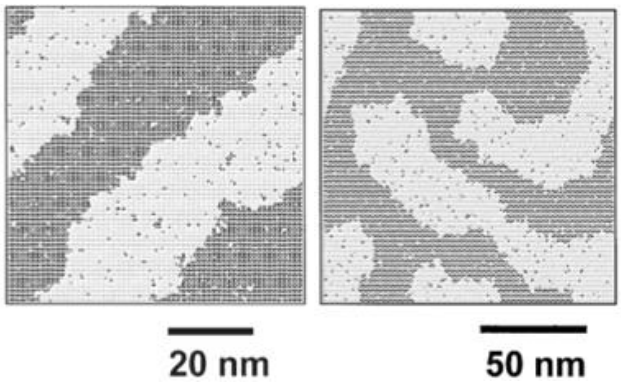

Figure 22 Monte Carlo simulation results of a 256x256 (left) and 128x128 (right) system shown the domain formation.[51]

It is now understood that the mixed monolayers form by co-adsorption of the different surfactants from the mixed solution to the surface of the NPs. Since the species adsorb simultaneously on the NP, they compete with each other.[52] The surfactants on the monolayer are always in dynamic equilibrium with the surfactants in the solution. If the NP is left in solution long enough, eventually the monolayer will become a homoligand monolayer composed by the surfactant that is less miscible in solution.[53] Even if surfactants have the same end group, there are still differences in their solubility with the solvent. In that case, the longer surfactant will be the less soluble. Therefore, to obtain a desired stoichiometric composition it is necessary to perform a trial and error study, in which the NPs are removed form the solution at different times, until the desired stoichiometry is achieved.

3.2.1. On nanoparticles

In 2004, Jackson et al. presented a new class of MPMNPs coated with a binary SAM of hydrophobic and hydrophilic thiol molecules.[8] Scanning tunneling microscopy (STM) and transmission electron microscopy (TEM) images of these particles

showed that the two immiscible ligands distributed in ordered domains (stripes) less than 1 nm wide on the surface of the NP (Figure 4).[54, 55]

Many interesting properties of MPMNPs coated with binary SAMs have been studied, both experimentally and through computer simulations. It was shown that these particles avoid non-specific protein adsorption.[8] This happens because the alternating ripples of hydrophobic and hydrophilic regions are at least one order of magnitude smaller than the proteins' size, so there is a series of attractive and repulsive domains between the protein and the MPMNP's surface that balance each other, resulting in no net attractive force between them. It was also found that two singularities form at the poles of the striped spheres where the aligned stripes collapse into points, as shown in Figure 23a. These singularities have been used to drive directionally specific assembly (Figure 23b).[11,56]

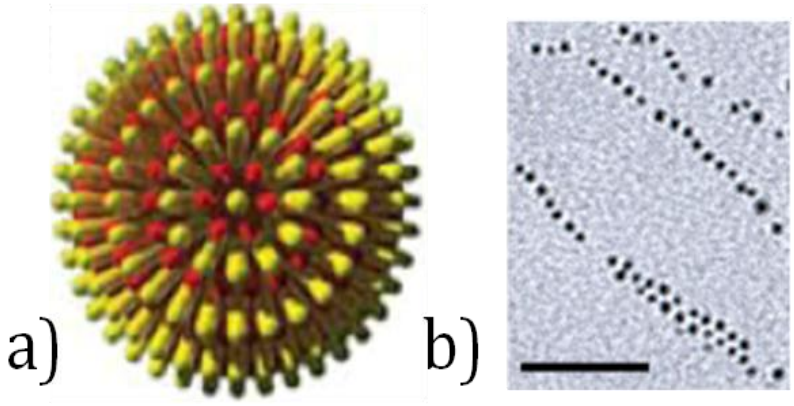

Figure 23 Directionally specific assembly. a) Singularity at the top of a MPMNP. b) TEM image of chains formed by MPMNP. [11]

More recently, it was shown that MPMNPs can penetrate cell membranes in a way that bypasses endocytosis and causes no harm to the cell or membrane.[56] It has been suggested that the penetration of cell membranes by NPs could be a viable path for drug delivery into the cytoplasm, and could potentially help understand the biological mechanism of direct membrane translocation (Figure 24).[57]

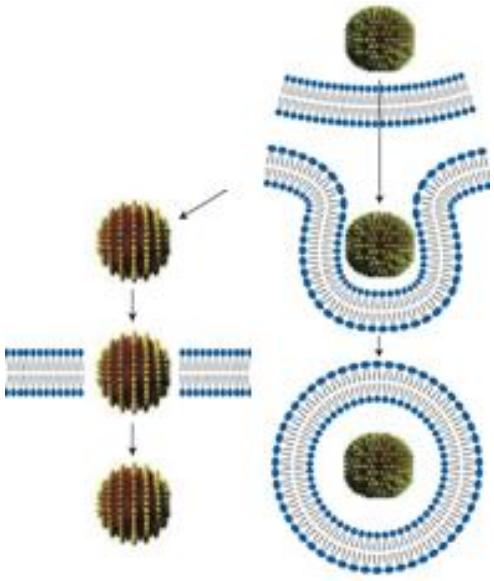

Figure 24 Membrane translocation by striped NP (left) vs. endocytosis (right). [57]

3.2.1.1. Spheres

Atomistic and mesoscale simulations of the system where conducted by Singh et al. to understand the formation of stripes on binary coated MPMNPs.[9] They determined that the stripes form because of competition between enthalpic losses and entropic gains at the interfaces between ligands. Enthalpy and free energy are normally reduced by decreasing the interface between two immiscible surfactants in system, which is known as bulk phase separation. However, longer and bulkier surfactants gain free volume by aligning next to smaller and less bulky ones, thus increasing their conformational entropy. Figure 25 shows a schematic representation of the free volume shared by neighboring surfactants on curved surfaces. This allows the larger bulkier molecules (yellow beads in the figures) to bend their tails on top of the shorter less bulky ones (red beads) as shown in Figure 26, and therefore increase their conformational entropy. When the entropy gain is sufficient to compensate for the penalty in enthalpy due to extra phase boundaries, the surfactants microphase separate into stripe like domains.

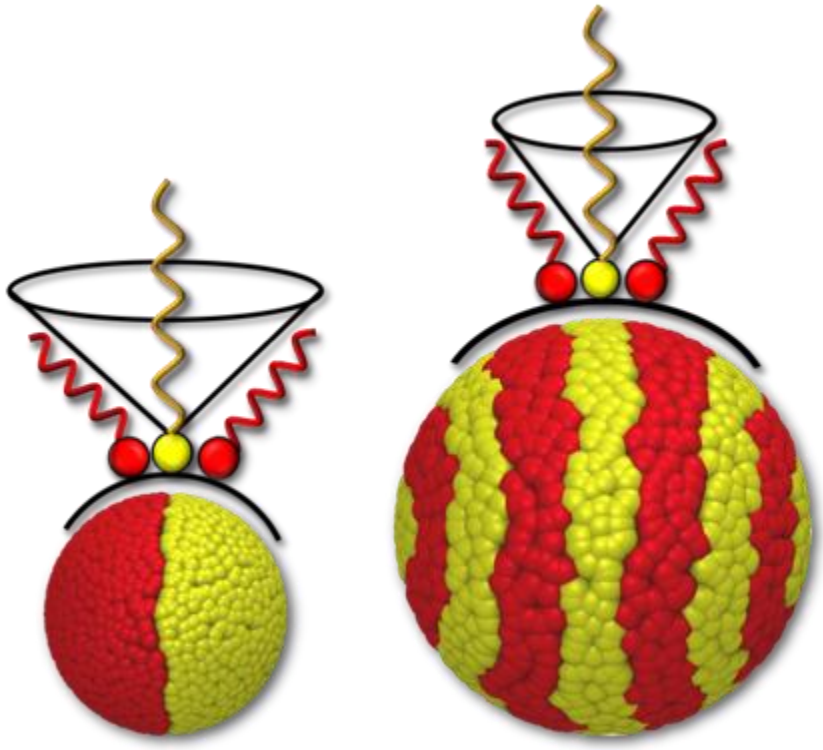

Figure 25 Free volume available for the surfactants' tails on the surface of a NP for high (left) and small (right) radius of curvature.

An attractive feature of binary-coated MPMNPs is that the stripes seen on their surface can be tailored by changing the size of the NP or the stoichiometry and size of the ligands in the SAM.[8,48] It was found experimentally that increasing the NP radius increases the distance between stripes. Changing the stoichiometry of the ligands determines the type of pattern found on the surface, from perfect ripples to discrete or "patchy" domains. Changing the length of the ligands (n-alkane thiol with n = 6 to 12 for the first component and either mercaptopropionic acid or mercaptoundecanoic acid for the second component) changes the height difference between peaks and valleys of the stripes.

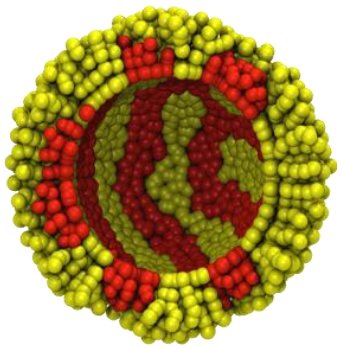

Figure 26 Cross sectional view of simulated striped MPMNP.

Simulations of MPMNPs coated with a binary SAM predicted that for small enough NP radius, the system forms a Janus particle (Figure 27a). This is because the larger curvature of the sphere already provides sufficient free space for the tails (FIGURE) and thus entropic gains are not enough to compensate for the increase in energy. Aligned stripes form on the surface of medium sized spheres (Figure 27b), and as the radius of curvature increases, the stripes become disordered and patches may appear due to kinetic effects (Figure 27c and d).[9]

The effect of the size of the surfactants' tails was also studied for binary SAMs,[9] It was found that when the difference in length or steric size between the two surfactants is not enough to generate sufficient entropic gains, the surfactants completely phase separate instead of forming stripes. On the other hand, even on flat surfaces (or infinite radius of curvature) stripes form if the difference in size between the two surfactants is large enough (Figure 27d).

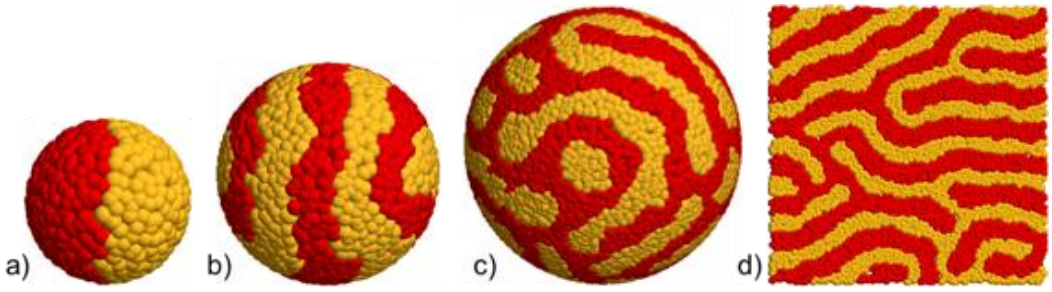

Figure 27 Microphase separation of surfactants in a MPMNP with different curvature. NP radius: a) 3, b) 5, c) 10, d) infinite. Not drown to scale. Tails not shown.[9]

3.2.1.2. Cylinders

On cylindrical surfaces, the stripes were always formed horizontally (Figure 28). It was found that when the stripes align with the vertical axis of the cylinder (Figure 28a) the surfactants become crowded in one dimension (red arrow in the figure) and therefore they are constricted to a smaller free space. However, when they arrange themselves horizontally (Figure 28b), they gain a new dimension of free volume to explore (black arrow). Therefore, this is their preferred orientation. [58]

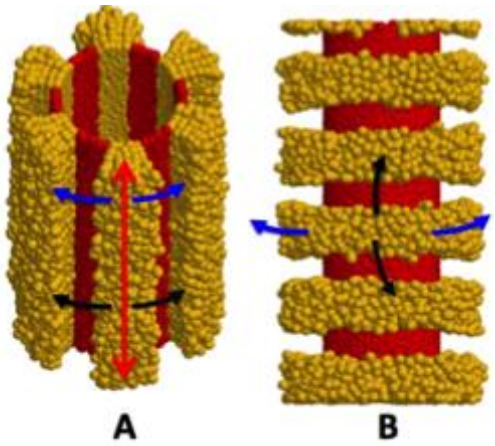

Figure 28 Free volume available for long surfactants (yellow) to explore in a) vertical and b) horizontal stripes. Tails of short surfactants (red) not shown.[58]

The effects of other parameters were also studied for this geometry. The effect of the radius of the cylinder is shown in Figure 29. For smallest cylinder radius, the surfactants separate without forming stripes (periodic boundary conditions are used for the simulation, therefore all of the short, red, surfactant is together in one domain in Figure 29a). This is due to the same curvature effect (FIGURE) that caused the formation of Janus particles on spherical NPs. The length of the cylinder had no effect on the width of the stripes formed. Varying the stoichiometry of the SAM to extreme values were one of the surfactants was in excess, caused them to form 2D-micelles patterns (like the ones found for flat surfaces) instead of stripes. [58]

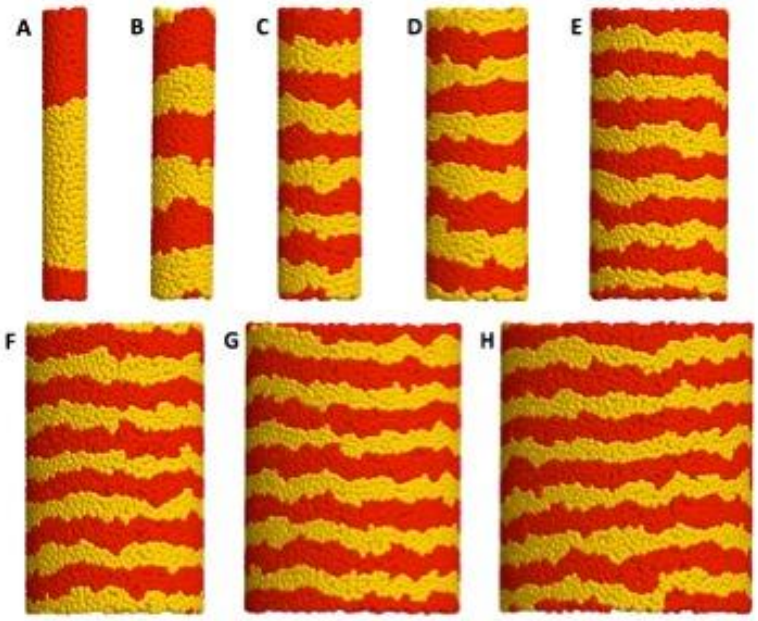

Figure 29 Effect of cylinder radius on phase-separated pattern in mixtures of short (red) and long (yellow) surfactants. The radii of the cylinders are: a)2, b) 3, c) 4, d) 5, e) 7, f) 9, g) 11, h) 13. Tails not shown.[58]

3.2.1.3. Faceted particles

For faceted particles coated with a binary SAM, it has been predicted that longer and bulkier surfactants prefer to occupy the edges of the NP rather than its flat faces. In this case, a similar effect as that of the curvature of spherical particles is observed. The edges of the facets provide the surfactant with a greater available free volume, and therefore this is their preferred position.[59] However, the results presented in Figure 30 are only valid for systems with very off-critical stoichiometries (the long surfactant is present in concentrations <10%) because they were obtained through a highly coarse-grained theoretical model. Simulations need to be performed to study the patterns that will form when the longer surfactant is present in higher concentrations, after all the available edges have been filled and it is forced to interact with the short one on the faces of the polygons.

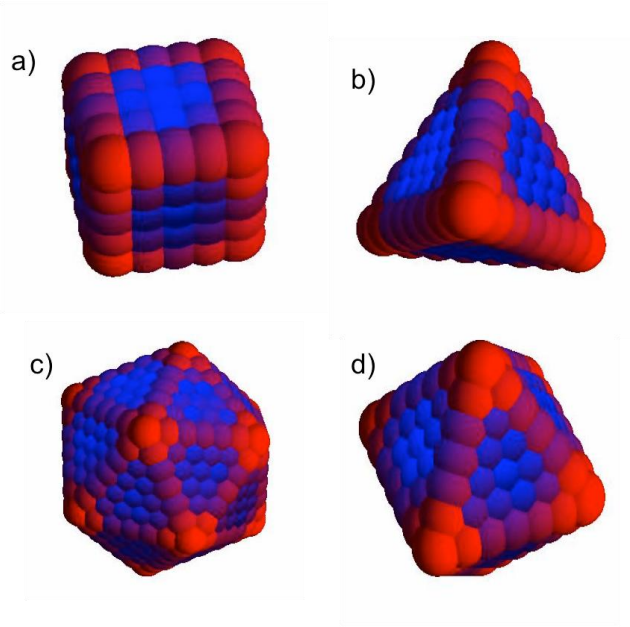

Figure 30 Preferred lattice positions occupied by long (red) and short (blue) surfactants for faceted surfaces: a) cube, b) tetrahedron, c) icosahedron, and d) octahedron. Tails not shown.[59]

3.2.2. On flat surfaces

The patterns formed by binary SAMs on flat surfaces were also studied.[58] Figure 31 shows the effect of stoichiometry of the SAM on the patterns formed. For very small interbead repulsion (Figure 31a) no stripes are observed because the immiscibility between unlike surfactants is not enough to force the minimization of interface length. However, as the repulsion between beads increases, stripes are found for stoichiometries near the 1:1 critical point. When one of the surfactants is in excess, then it forms a continuous matrix in which 2D-micelles of the other surfactant are dispersed. For these systems, the effect of surfactant length was also studied. It was found that for small length difference between surfactants, no stripes were formed. In those cases, the gain in free volume that would derive from forming stripes was not enough, and therefore the surfactants completely separated into two domains.

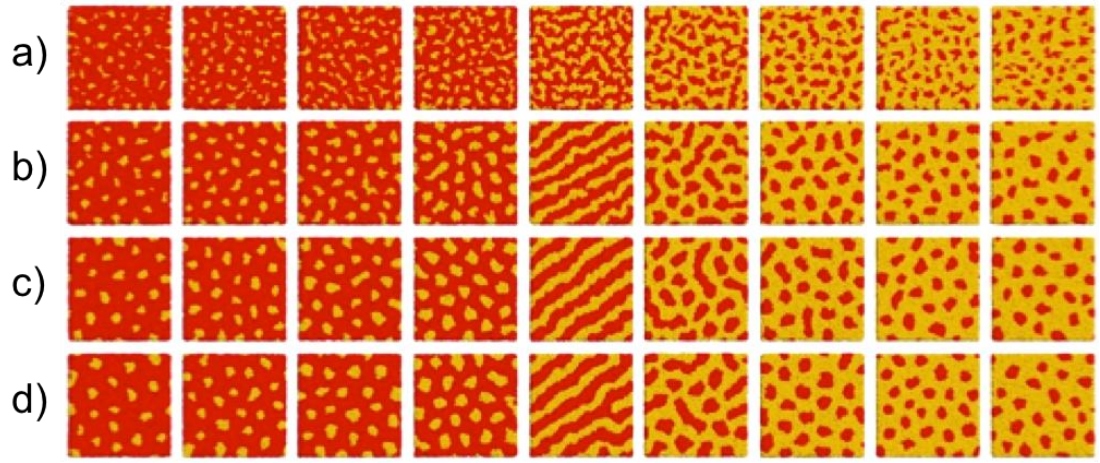

Figure 31 Simulation snapshots of microphase separation in asymmetric mixtures of short (red) and long (yellow) surfactants for increasing fraction of long surfactant. Interbead repulsion is a) 20, b) 25, c) 30, and d) 35. Tails not shown.[58]

Chapter 4. Assembly of monolayers on spherical nanoparticles

In this chapter we will describe the types of patchy patterns that can be found on mixed SAMs of alkanethiols. The patterns are organized into different groups depending on the symmetry and base pattern of the monolayer. The simulations were performed using DPD, but key results very verified using MD. The results presented in this work are for spherical nanoparticles, but we show how they can also be extrapolated to flat surfaces and nanorods. To produce the results presented in this Chapter, all simulations were ran for at least 30 million time steps. To explore the effect of all parameters, we performed a total of 4280 production runs averaging 10 GPU-hours per run.

4.1. Patchy patterns

The patchy patterns found for ternary and quaternary SAMs have been divided into different groups according to their base pattern. In all cases, red is the shortest surfactant and yellow is the longest. Blue and green are intermediate length surfactants, with green being longer than blue. Only the heads of the surfactants are shown for DPD simulations to simplify the recognition of the pattern formed.

4.1.1. Decorated striped particles

The striped patterns are shown in Figure 32. The top row shows the base striped patterns, and the following rows show different modifications that can be done to this patterns following the design rules which will be discussed in Chapter 5.

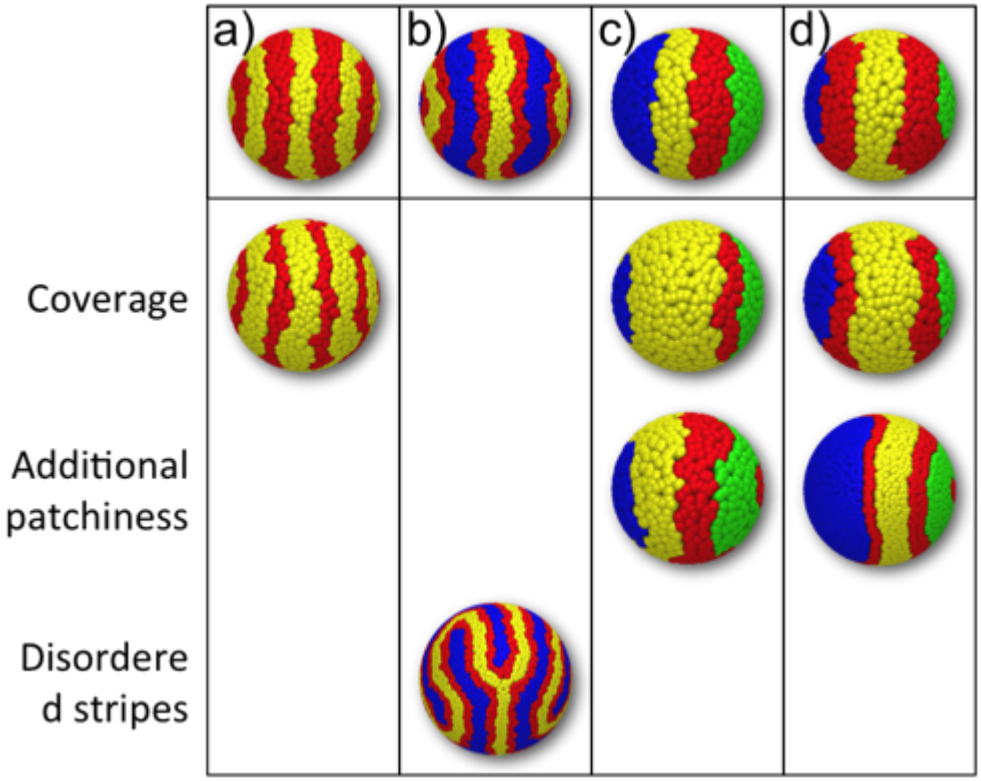

Figure 32 Decorated striped patterns. Tails not shown. Red: short, blue: medium, green: long, and yellow: longest surfactant. a) Striped particle, b) alternating stripes particle, c) four stripes particle, d) decorated Neapolitan particle. The bottom rows show possible variations to the patterns shown on the top row.

Figure 32a shows the original striped pattern found for binary SAMs on spheres[9], and directly underneath it is another version of the same pattern with different stripe width. Figure 32c shows the base ternary pattern, which was named Alternating Stripes[61] because the medium (blue) surfactant forms one single stripe that coils all the way around the NP, and is always separated from the long (yellow) surfactant by a stripes of the red (short). This arrangement in which the short (red)

surfactant separates the two longest ones (blue and yellow) is preferred because it maximizes the length differences between surfactants that share an interface, and therefore maximizes conformational entropy. On the bottom of that same column it is shown the alternating stripes pattern with disordered stripes

Figure 32c shows the simplest quaternary case, in which the four surfactants form one single stripe around the NP.[62] The longest surfactant (in yellow) has an interface with the two shortest ones (in red and blue). Also, the two longest surfactants (yellow and green) both have an interface with the shortest (red). This pattern is found for a system with two short surfactants (*i.e*. 3, 4, 7 and 8 beads) and low interbead repulsion between unlike beads (a_{ij} = 30), when the overall length of the surfactants is relatively short compared to the NP size (*i.e*. all surfactants are less than 10 beads long). This pattern is also prevalent when the two shortest surfactants are in very low concentrations (≤ 20% of each), an example of which is shown directly underneath Figure 32c. The bottom-most pattern shown underneath Figure 32c shows a modified where there is one additional patch of the short surfactant (in red) inside the domain formed by the second longest surfactant (green). This case occurs under a very narrow range of conditions, for a system with two short surfactants (*i.e*. 3, 4, 8 and 9 beads) with low interbead repulsion between unlike surfactants (a_{ij} = 30), when the overall length of the surfactants is longer than the case for Figure 32a.

Figure 32d shows a striped quaternary pattern where the short surfactant (in red) forms two stripes around the NP, instead of just one. [62] These two stripes separate the longest surfactant (in yellow) from the two medium length surfactants (in blue and green). This pattern is found for large NP radius (NP radius > 4) and high interbead repulsion between unlike beads ($65 < a_{ij} \leq 350$). In systems with large NP radius, the surfactants have less available space to explore with their tails,[9] and therefore the longest surfactant (yellow) prefers to increase its interface with the short one (red). This pattern can also be found in systems were the medium

surfactant (blue) is in the lowest concentration (≤ 10%), so there is not enough of it available to create sufficient interfaces with the longest one (yellow).

The two patterns shown underneath Figure 32d are additional variations to this pattern, the first one by changing the coverage and width of the stripes. The second one, by adding an additional patch of the small surfactant (in red) inside the domain formed by the second longest (in green). This pattern is found also for large NP radius, but for smaller repulsion between unlike beads (a_{ij} = 65)

4.1.2. Decorated Janus particles

Janus particles are a macrophase separated pattern formed by two domains, one in each side of the NP. They were named after the double-faced Roman God custodian of the universe.[63] The simplest example is found for binary mixtures of unlike surfactants[10] and is shown in Figure 33a. The image directly underneath it shows a possible variation of this pattern, where the two domains are not of equal size.

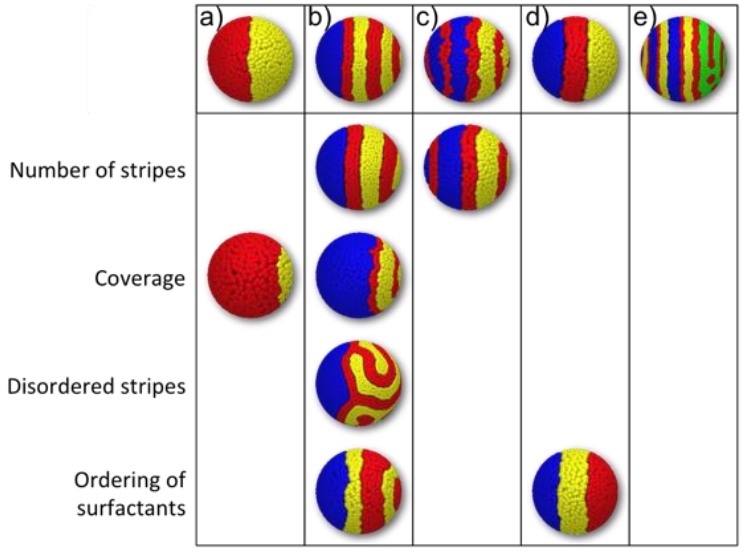

Figure 33 Decorated Janus patterns. Tails not shown. Red: short, blue: medium, green: long, and yellow: longest surfactant. a) Janus particle, b) with stripes on one side, c) with stripes on both sides, d) Neapolitan particle, e) Janus particle with alternating stripes on one side and stripes on the other side. The bottom rows show variations to the patterns.

Figure 33b shows a decorated Janus NP with stripes on one side. This pattern occurs for ternary mixtures of surfactants,[61] and is characterized by the medium (blue) surfactant separating from the other two. The shortest (red) and longest (yellow) surfactants form stripes on the other side of the Janus particle, and behave exactly like they would in a binary system. The separation of the medium (blue) length surfactant is expected and analogous to the case observed previously for the Alternating Stripes pattern. Possible variations to this pattern include changing the thickness of the stripes, the coverage of the Janus NP, disorder of the stripes, and changing of the order of the surfactants. This last variation deserves special attention, and it's shown as the bottom-most image below Figure 33b. In this case, an interface between the yellow (long) and the medium (blue) length surfactant can actually be forced to occur. This will be discussed in detail in the following chapter.

Figure 33c shows a Janus NP decorated with stripes on both sides, and also occurs for ternary SAMs. [61] The number and thickness of the stripes can also be easily controlled. Another possible variation for ternary SAMs is the formation of a Neapolitan particle, [61] shown in Figure 33d. In this particle, the short (red) surfactant forms one single stripe separating the two longest ones (blue and yellow). This ordering can also be modified, as shown below Figure 33d, by forcing the longest (yellow) surfactant to be the one forming the stripe between the two shortest (red and blue).

Finally, Figure 33d shows a quaternary Janus NP decorated with stripes on both sides.[62] The two shortest surfactants (in red and blue) form an alternating stripe pattern[61] with the longest surfactant (yellow) on one side of the Janus particle, while the second longest surfactant (green) forms a striped pattern with the shortest one (red) on the other side of the NP. This pattern is found for large NP radius (> 4) and low interbead repulsion between unlike beads (a_{ij} = 30), and is analogous to the pattern observed under similar conditions for ternary systems.[61]

4.1.3. Decorated Cerberus particles

We observe several types of patterns where three of the surfactants macrophase separate into dominant features. The simplest case, found for ternary SAMs, is shown in Figure 34a.[61] The Cerberus particle is the ternary analogue of a Janus particle, and we therefore named it after the Roman and Greek three-headed dog guardian of the gates to the underworld.

Figure 34b shows a quaternary Cerberus NP that is decorated with a stripe of the shortest surfactant (shown in red) separating the three longest ones.[62] We observe this particular pattern when the system has one short surfactant and three long ones (*i.e.* 3, 7, 8 and 9 beads) and the repulsion between unlike surfactants is low (a_{ij} = 30). In this case, all three long surfactants compete to form an interface with the short one to maximize the free volume available for their tails to explore. The pattern directly underneath Figure 34b shows the possibility to control the width of the stripe formed by the short (red) surfactant.

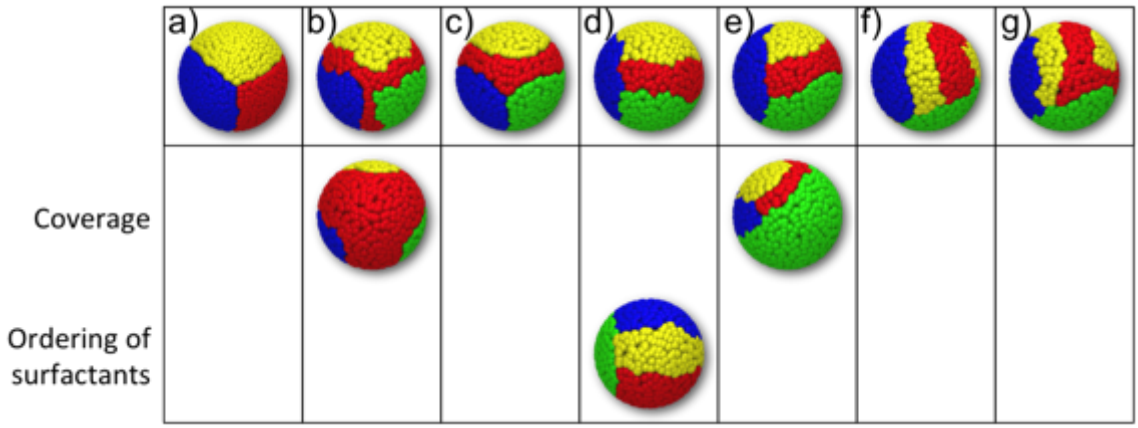

Figure 34 Decorated Cerberus patterns. Tails not shown. Red: short, blue: medium, green: long, and yellow: longest surfactant. a) through g) show different patterns, and the bottom rows show possible variations of those patterns.

Figure 34c shows a Cerberus pattern in which the longest surfactant (shown in yellow) is separated from all others by the short one (shown in red), while the two

medium length surfactants (shown in blue and green) share an interface.[62] This pattern also forms when there is one short surfactant in the system and three long ones (*i.e*. 3, 7, 8, and 9 beads) but when the interbead repulsion between unlike surfactants is high (a_{ij} = 65). In this case the system's free energy is minimized by minimizing the number of interactions between the longest (yellow) and the two medium surfactants (blue and green).

In Figure 34d the short surfactant (red) separates only the two longest ones (green and yellow). Both of these long surfactants have an interface with the medium one (blue).[62] This pattern forms when the surfactants have an equal length difference (*i.e*. 3, 5, 7, and 9 beads) and the interbead repulsion between unlike surfactants is high (a_{ij} = 65). Since the medium surfactant (blue) is relatively short compared to the two longest ones (green and yellow), both of them gain conformational entropy by forming an interface with it.

An analogous pattern to Figure 34d is shown underneath it. However, the arrangement of the surfactants is not the same between these two patterns. In this last case, there are three short and one long surfactant in the system (*i.e*. 3, 4, 5, and 11 beads) and the interbead repulsion between unlike beads is high (a_{ij} = 65). In this case, the longest surfactant (yellow) maximizes its interface with the two shortest (red and blue), and also has a smaller interface with the second longest (green).[62]

Figure 34e is similar to Figure 34d, with the difference that the stripe formed by the short surfactant (red) curves towards the longest (yellow) surfactant to increase the length of the interface between the two longest surfactants (in green and yellow) and the shortest one (in red). This pattern is obtained for SAMs formed by surfactants of symmetric lengths (*i.e*. 3, 5, 7, and 9 beads) and low interbead repulsion between unlike surfactants (a_{ij} = 30). Therefore, this pattern occurs under similar conditions to Figure 34d, with the only difference that the interbead repulsion between unlike surfactants is smaller for Figure 34e, which is why the surfactants prefer to form a longer interface.[62] A variation of this pattern is shown directly underneath it, in which the width if the stripe has changed.

In Figure 34f the short surfactant (shown in red) forms a single stripe inside the domain of the longest surfactant (shown in yellow).[62] The stripe also has interfaces with the second longest surfactant (shown in green), but none with the medium surfactants (shown in blue). This pattern occurs for three short surfactants (*i.e.* 4, 5, 6 and 11 beads) when the interbead repulsion between unlike surfactants is low (a_{ij} = 30).

Figure 34g is a sub-case of Figure 34f, in which the stripe of the short surfactant (red) becomes a fully closed circle creating a larger interface with the second longest surfactant (green).[62] This case also occurs for three short surfactants and low interbead repulsion between unlike beads, but only for very short surfactants with respect to the NP radius (3, 4 and 5 beads long for the shortest surfactants, up to 9 beads long for the longest).

4.1.4. Spotted particles

Figure 35 shows spotted patchy particle for different numbers of surfactants in the monolayer. This type of pattern is found when the short surfactant (in red) is in excess (>50%) of the other ones. The longest surfactants form circular 2D micelles – spots – that are dispersed in a continuous matrix of the short one.[58,61,62] The number and size of the spots can be modified as shown in the bottom row of Figure 35.

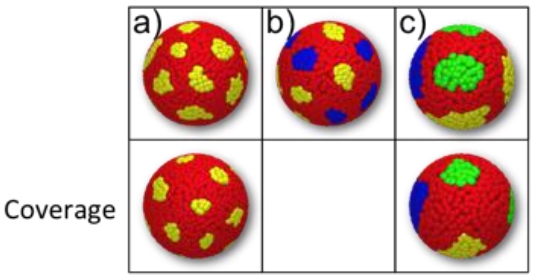

Figure 35 Spotted particles. Tails not shown. Red: short, blue: medium, green: long, and yellow: longest surfactant. a) Binary, b) ternary and c) quaternary spotted particle. The bottom row shows possible variations for the patterns showed on the top row.

4.1.5. Tetrahedral particles

Figure 36 shows a quaternary patchy particle with tetrahedral symmetry in the SAM pattern. We refer to this particle as a tetrahedral particle.[62] This pattern minimizes the interface between all surfactant pairs. Moreover, the three longest surfactants (shown in blue, green and yellow) all have an interface with the shortest surfactant (shown in red in Figure 36a). When viewed from the top, this particle looks exactly like a Cerberus particle found in the ternary systems[61] as shown in Figure 36b. The tetrahedral particle forms in cases when the surfactants are very long compared to the NP radius (*i.e.* all surfactants are at least 10 beads long, for a NP radius of 4), but the length difference between the four surfactants is relatively small (no more than six beads difference between the shortest and longest surfactants).[62]

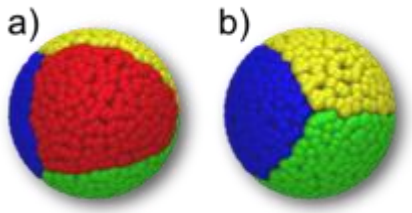

Figure 36 a) Top and b) bottom view of a tetrahedral particle. Tails not shown. Red: short, blue: medium, green: long, and yellow: longest surfactant.

4.1.6. Brahma particles

Figure 37 shows a patchy particle with the SAM separated into equal quadrants; we refer to this particle as the Brahma particle,[62] in reference to the Hindu god of creation who is traditionally depicted with four heads. Here the surfactants again separate without forming stripes, but now each surfactant forms an interface with only two of the others. The two longest surfactants (shown in yellow and green) do not share an interface, and both form an interface with the two shortest surfactants (shown in red and green). This pattern forms when the SAM is comprised of two

short and two long surfactants (*i.e.*, the surfactants are 5, 6, 13 and 14 beads long respectively, for a NP of radius 4).

Figure 37 Brahma particle. Tails not shown. Red: short, blue: medium, green: long, and yellow: longest surfactant.

4.2. Validation of results

The DPD patterns were validated by running less coarse-grained MD simulations for a few key systems. The comparison of the DPD and MD results is shown in Figure 38. Figure 38a and b show the reproduction of the Cerberus and alternating stripes patterns using MD simulations, and Figure 38c and d show the reproduction of the tetrahedral and Brahma patterns. There is good agreement between both simulation methods.

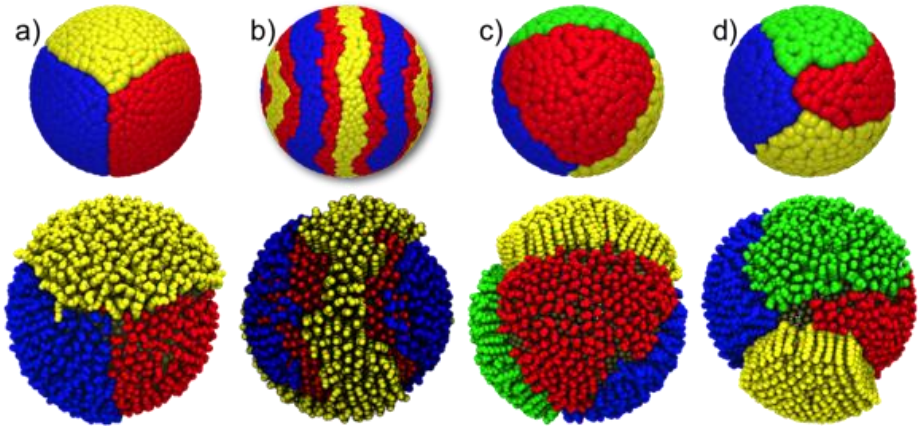

Figure 38 Comparison of DPD (top row) and MD (bottom row) patterns for ternary and quaternary SAMs. Ternary patterns for a) low and b) higher interbead repulsion, and quaternary patterns for c) low and d) higher interbead repulsion between unlike surfactants. DPD tails not shown. MD tails shown. Red: short, blue: medium, green: long, and yellow: longest surfactant.

4.3. Patchy patterns on flat surfaces and cylinders

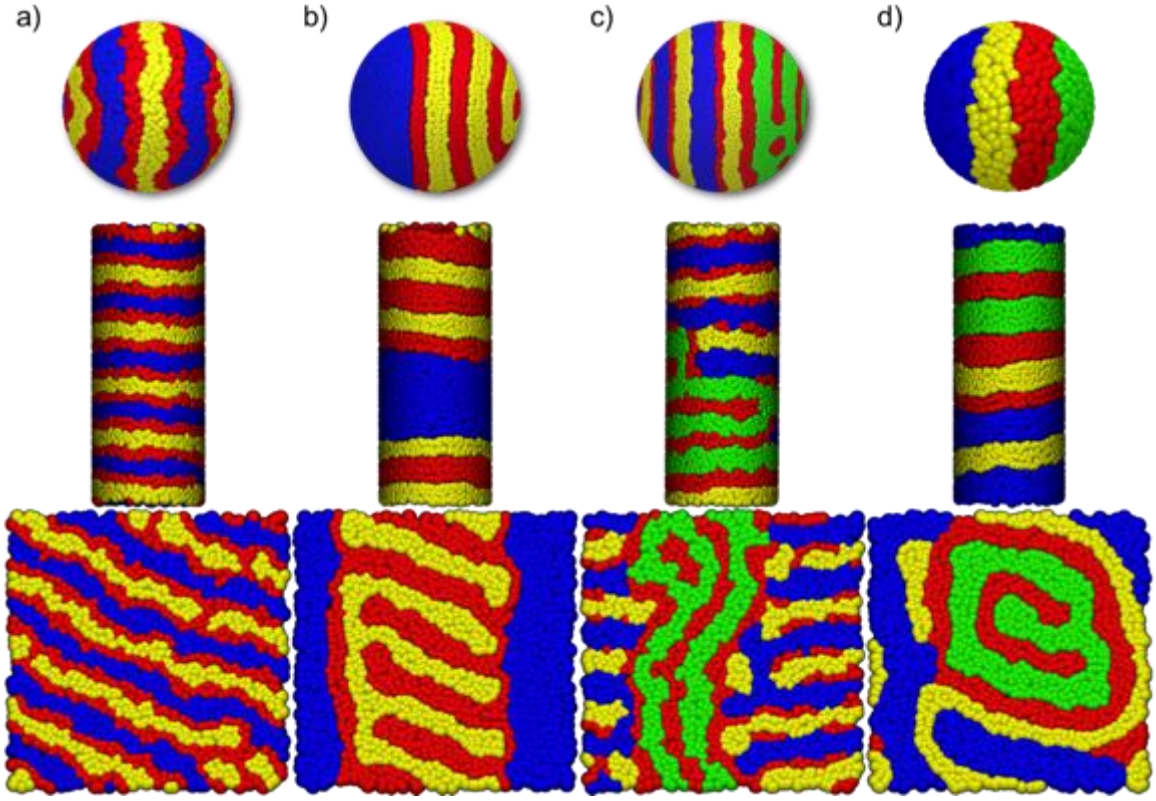

Figure 39 Comparison of ternary and quaternary patterns on spheres (top row), cylinders (middle row) and flat surfaces (bottom row). Ternary patterns for a) low and b) higher interbead repulsion, and quaternary patterns for c) low and d) higher interbead repulsion between unlike surfactants. Red: short, blue: medium, green: long, and yellow: longest surfactant. Tails not shown. Not drawn to scale.

Figure 39 shows some key ternary and quaternary patterns reproduced on cylinders and flat surfaces. The cylinders have a radius of 4σ and a length of 24σ, and the flat surfaces are $24\sigma \times 24\sigma$. For both ternary patterns (Figure 39a alternating stripes, and Figure 39b striped Janus) we see perfect agreement between the patterns formed on all geometries. There are some discrepancies for the quaternary patterns, especially for the stripes pattern shown in Figure 39d. For spheres, we see that the yellow and blue surfactants are separated on both hemispheres of the NP,

and therefore they do not share an interface. However, for cylinders and flat surfaces this is no longer a possibility, because of the continuity of the pattern due to periodic boundary conditions. Therefore, we see some interfaces on the cylinder and flat patterns (like the blue-green interface seen on the rightmost cylinder) that were not necessary on a sphere. However, for all quaternary geometries we see a marked preference for the shortest (red) surfactant to form interfaces with the two longest (green and yellow), and for the longest (yellow) not to form interfaces with the second longest (green).

To verify that size effects were not playing a role in the patterns found, we also performed simulations for $L = 50\sigma$ and $L = 100\sigma$, and compared them to the results from using $L = 24\sigma$. The results for ternary flat surfaces are shown in Figure 40, in which we can see that the pattern remains the same regardless of the size of the system, but the stripes become disordered with larger system size. This phenomenon has also been observed for spheres with both binary[58] and ternary[61] monolayers previously.

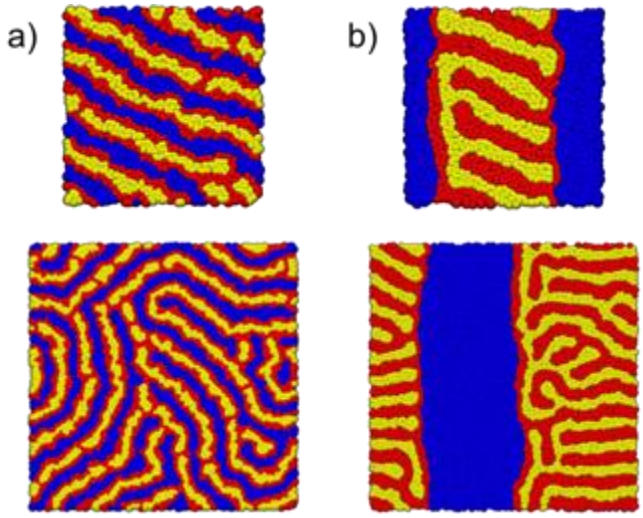

Figure 40 Ternary patterns for large systems size in flat surfaces. Top row: L = 24σ; bottom row: L = 50σ. Ternary patterns for a) low and b) higher interbead repulsion between unlike surfactants. Red: short, blue: medium, and yellow: longest surfactant. Tails not shown. Not drawn to scale.

4.4. Comparison of binary, ternary, and quaternary SAMs

Some of the results found for quaternary MPMNPs have relatively low symmetry. To understand this unexpected behavior, we compared those patterns with those found for binary and ternary NPs in Figure 41. We discussed previously how the Cerberus and Brahma particles are the ternary and quaternary equivalents, respectively, to the Janus particle found for binary MPMNPs. In Figure 41 we also show how the Janus pattern is the base for most of the patterns found on ternary SAMs, and the Cerberus pattern is the base for most of the patterns found on quaternary SAMs. Of course, there are exceptions to this behavior, like the alternating stripes pattern on ternary[61] SAMs and the tetrahedral, Brahma and decorated stripe patterns on quaternary SAMs.[62]

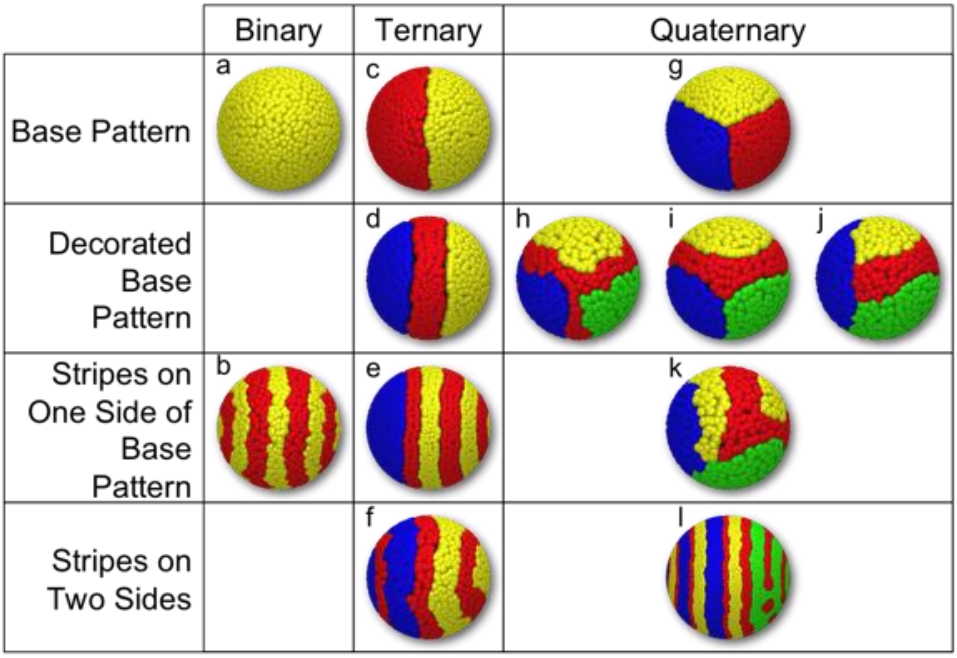

Figure 41 Comparison of binary, ternary and quaternary patterns found on MPMNPs. Tails not shown. Red: short, blue: medium, green: long, and yellow: longest surfactant.

As shown in Figure 41, for binary MPMNPs the base pattern is a NP coated by a single surfactant (Figure 41a), and this can only be decorated with stripes on one side of the pattern (Figure 41b). However, when we move to ternary MPMNPs, we increase the number of possible options. In this case, the base pattern is a Janus particle (Figure 41c), which can be decorated with a single stripe separating the two sides of the Janus particle to form a Neapolitan particle (Figure 41d), or stripes in either one (Figure 41e) or two (Figure 41f) sides of the NP. In doing this, certain symmetries in the patterns are broken. For example, the Neapolitan pattern (Figure 41d) and the Janus pattern with stripes on both sides (Figure 41f) have higher symmetry when the difference in tail lengths is disregarded. The least symmetric pattern for ternary MPMNPs is the striped Janus NP (Figure 41e), where there are stripes on only one side of the NP.

In the case of quaternary MPMNPs, the introduction of the fourth surfactant further increases the number of possible patterns that can be constructed. The base pattern now is a Cerberus particle (Figure 41g), which is further decorated by the addition of the fourth surfactant. Analogous to the formation of Neapolitan particles (Figure 41d) for the ternary case, a stripe may separate all sides of the Cerberus particle (Figure 41h), or only two sides of the Cerberus particle (Figure 41i), or even just one side (Figure 41j). With each of these patterns, the symmetry successively decreases. Similarly, we found a quaternary pattern in which there are stripes only on one side of the NP (Figure 41k), and thus two sides without stripes.

However, instead of a Cerberus particle with stripes on two sides, which would be the quaternary equivalent of Figure 41f, we find a Janus particle with stripes on both sides (Figure 41l). In this case it is symmetry that drives the system to form this Janus particle with stripes on both sides, instead of forming a Cerberus pattern with stripes on two sides and one stripe-less side. In the previous cases (Figure 41h-k) there was no option that offered more symmetry to the system, so the asymmetric patterns formed instead.

With this, it becomes clear that introducing additional surfactants in the monolayer is a way of introducing additional anisotropy to the resulting MPMNPs. Since higher anisotropy of the patterns can guide increasingly more complicated assemblies of NPs, this approach to produce anisotropic building blocks could provide a novel route to obtain higher order structures not possible with high symmetry NPs.

Chapter 5. Rules for the design of patchy particles

In this chapter we present the phase diagrams from varying all possible parameters of the MPMNP for ternary and quaternary SAMs. This explains in greater detail the reasons why the patterns shown in Chapter 4 are formed. We look at the effect of changing the radius of the NP, the degree of immiscibility between unlike surfactants, the stoichiometric composition of the SAM, and the length difference between unlike surfactants. All these parameters have direct correlation with relatively easy to control experimental parameters. The goal is to provide a design rules to guide future experiments and simplify the selection of the necessary parameters to obtain the desired pattern. The phase diagrams also show the robustness of the patterns, meaning that for each desired pattern there is a range of the parameters in which the pattern occurs.

5.1. Effect of nanoparticle size and degree of immiscibility

The effects of NP radius and interbead repulsion for ternary SAMS are studied in Figure 42. Unlike surfactants separate without forming stripes for the smallest NP radius studied. When the curvature of the NP provides enough free volume for surfactant tails to explore, the possible entropic gains from stripes are not enough to overcome the energetic penalties. The analogous effect is observed for binary

systems, where a Janus particle forms for smaller NP radius.[60] As seen in Figure 42, for ternary systems a Cerberus particle is formed when the three surfactants adopt the minimum interface possible between them.

As NP radius increases, the surfactants arrange themselves into stripped patterns. For the conditions of Figure 42, the short surfactant (red in the Figures) is always between the long (yellow) and medium (blue) ones, providing enough length difference to support the formation of the stripes.

For smallest interbead repulsion (a_{ij} = 30), a pattern with Alternating Stripes is formed. In this pattern, the medium and long surfactants form alternating stripes with the short one always in between them. As NP radius increases, this pattern evolves from ordered to disordered stripes, as observed in Figure 42 for a NP radius = 8. From the Alternating Stripes pattern it is evident that the entropic gains are only enough to form stripes when either the long or medium combine with the short surfactant. However, the entropy gain from stripes formed between the medium and the long are not enough and therefore these types of stripes are not seen. Since the length difference between the short and the medium, and the medium and the long is the same (3 beads) (and therefore the gain in free volume is the same), but stripes are only seen for the first case, it becomes evident that the relative length of the surfactants with respect to the NP radius is also an important factor in the formation of stripes. This effect will be discussed in the next section.

For higher interbead repulsion (a_{ij} > 30), different stripped patterns appear. The Cerberus particle transitions into a Neapolitan particle, where three stripes are formed. In this pattern the long and medium surfactants occupy the two poles of the NP, while the short surfactant forms a single stripe in between them. As the NP radius increases, the short surfactant begins to form stripes with the long surfactant on one face of the NP while the medium length surfactant remains separated on the other face, forming a Stripped Janus particle. The long and short surfactants behave like they would on a binary system, with increasing number and disorder of stripes as the NP radius increases.[9]

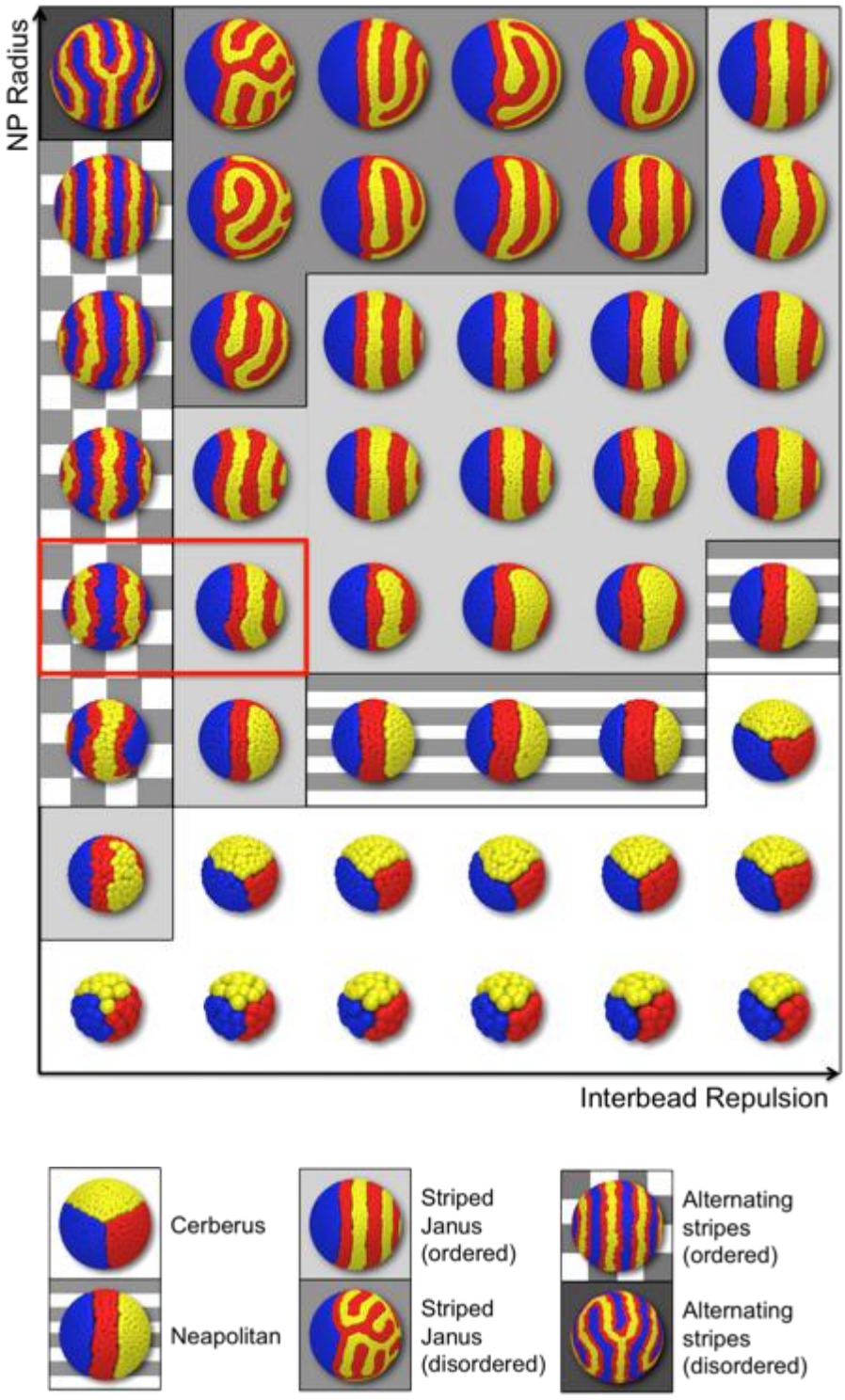

Figure 42 Effect of interbead repulsion vs. NP radius on ternary SAMs. Tails not shown. Length of surfactants is 3 (red), 6 (blue), and 9 (yellow) beads. Composition

of SAM is 1:1:1. NPs not drawn to scale. Radius of NPs in top row is eight times that of bottom row. Interbead repulsion increases from 30 to 365 from left to right. Different patterns are highlighted in shadowed regions. For systems highlighted by red rectangle, effect of surfactant length SAM stoichiometry has been shown in Figure 47 and Figure 48 respectively.

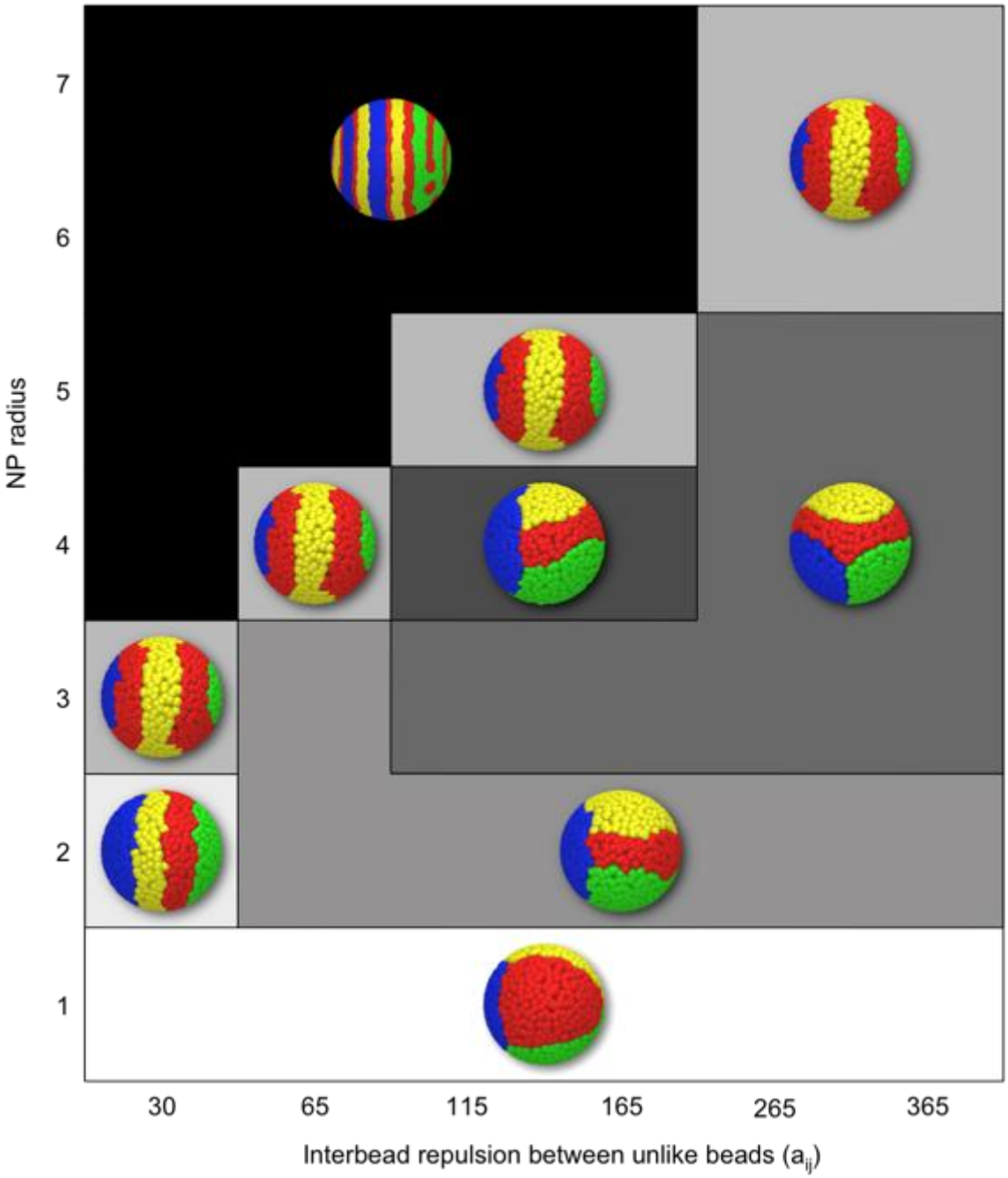

Figure 43 Effect of NP radius on quaternary SAMs for fixed surfactant lengths. The NP radius is varied from 1 to 7, and the interbead repulsion between unlike beads,

which controls enthalpic immiscibility, is varied between 30 and 365. NPs not shown to scale. Tails not shown. Red: short, blue: medium, green: long, and yellow: longest surfactant.

Increasing interbead repulsion increases the energetic penalties for forming stripes. A smaller radius of curvature (i.e. less available free volume for the tails) is needed before the striped patterns are favored. This means that as the interbead repulsion increases, the transition from Cerberus to Neapolitan to Striped Janus requires higher increments in the NP radius to occur.

Figure 43 shows the effect of varying the same parameters for quaternary SAMs. The trends are similar to those found for ternary SAMs. For smallest radius the surfactants macrophase separate into a tetrahedral particle. As the radius of the NP increases, stripes begin to form as it becomes necessary to increase the interface between surfactants of different lengths to maximize conformational entropy gains. Analogous to the Neapolitan pattern for ternary SAMs, the four-striped pattern emerges for quaternary SAMs. Largest NP radius and small interbead repulsion force the maximization of the interface length, eventually resulting in a Janus NP with alternating stripes on one side and simple stripes on the other side. Highest immiscibility between unlike particles results again in macrophase separation, by the formation of decorated Cerberus patterns.

5.2. Effect of surfactant length

Figure 44 shows the effect of surfactant length on the formation of ternary patterns. A tridimensional space was studied, where the length of each surfactant corresponds to each dimension. In Figure 44a, a view of the effect of the length of the short and medium surfactants is shown, and the axis corresponding to the long surfactant is not presented. For relatively short surfactants with respect to the NP radius, a Striped Janus particle is observed. As the length of the surfactants increases with respect to the NP radius, the system evolves to Neapolitan and

Cerberus particles. The stripes are lost because the length difference between the surfactants does not provide enough entropic gains to overcome the high energetic penalties due to having long chains of unlike beads forming interfaces. This is the same effect observed in Figure 42, where given the same length difference between two surfactants, only the smaller ones (short, 3, and medium, 6 beads) formed stripes, whereas the longer ones (medium, 6, and long, 9 beads) did not.

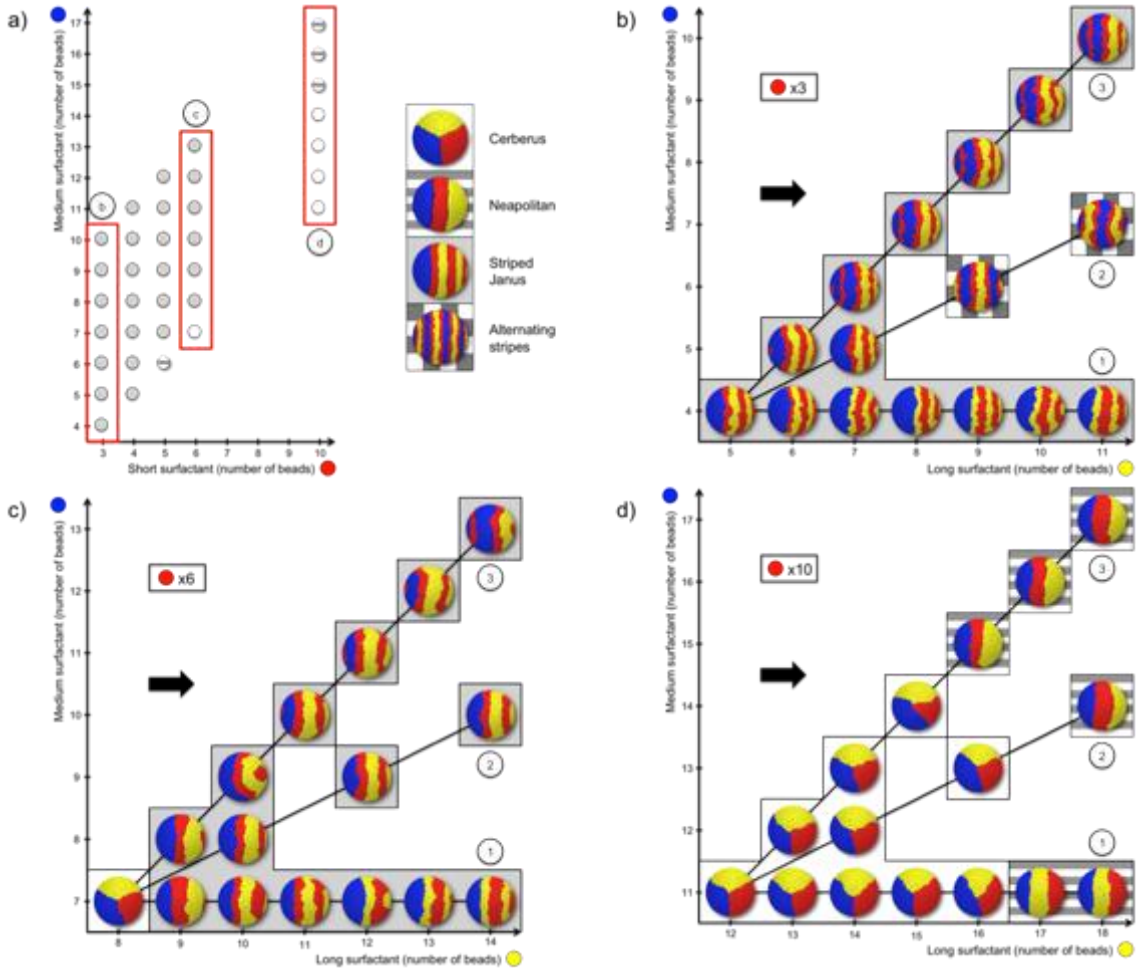

Figure 44 Effect of surfactant length on ternary SAMs. a) Length of short surfactant vs. length on medium surfactant. Dots represent data points simulated for different surfactant lengths and the patterns obtained are presented according to the coloring of Figure 1. b) through d) Length of medium surfactants vs. length of long surfactant. b) through d) are side views of planes highlighted by red squares in a), after adding a third axis representing the length of the long surfactant. NPs have

radius 4. Stoichiometry of SAM is 1:1:1. Interbead repulsion is 15. Length of the short surfactant is b) 3, c) 6, and d) 10 beads. Length of medium and long surfactants are varied along the axis in the figures. The black arrows represent the side from which the figures are viewed in a). In b) through d), line 1 corresponds to the case with two short surfactants and one long, with only a one bead difference between the short and medium surfactant. Line 2 represents the case when the difference in number of beads between the short and medium surfactant is equal to the difference in number of beads between the medium and the long. Line 3 represents the case when there are two long surfactants in the system, with the difference between the medium and the long being only one bead. Tails not shown.

Figure 44b through c show planes perpendicular to the one shown in Figure 44a, corresponding to the red rectangles. In them, the patterns obtained as a function of length of the medium and long surfactants are shown, keeping the length of the short surfactant constant in each case. Three different cases were studied for each plane, corresponding to the numbered lines in the figures.

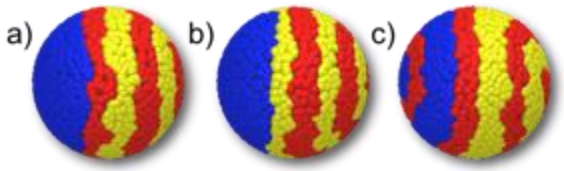

Figure 45 Striped Janus particles. a) Short (red) and long (yellow) surfactants form stripes, while medium (blue) separates. No interface between medium and long. b) Same as a), but with interface between medium and long surfactants. c) Short surfactant forms stripes on both sides of Janus particle. Tails not shown.

The first case, Line 1, is parallel to the long surfactant axis. The length of the medium surfactant is kept constant at just one bead longer than the short surfactant, as the length of the long surfactant is increased to up to eight beads longer than the short one. The net effect of this case is a SAM formed by two short surfactants and a long one. For short surfactants (Figure 44b) a one bead difference is still enough to stabilize the formation of stripes. But as the length of the surfactants increases (c and d), Cerberus particles are formed. In this last case, for a NP of radius 4, surfactants of 10, 11, and 12 beads act essentially as same length surfactants and they separate to minimize the interface between them. Moving from left to right

along Line 1, Striped Janus particles begin to appear as the long surfactant grows. However, unlike the cases previously studied (Figure 45a), this time an interface between the long and medium surfactant is generated, without the need for the short one in between them (Figure 45b). This occurs as the medium surfactant becomes short enough with respect to the long one to offer enough gain in the free volume to justify the formation of stripes.

The second case, Line 2, corresponds to the same length difference between the short and medium, and the medium and long surfactants. Alternating Stripes are formed when the surfactants are short relative to the NP radius (b), but as they grow in length this pattern is lost, turning into Striped Janus (c) and finally Neapolitan particles (d).

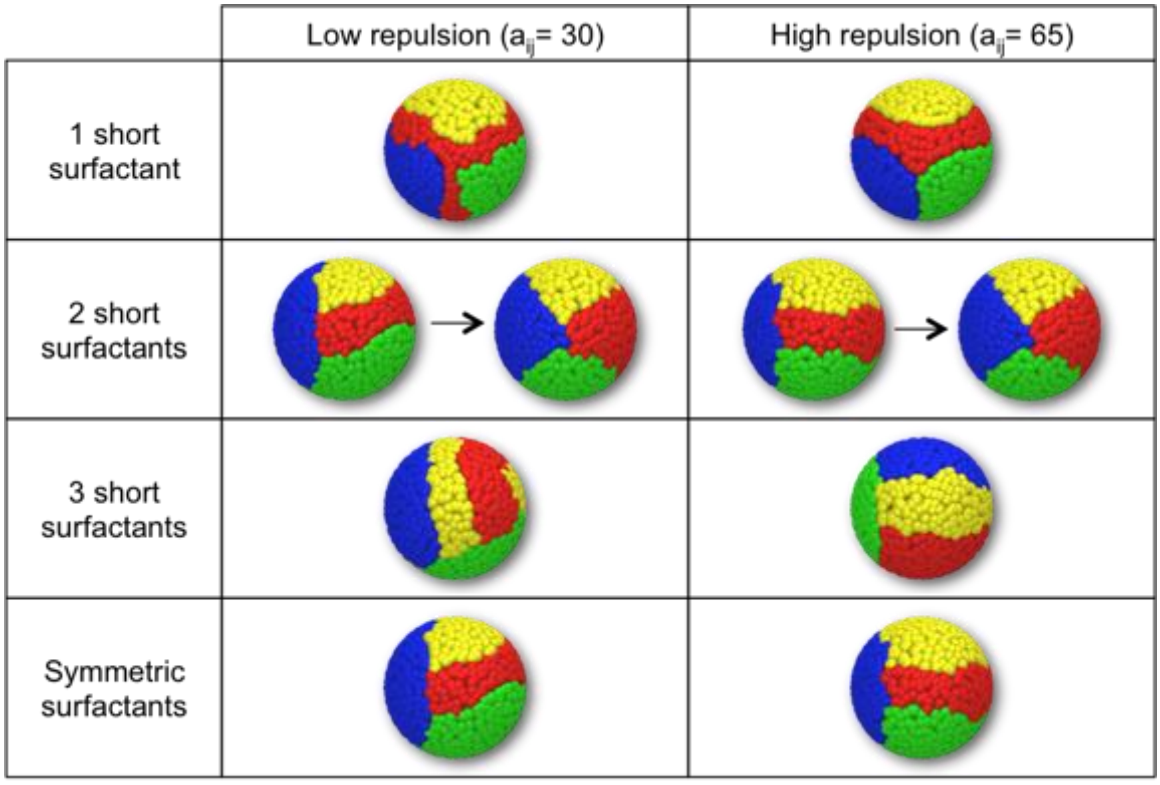

Figure 46 Effect of surfactant length on quaternary SAMs. Tails not shown. Red: short, blue: medium, green: long, and yellow: longest surfactant.

The last case, Line 3, shows the case when the length difference between the long and medium surfactant is only one bead, essentially acting as two long surfactants and one short. A behavior very similar to the one of Line 1 is observed. However, in this case the short surfactant always needs to be in between the other two. Also, the Janus particle has now stripes on both sides, instead of only one (Figure 45). Since the length difference between the long and medium is only one bead, the entropic gains from forming stripes with either one of them are very similar so stripes form on both sides. Once again, this effect is lost as the surfactants become too long with respect to the NP radius, with the number of stripes decreasing in (c), and a Neapolitan particle in (d).

An equivalent study to the one presented in Figure 44 was conducted for quaternary surfactants. However, because the phase space becomes even larger for quaternary surfactants and impossible to represent in two dimensions, the results are summarized as shown in Figure 46. Four different cases were considered for the quaternary surfactants: one short (*i.e.* 3, 10, 11 and 12 beads), two short (*i.e.* 3, 4, 11 and 12 beads), three short (*i.e.* 3, 4, 5 and 12 beads), and symmetric length differences (*i.e.* 3, 6, 9 and 12 beads) between surfactants. The results for each case are shown in Figure 46 for low and high immiscibility. On the case of the two short surfactants in which two patterns are shown for both low and high immiscibility, the transition from the leftmost (decorated Cerberus) to the rightmost (Brahma particle) occurs as the overall length of the surfactants increases with respect to the NP radius.

5.3. Effect of self-assembled monolayer stoichiometry

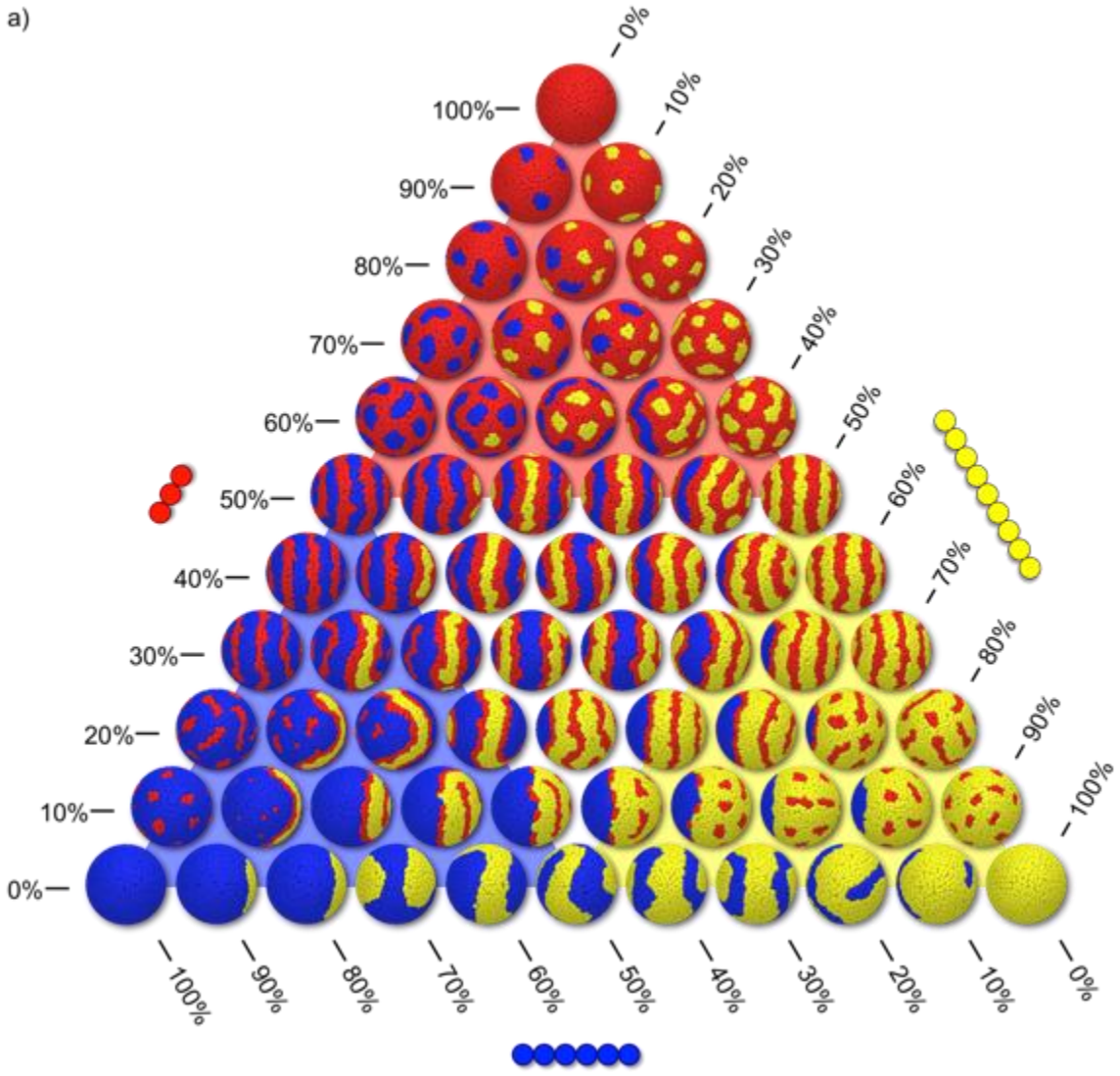

Figure 47 Effect of SAM stoichiometry on ternary MPMNPs. Only head beads shown. NPs have radius 4, and length of surfactants is 3, 6, and 9 beads. Interbead repulsion is a) 30 and b) 65. Color shadows in background represent the surfactant in highest concentration in SAM. Tails not shown.

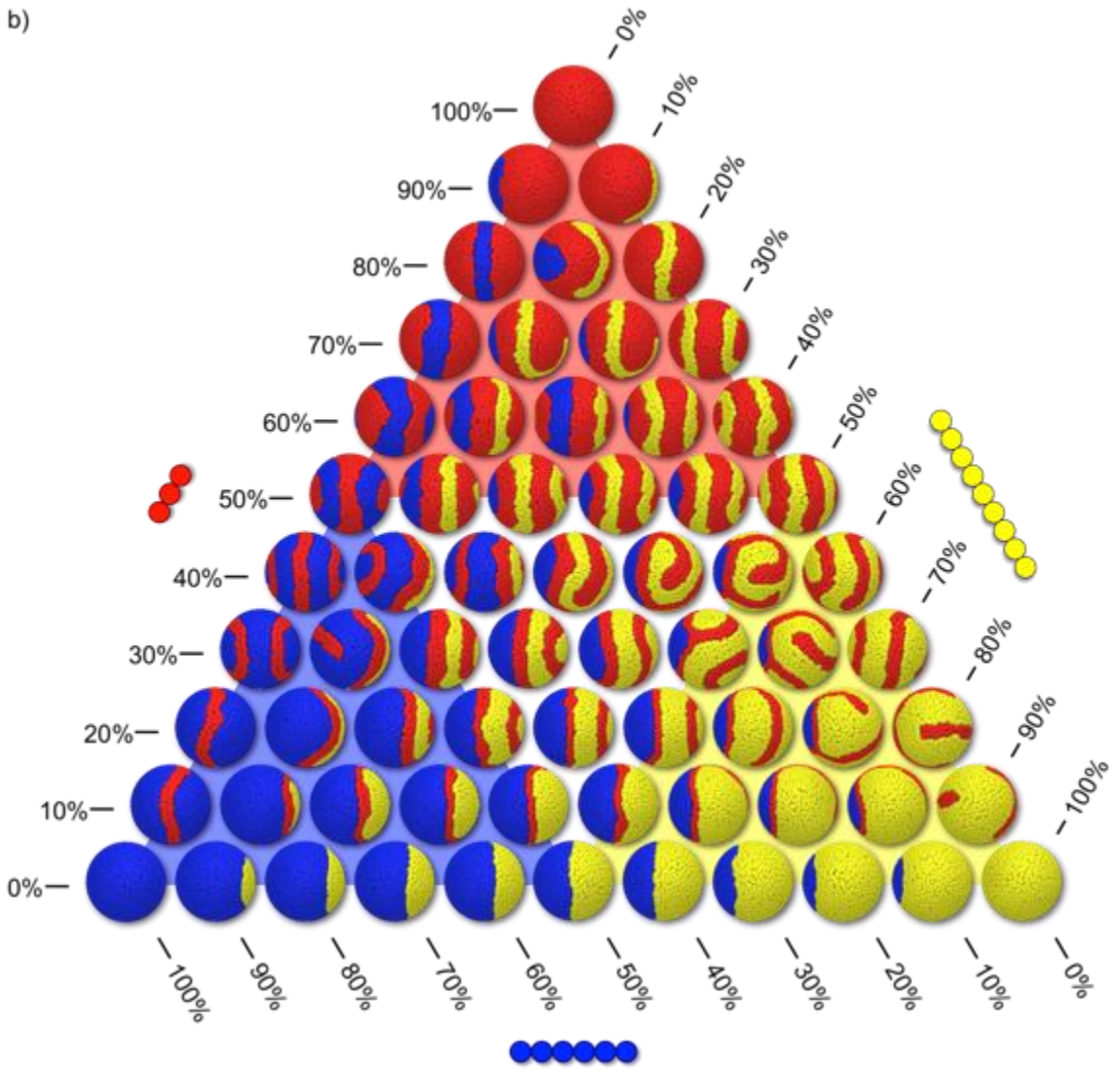

Figure 48 Effect of SAM stoichiometry on ternary MPMNPs. Only head beads shown. NPs have radius 4, and length of surfactants is 3, 6, and 9 beads. Interbead repulsion is a) 30 and b) 65. Color shadows in background represent the surfactant in highest concentration in SAM. Tails not shown.

For fixed NP radius = 4 and length of surfactants (3, 6, and 9 beads), the effect of SAM stoichiometry on ternary MPMNPs is presented in Figure 48. For interbead repulsion = 30 (Figure 48a), the Alternating Stripes pattern is observed around the 1:1:1 critical composition of the SAM. When the concentration of one surfactant is >70%, the patterns present 2D-micelles instead of stripes (Figure 49). When either the medium or long surfactants are in the highest concentration, a Janus particle is

formed with 2D-micelles of the short surfactant dispersed into the surfactant that is present in the highest concentration (Figure 49b and b). When the short surfactant is in the highest proportion, then the other two form 2D-micelles dispersed in a continuous matrix of the short surfactant (Figure 49a). In this case, the entropic gains achieved by the creation of additional interfaces with the short surfactant are enough to stabilize this pattern. For the cases when there are only two surfactants present in the SAM, stripes are formed also for stoichiometries where the relative concentration of the surfactants is similar. If one of them is in excess, 2D-micelles will be formed except for the case where there is no small surfactant present. In this case, Janus particles are formed, and even for near 1:1 stoichiometries the stripes formed are much thicker than the ones formed in all other cases. This is due to the effects of surfactant length as previously discussed.

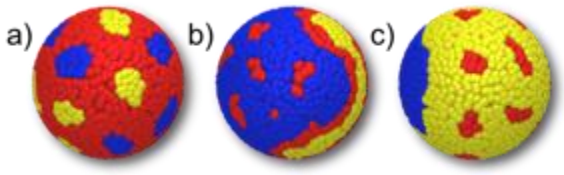

Figure 49 Patterns of 2D-micelles, obtained for concentrations >70% of a) short, b) medium, and c) long surfactant. Tails not shown.

For higher interbead repulsion (Figure 48b), the Striped Janus pattern is always observed. For very low concentrations of the small surfactant (10%) a Neapolitan particle is formed with a very thin stripe of the small surfactant separating the other two. When there is no small surfactant present, the other two form a Janus particle with no stripes. In this case, the relative length of the two surfactants with respect to the NP radius becomes too high, and no stripes are formed.

For quaternary SAMs, the stoichiometric variations of the monolayer are now represented as a pyramid, instead of a triangle. The results are shown in Figure 50 for low and Figure 51 for higher interbead repulsion between unlike surfactants.

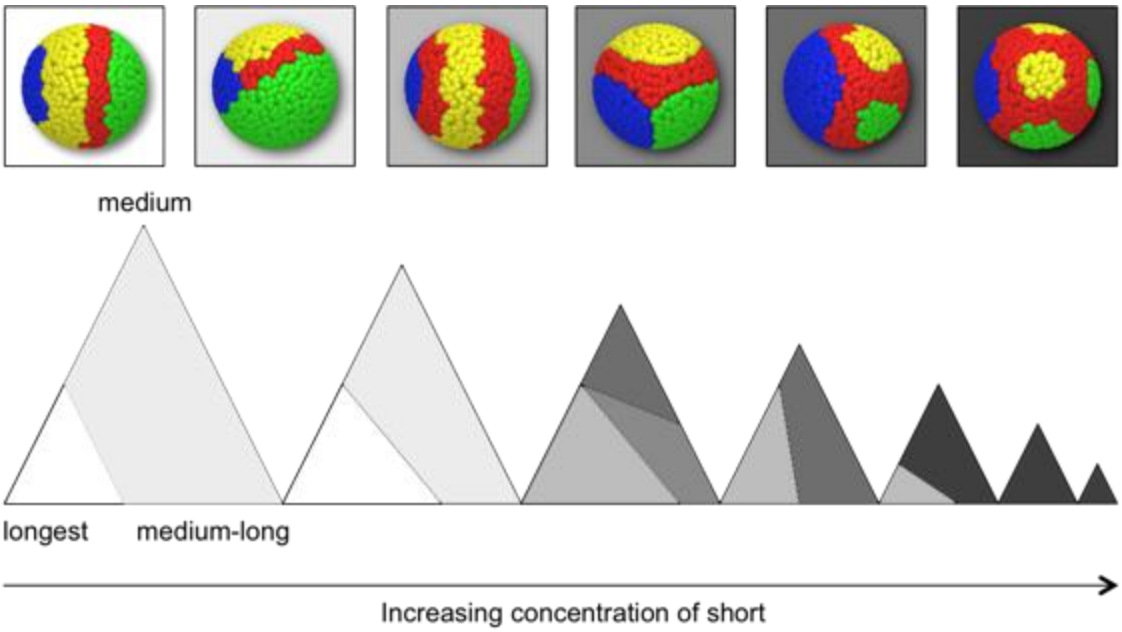

Figure 50 Effect of SAM stoichiometry on the quaternary patterns as shown via ternary phase diagrams for fixed but increasing concentration of short (red) surfactants, in the limit of weak immiscibility between unlike surfactants (a_{ij} = 30). Concentration of short surfactant is varied from 10% on the leftmost triangle to 70% on the rightmost triangle. Tails not shown. Red: short, blue: medium, green: long, and yellow: longest surfactant.

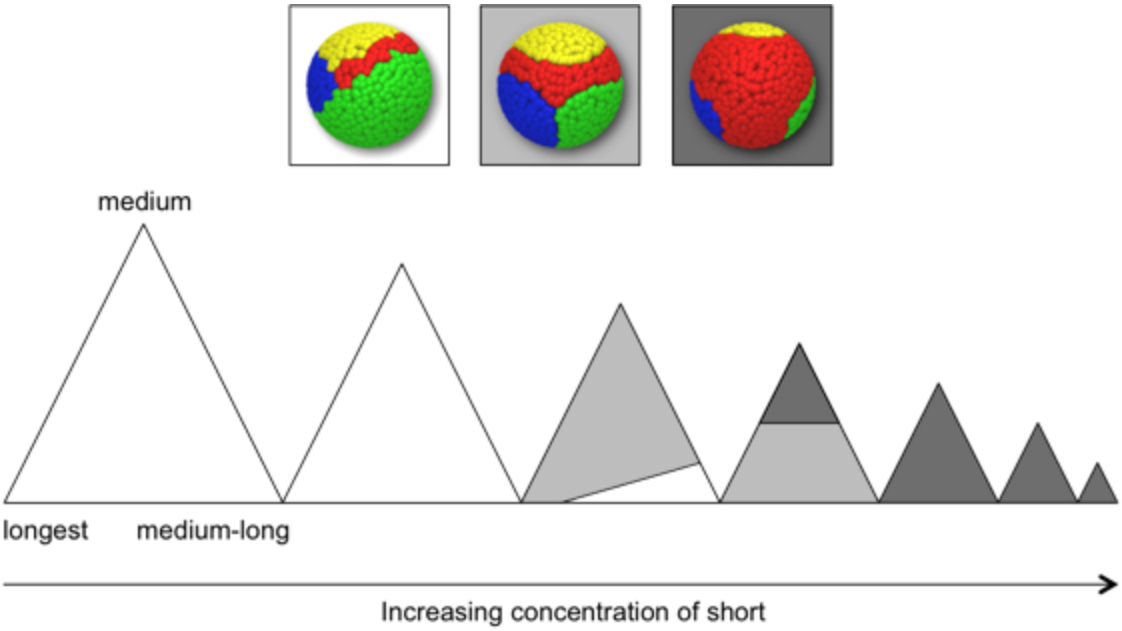

Figure 51 Effect of SAM stoichiometry on quaternary patterns as shown via ternary phase diagrams for fixed but increasing concentration of short (red) surfactants, in

the limit of strong immiscibility between unlike surfactants (a_{ij} = 65). Concentration of short surfactant is varied from 10% on leftmost triangle to 70% on the rightmost triangle. Tails not shown. Red: short, blue: medium, green: long, and yellow: longest surfactant.

5.4. Summary of design rules

We can summarize our findings as general design rules for patchy particles made from quaternary (four-component) SAM MPMNPs:

- Patchy particles with tetrahedral symmetry can be obtained by using the smallest NP radius possible, or by increasing the overall size of the four surfactants with respect to the NP radius, so as to optimize for "bulk" phase separation in lieu of microphase separation.
- Brahma NPs can be produced by using two long and two short surfactants so that there is no interface between the two longest surfactants and the two short ones assemble between them.
- The decorated Cerberus patterns can be obtained by various combinations of surfactant length and immiscibility between unlike surfactants, playing off phase separation and microphase separation unequally between different surfactant pairs:
    - Cerberus particles analogous to those predicted for ternary MPMNPs[61] but with simple decorations between the three main domains of the NP can be obtained when there is one short surfactant and three longer ones;
    - Modified Cerberus particles in which three surfactants form three parallel stripes, and the fourth forms one perpendicular stripe on a pole of the NP can be obtained for symmetric length differences between surfactants when the overall length of the four surfactants is long with respect to the NP radius; or for three short surfactants when the unlike surfactants are strongly immiscible;

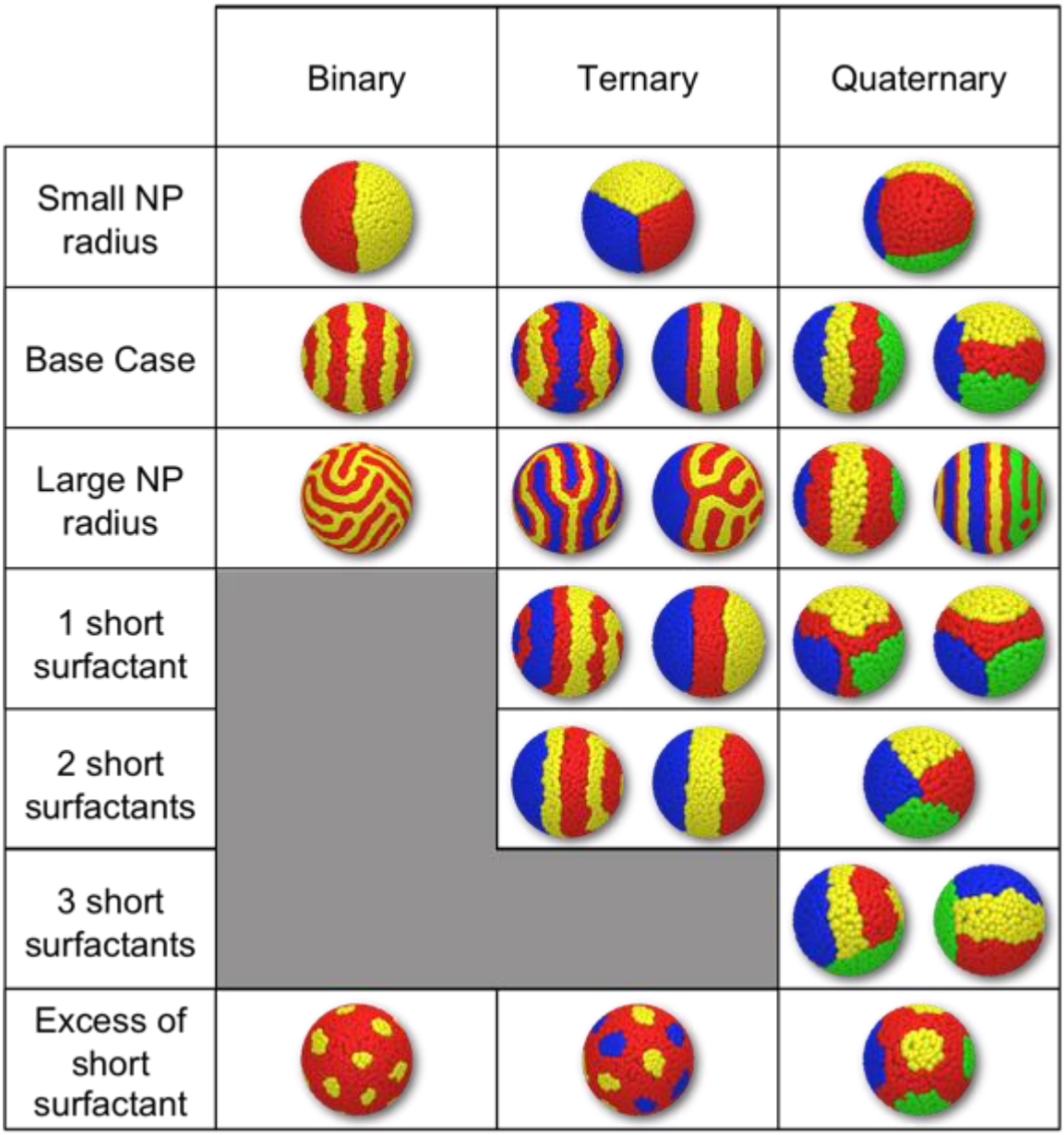

Figure 52 Summary of design rules and patterns for MPMNPs. Tails not shown. Red: short, blue: medium, green: long, and yellow: longest surfactant. Particles not drawn to scale. The base case has a 1:1:1:1 stoichiometry, with symmetric length diference between surfactants (3, 6, 9 beads for ternary; 3, 6, 9, and 12 beads for quaternary) on a NP of radius 4. In the cases when there are two images per case (*e.g.* Ternary base case) the leftmost image corresponds to weak immiscibility between unlike surfactants (a_{ij} = 30) and the rightmost corresponds to strong immiscibility between unlike surfactants (a_{ij} = 65). Shadowed in gray are cases that do not apply, based on the number of surfactants available.

    - A Cerberus particle in which there are stripes in one of the three domains can be made using three short and one long surfactant, with weak immiscibility between unlike surfactants.
- Striped particles can be achieved for weak immiscbility between unlike surfactants, and can be further complicated by increasing the NP radius, going from a simple system of four stripes all the way to a decorated Janus NP with stripes on both sides of the NP.
- Modifying the stoichiometric composition of the SAM allows one to tune the coverage of each surfactant on the surface of the NP for some of the previous patterns, except for the cases when the small surfactant is in excess of 50%, which produces a spotted pattern of 2D micelles.

These design rules are summarized in Figure 52 for binary, ternary and quaternary SAMs. Examples of the application and usefulness of these design rules follows.

5.5. Application of design rules in the formation of new patterns and the study of monolayers formed by mixtures of five or more surfactants

Imagine that we would like to produce a decorated Cerberus NP with stripes on the three sides of the Cerberus. This pattern did not emerge naturally from the combinations of parameters for quaternary SAMs that were studied in this Chapter. However, we now from ternary SAMs that a Janus NP with stripes on both sides can be obtained when there are two long surfactants competing to form interfaces with the short one. Therefore, we can assume that we need three long surfactants (of very similar length difference), and one short one. This makes sense because when we look of this case in Figure 46 for low interbead repulsion, we see that the pattern

form is the closest one to our desired pattern, we only need to add the additional stripes in each side of the Cerberus particle. We can also assume that since the short surfactant will be creating stripes with the other three, we need it to be in a higher stoichiometric ratio, probably close to 3:1:1:1. Based on these heuristics, we simulated the desired system and the result is presented in Figure 53.

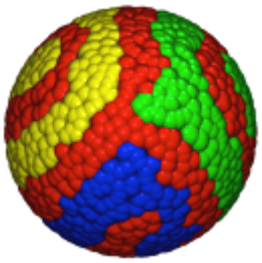

Figure 53 Decorated Cerberus NP with stripes on the three sides. Short surfactant shown in red; longest surfactants shown in blue, green and yellow. Tails not shown.

An analogous reasoning can be applied to any other pattern that may be produced as a combination of the design rules presented in this Chapter. This includes the extrapolation of these design rules to nanoparticles coated with mixture of five or more surfactants, which have not been explicitly studied so far. However, just as adding a third surfactant allowed for the formation of decorated Janus patterns, and the addition of a fourth surfactant allowed the formation of decorated Cerberus patterns, increasing the number of surfactants to five, for example, allows the formation of decorated tetrahedral patterns as shown in Figure 54a. The top image in Figure 54a shows all five surfactants, and the two images directly below it show side views that allow to identify the pattern easier (since in Figure 54a it's difficult to spot all five surfactants, only small regions of the yellow, blue and purple patches are showing).

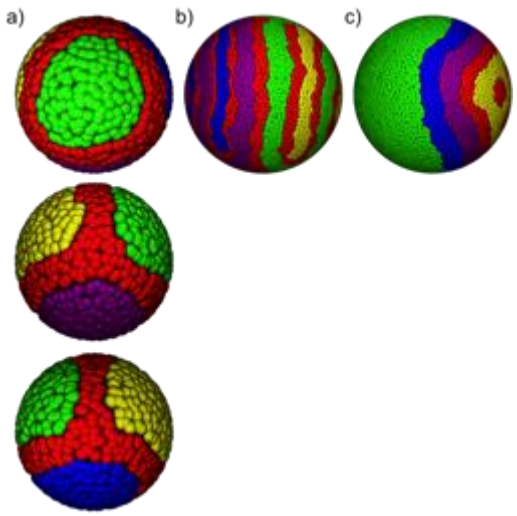

Figure 54 Decorated quaternary patterns formed using monolayers of five surfactants. a) Decorate tetrahedral pattern, images below the top row show different views from the same pattern. b) Janus particle with alternating stripes on both sides. c) Five striped particle. Surfactant colors (from shortest to longest): red, blue, green, purple, and yellow. Tails not shown.

Figure 54b shows a particle with two types of alternating stripes separated on two hemispheres of the NP, similar to a decorated Janus particle. On the right side, the second shortest (blue, 6 beads) and second longest (purple, 12 beads) surfactants for alternating stripes while remaining separated from each other by the short (red, 3 beads) surfactant. On the other side of the Janus, the medium (green, 9 beads) and longest (yellow, 15 beads) surfactants also form alternating stripes. This distribution of the surfactants was to be expected, since in both cases the length differences are maximized (6 to 12 beads on the right, and 9 to 15 beads on the left). To achieve this pattern, a higher concentration of the short surfactant is necessary (3:1:1:1:1).

Finally, Figure 54c shows a pattern in which most surfactants form stripes, while the yellow and longest maximize interface on one hemisphere of the NP by forming small 2d-micelles of the shortest (red) surfactant inside a continuous matrix of the longest (yellow). The other surfactants arrange themselves in a way that the second longest surfactant (purple) shares an interface with the two shortest (red and blue).

As shown in Figure 54, understanding the effect of adding additional surfactants to the system (ternary and quaternary monolayers) allows predicting the behavior of monolayers with multiple surfactants (five or more) without the need to perform exhaustive phase-space studies. Since each time an additional surfactant is added to the system the possible combination of parameters increases exponentially, it is no longer practical to study larger systems extensively. It is more efficient to utilize the knowledge garnered from ternary and quaternary monolayers to identify the range of parameters that more closely resemble the desired pattern, and then study in detail a much more constrained phase-space until the desired pattern is perfected.

Chapter 6. Crystallization of surfactants of self-assembled monolayers

Janus nano- and micro-particles are currently under intense investigations because of their unique assembly and physico-chemical properties, as well as many potential applications. Unfortunately, mostly at the nanoscale, there are only complex procedures intrinsically limited to low yields to produce Janus nanoparticles. Obviously this limits their potential. Monodisperse Janus NPs based on mixed self-assembled monolayers were synthesized by the Stellacci group using a one-step one-phase method. The results were confirmed by scanning tunneling microscopy, transmission electron microscopy, nuclear magnetic resonance and molecular dynamics simulations. By tuning the length difference and composition ratio of binary mixtures of suitable ligand molecules of different lengths, the surface morphology of the resultant NP is varied in a controlled manner. The ease and efficiency of this method to synthesize small Janus nanoparticles (< 10 nm) as well as its scalability and versatility to include various functionalities make it a powerful candidate to become the main approach to achieve Janus nanoparticles.

6.1. Introduction

Janus particles can have different shapes, including dumbbell-like,[64] acorn-like,[65] half raspberry-like[66] or snowman-like particles[67] and be produced with different materials such as dendritic macromolecules,[68] block-copolymers micelles,[69] or inorganic materials.[70] The asymmetry of Janus particles makes them useful for a

wide range of applications. They can be used like surfactants and stabilize oil-in-water or water-in-oil emulsions via the Pickering effect.[71] The emulsions stabilized by Janus particles have been shown to be more stable than those stabilized by homogenous particles due to the higher absorption energy[72,73] making them suitable for applications ranging from water-based paints to heterogeneous nanocatalysis.[74] Janus particles can also be used in electronic displays,[75] nanomotors,[76,77] drug or gene delivery[78] or as building blocks for more complex suprastructures such as supracrystals or molecular colloids.[1,79,80]

Various strategies have been used to produce Janus particles. These include approaches such as toposelective surface modification (or masking), template-directed self-assembly, controlled phase separation or controlled surface nucleation.[81-83] However, methods to obtain small (<10 nm) nanoparticles (NPs) are scarce. The majority of the methods for micron-sized or hundreds of nanometer-sized Janus particles are excellent in terms of morphology control and yield, but they have not been shown to scale to small (10 nm and smaller) NPs.[83-89] The few available methods to obtain small Janus NPs normally involve complex procedures involving multiple-step synthesis. Most methods cannot be considered truly bulk syntheses and hence have a limited yield because they use surfaces as masks.[81] To the best of our knowledge none has the ability to produce large quantities of Janus NPs in the way a direct synthesis could and it is evident that methods able to synthesize small Janus nanoparticles in an easy way and with high yield are a necessity nowadays.

In 2004, Jackson, et al. discovered that 1-2 nm “ripples” or “stripes” formed on the surface of gold NPs when these NPs were coated with SAMs of binary mixtures of immiscible ligands.[8,48] This finding was striking because similar ligand molecules were known to form domains on flat surfaces somewhat larger than the NPs (>5nm) themselves.[90] Later, simulations (coarse grained as well as MD) demonstrated that the stripes result from a balance between an entropy-driven stabilization of the domain interface due to the gains in conformational entropy for longer ligands

surrounded by shorter ones, and enthalpy of phase-separation driven minimization of those interfaces.[10] The Gibbs free energy of mixing $\Delta G^{mix}=\Delta H^{mix}-T\Delta S^{mix}$ is composed of an enthalpy part responsible for the phase separation of the two ligands, and an entropy term ($-T\Delta S^{mix}$) that is negative as the entropy increases upon the mixing. The entropy in this case can be separated into two parts, configurational entropy due to the distribution of ligands on the surface of the metallic core and conformational entropy due to the allowed conformations of individual ligands. In the case of self-assembled monolayers (SAMs) -and in general for any two-dimensional assembly, the latter term is directly proportional to the length of the interface, and hence can be further decomposed in an entropic term per unit length and a length term. Theoretical approaches, and further simulations have confirmed this interpretation at least in the case of similar monolayers on cylinders.[91,92] When the total entropy balances the enthalpy, patchy NPs are produced (around the 1:1 composition these form striped-like domains). Simulations based on this reasoning have correctly predicted many experimental observations,[10,60,93] and have predicted other morphologies that have yet to be found.[61,62] Most notable of these are Janus morphologies, which were predicted to form on NPs of sufficiently small radius of curvature to allow for each ligand to explore a large enough cone angle such that the number of microstates accessible to the ligand far exceeded the free volume obtainable by the ligand when surrounded by shorter ligands. In this case the contribution of the interfacial conformational entropy to the free energy of mixing becomes negligible, and the enthalpic term dominates, leading to "traditional" demixing and the formation of Janus NPs. This prediction has been confirmed recently for NPs with diameters well below 3 nm.[94-96] However, these NPs difficult to synthesize in monodisperse samples, have limited stability, and in any case exist only in a very limited size range.

The Stellacci group presented a novel route to produce monodisperse small Janus NPs (<10 nm) by direct one-step synthesis based on the aforementioned thermodynamic principles. Their approach strategically increases the enthalpic gain for phase-separation while simultaneously minimizing the conformational free-

energy gain at interphases, thus leading to a morphology that tends to minimize interface length. This can be achieved using combinations of relatively long and short ligands so that (i) the strong tendency to crystallization for the long ligands increases the enthalpy driving force towards separation, and (ii) the large length mismatch between the two ligands leads to a 'hanging' part of the long ligand that in itself has a strong tendency to crystallize. The latter argument implies that for the 'extra length' of the longer ligands the enthalpy of crystallization should exceed the interfacial conformational entropy (in absolute numbers). Together both arguments suggest a plausible strategy for the formation of Janus NPs. Two thiolate molecules were used initially, 1-dodecanthiol (C12) and 1-hexanethiol (C6). The length difference of six methylene groups is equivalent to a hexanethiol molecule (known to produce ordered domains on flat and curved surfaces[97]). As shown in Figure 55, NPs produced with a C12:C6 ratio of 2:1 (reaction stoichiometry) exhibit Janus morphology as observed by scanning tunneling microscopy (STM). This case was analyzed in detail through a systematic study with a variety of different ligand ratios and lengths. The Stellacci group further demonstrated the synthesis of Janus NPs with functional groups, extending their potential for a variety of applications.

Figure 55a shows an STM image in an ultra high vacuum (UHV) Omicron system of NPs synthesized using a modification of the method described by Zheng et al.[98] (a one-step, one-phase synthesis) and covered by a monolayer of C12:C6 2:1 (reaction stoichiometry). Each circular mushroom-like motif corresponds to an individual NP with an average size of 10.4±1.0 nm. The distribution of NP sizes determined through analysis of the STM images is presented in Figure 55e. This size is consistent with TEM results (see Supporting Materials, SM) that show an inter-particle distance of 10.8±0.4 nm and a core size of 8.2±0.5 nm. These NPs tend to form a close-packed lattice, which is characteristic of monodisperse NPs. Most interestingly, a pronounced sub-NP feature is observed: each NP (in the specific image, most in generic images) is split into two parts, as illustrated by the cartoon in Figure 55c. This feature is further confirmed by STM results using a Veeco Multimode in air on the same sample, as shown in Figure 55b and d; these images

also show a clear patchy structure with C12 and C6 split into separated domains. The statistics on the surface-area ratio between the small patch (red section) and the whole NP based on both UHV and air STM results yield a value of 0.39±0.06 (Figure 55f), which is only a little higher than the stoichiometry ratio of 2:1 (note though that the final ratio of C6:C12 tends to be smaller than the initial stoichiometry ratio of the reaction). As STM can only visualize the exposed surface, the higher measured ligand ratio could be due to the nanoparticles orientation exposing more of the C6 surface.

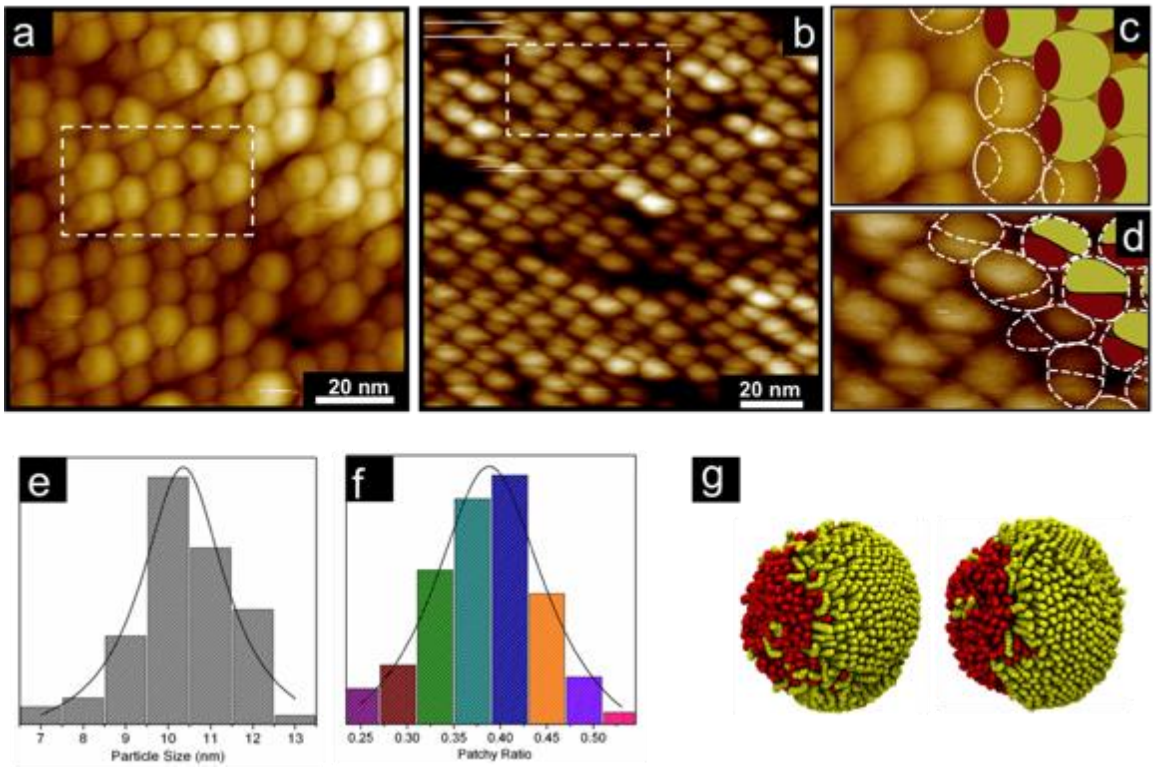

Figure 55 a) A STM image of a Langmuir-Blodgett film of C12:C6 2:1 Janus NPs collected in UHV with an Omicron STM microscope and b) in air with a Veeco multimode both on the same sample. c) and d) are close views of a) and b) respectively, where the superimposed cartoon represents the surface morphology of the Janus NP with long C12 ligand section in yellow and short C6 ligand part in red. e) The size distribution of the Janus NPs. f) A statistical diagram of the ratio of the C6 size to the whole NP based on STM results. g) The front and backside of a C12:C6 2:1 NP obtained by MD simulation; red ligands correspond to C6 and yellow to C12.

We performed MD simulations for C12:C6 NPs at the same stoichiometry starting from a mixed ligand configuration. Figure 55g shows both sides of the simulated NP demonstrating phase-separation of the ligands into two large domains. Closer inspection shows how the long ligands tend to align in a parallel fashion, *i.e.* in a crystalline state while the short ones tend to be in a less order conformation, in agreement with what is known for self-assembled monolayers on flat[97] and curved surfaces.[24] This observation further supports the hypothesis leading to the choice of this pair of ligands. It can also be noticed that the ligands at the interface appear significantly less crystalline than those further away from the interface. This type of interfacial configuration of the ligands would result in a darker interface in STM images. Indeed we find a dark interface with a sizeable thickness in good agreement with the MD simulations Figure 55c and d.

Interestingly, Janus NPs were not observed when the C12:C6 2:1 NPs were synthesized using one-phase synthesis with the reduction of $HAuCl_4$ with $NaBH_4$ in ethanol at 0°C. These NPs have only slightly smaller sizes but higher polydispersity (4.2±1.3nm) than the NPs produced using the Zheng method, suggesting an influence of the synthesis method on the final structure. This is not unexpected because different temperatures of synthesis and to a lesser extent different solvents, can lead to different equilibrium states, as recent studies suggest.[99]

This approach to Janus NP synthesis has the potential for broad impact when one considers the large variety of existing functional ligands or ligands that could be further functionalized. Here, as an example, we have synthesized NPs composed of 1-dodecanthiol (C12) and Hex-5-yn-1-thiol (C6yne). C6yne is formed by a 6-carbons chain with a triple bond at the end of the chain. This acetylene group can be used to attach one side of the NP to another system or to another NP with a direct reaction. C12:C6yne 2:1 also exhibits Janus morphology, as can be seen in the STM image (Figure 56a). Similar to the case of C12:C6 2:1, mushroom-like motifs with two different sides are observed, with the larger hemisphere corresponding to C12 and the smaller to C6y. The acetylene group has been used to bind the NPs using a direct

coupling catalyzed by CuBr. Because these groups are concentrated on one side of the NP, small clusters of NPs such as dimers are expected but not large aggregates. Figure 56b shows a TEM image of the nanoparticles after the binding showing the presence of many dimers and a few trimers. An analysis of the images show that around 75% of the clusters correspond to dimers, ~15% to trimers and fewer than 10% to clusters of higher number, indicating the segregation of the acetylene groups to only one side of the NPs.

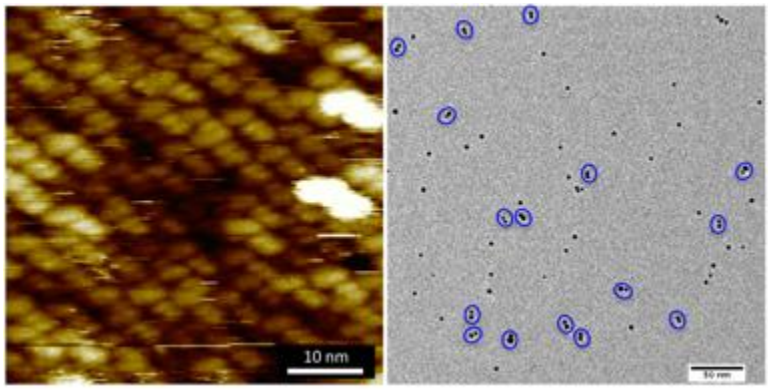

Figure 56 a) STM image of C12:C6yne 2:1 NPs. b) TEM image of C12:C6y 2:1 after direct coupling. Blue circles show where the dimers have been identified.

6.2. Effect of self-assembled monolayer stoichiometry

To gain a better understanding of the separation phenomenon a series of C12:C6 NPs with different ligand ratios were synthesized. The actual ratio of ligands on the NPs was been obtained by H NMR spectroscopy on the ligands after etching. The measured ratio showed a larger fraction of the longer ligand than the stoichiometric ratio used in the reaction. The observed fraction of Janus NPs relative to particles that have no discernable structure in STM images changes with the ratio of the ligands. Based on visual analysis of several STM images the samples were classified as: primarily Janus NPs (Full), roughly half Janus NPs (Half) and a small percentage

of Janus NPs (Few). Examples of these NPs can be seen in the Figure 57a, b and c respectively (the images for the NPs at all the different ligand ratios can be found in SM). Figure 57d shows the amount of Janus as a function of the molar fraction of C6 (χ(C6)).

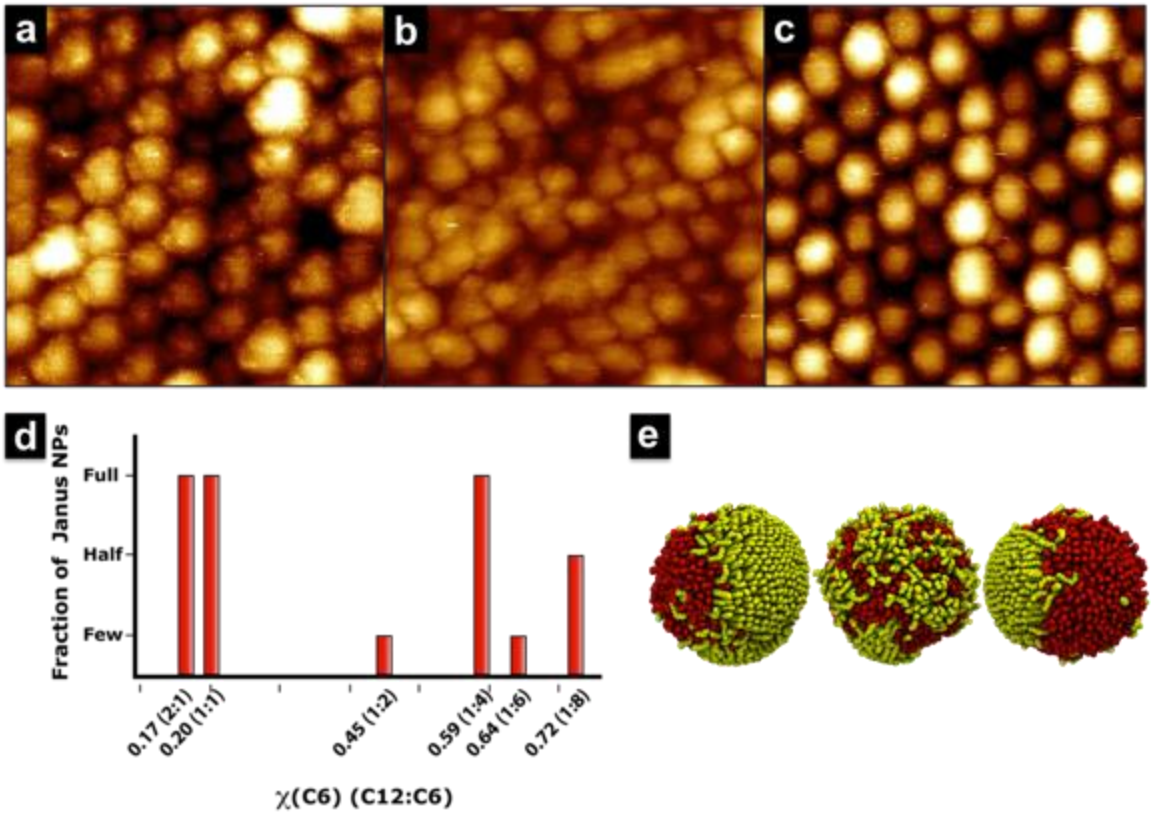

Figure 57 a)-c) STM images of C12:C6 NPs at different ligand ratios showing different yields of Janus nanoparticles. The duplicated images outlining the NPs have been added to easily identify the Janus Nanoprticles. a) STM image of NPs with χ(C6)=0.59 showing a high yield of Janus NPs. b) STM image corresponding to the NPs (χ(C6)=0.72) where roughly half of them are Janus. c) STM image corresponding to the NPs (χ (C6)=0.64) where only a few Janus can be found (STM image for other compositions can be found in the SM). d) Amount of Janus NPs visualized for the different NPs ratios classified in "full", "half" or "few" depending on the amount of NPs visualized; The x-axis indicates de molar fraction of the C6 ligand (χ (C6)) and in brackets the ligand ratio used for the reaction. e) MD simulations of C12:C6 at different ratios of 2:1, 1:1, 1:2 (C12 ligands in yellow and C6 ligands in red).

The decrease in the percentage of Janus NPs at intermediate values of χ(C6) can be explained by an increase in the interfacial entropy. As discussed, conformational

entropy increases linearly with the length of the interface. Hence as the 1:1 ratio is approached, it is reasonable to expect that this term becomes comparable to the enthalpy, leading to an instability of the Janus morphology, and consequent increase in the amount of interface. Simulations at this composition support this reasoning, showing fluctuating patterns similar to those of a system close to some critical instability. Figure 57e shows the equilibrium states from MD simulations of C12:C6 nanoparticles at compositions 2:1, 1:1 and 1:2. As observed for the ratios 2:1 and 1:2, there is a complete phase separation of ligands into Janus morphology while for the 1:1 composition we observe a higher degree of mixing with the formation of small irregular domains. The lack of any observable structure in STM images of χ(C6)~0.5 (despite considerable efforts) further supports this interpretation. On the other hand decrease of the yield of Janus NPs at much higher values of χ(C6) could be somewhat easier to explain if one accepts the simulations results of less ordered short ligands, then as the χ(C6) increases there will be a larger tendency for C6 to act as a 'solvent' for C12. When analyzing the plot in Figure 57d it is important to consider two additional factors that can also affect the results. First some of the NPs could adopt a vertical orientation (the interfacial line parallel to the surface) rendering the feature delineating the two phases invisible in STM images. Second a possible segregation of NPs could occur similar to the known segregation that takes place for NPs of different sizes[100] so in the hypothetical case of a mixture of NPs with different surface structure it could happen that only areas of one kind are observed.

Additional investigations for the 1:1 stoichiometry were performed, both through simulations and experiments. Since we were not able to observe the formation of Janus particles for a length difference of six carbons, we decided to increase that length difference and verify its effect on the crystallization of the ligands. Therefore, we studied the 1:1 stoichiometry for a NP coated with the following surfactant mixtures: C12:C5, C13:C6, and C15:C6. In all cases, we increased the length difference to more than six carbons. As shown in Figure 58, we obtained the desired Janus pattern for all three cases. These results confirm the idea that there is a competition between length of the interface and length difference between the

surfactants that influences the type of pattern on the monolayer. For longer interface length, a longer length difference between the surfactants is required to stabilize the Janus pattern.

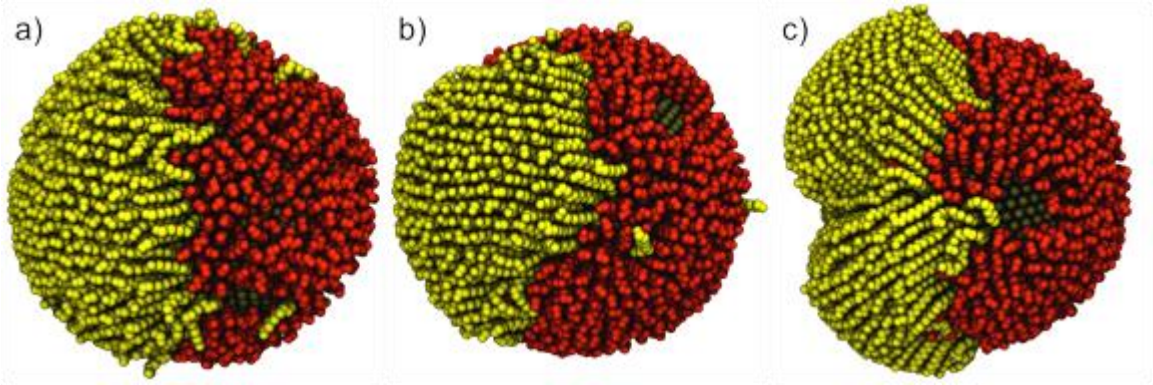

Figure 58 Results from MD simulations of a NP coated with a monolayer of a) C12:C5, b) C13:C6, c) C15:C6 with a stoichiometric ratio of 1:1.

As seen on Figure 58c, the longest surfactant (C15) separates into well-defined clusters that have different tilt angles. This result was expected, and previously observed for homoligand monolayers.[24] We will further explore the effect of the length of the surfactants in the next section.

6.3. Effect of length difference between surfactants

As mentioned above, the phase separation of the ligand mixture occurs due to the length mismatch between the two ligands. This begs the question of what is the necessary length mismatch to produce Janus NPs. To answer this question, a systematic investigation of NP patterning by varying the length mismatch of the alkanethiols from eight to two methylene groups was performed both experimentally by the Stellacci group and by me through MD simulations. Figure

59a-d shows the STM images of NPs covered by different mixed alkanethiols with the general composition C12:C*n* 2:1 with *n*=10,8,6 and 4, resulting in four length mismatches of 2, 4, 6, and 8 methylene groups, respectively. The results show separation of ligands in Janus NPs for the C12:C4 and C12:C6 NPs containing 6 and 8 methylene groups difference in length, respectively. Non-Janus NPs are observed for the C12:C10 combination (2 methylenes length difference). MD simulations of NPs with a C12:C10 monolayer for different stoichiometric ratios also show that for this system phase separation in Janus does not occur at any of the ratios tested, showing a good agreement with the experimental results (Figure 59e). For C12:C8 NPs non-Janus configurations were observed with only a small percent of Janus NPs (less than 2%). Other NPs with short length difference and shorter ligands (C8:C6 and C8:C4) also showed non-Janus morphology. The results show that a 6-carbon length mismatch is the minimum necessary to produce a complete formation of Janus NPs (for an all-alkane system). These results are also in good agreement, despite the difference in curvature, with what has been found for mixed SAMs of alkanethiols on flat surfaces.[101] From a thermodynamic point of view the reduction of the length mismatch corresponds to a decrease of the enthalpy ΔH^{mix}, as this is mainly the energy involved in the crystallization of the extra length of the long ligand, and a decrease of the conformational entropy of mixing as the number of microstates of the extra length is smaller for shorter chains. For the limit $\Delta L \rightarrow 0$ both terms will be 0 as the molecules are identical. On the other hand the conformational entropy of mixing remains independent on the length mismatch as it takes into account only the position of the ligands on the surface of the gold core. This means that the free energy has a term that tends to 0 and a term that remains negative so it necessarily has to became negative producing a complete mixture of the ligands bellow a certain value of ΔL. On the contrary if we start from a small value of ΔL where the ligands are mixed and we increase it, the enthalpic part per methylene group should be bigger than the configurational entropy per methylene so it reaches a moment where ΔG^{mix} is positive giving rise to Janus nanoparticles.

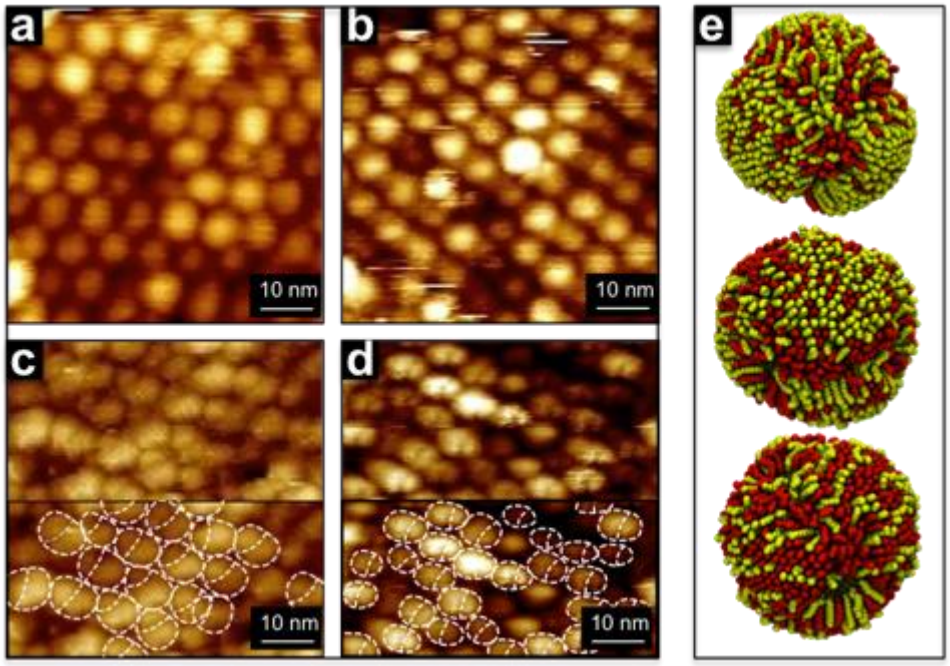

Figure 59 STM images of Langmuir-Blodgett films of mixed ligand NPs. a) C12:C10 2:1. b) C12:C8 2:1. c) C12:C6 2:1. d) C12:C4 2:1. The duplicated images with the superimposed cartoons have been added to help to identify Janus NPs. e) MD simulations of C12:C10 at different ratios of 2:1, 1:1, 1:2 (C12 ligands in yellow and C10 ligands in red)

6.4. Effect of repulsion between surfactants

The Stellacci group also synthesized particles coated with a mixture of alkane thiols (C14 or C12 specifically) and 6-Mercapto-1-hexanol (C6ol) or 4-Mercapto-1-butanol (C4ol), to produce hydrophobic/hydrophilic Janus NPs, as most of the theoretical predictions on unusual pickings focus on these types of particles. Figure 60a and b show the STM image of C14:C6ol 1:1 and C12:C4ol 1:1 respectively. Both NPs have a length mismatch approximately equivalent to a seven-methylene groups chain and show Janus morphology. This long mismatch, as well as the very well known tendency for C12 and C14 to form highly crystalline monolayers when on Au NPs is a strong driving force for the formation of Janus NPs, as shown in the STM images in

Figure 60. It should be pointed out that when the alkane ligand becomes shorter, then a weaker tendency to crystallize together with a stronger ability for C6ol to disrupt the interface lead to the formation of stripes in these types of particles, as previously shown using both STM and atomic force microscopy.[90] Finally, it should be pointed out that STM images for these NPs show a preferential orientation for the NPs similar to one observed for all-alkane NPs. The reason for this orientation (with the Janus plane roughly perpendicular to the substrate plane) is not clear. Most of the experimental samples were produced via a Langmuir Schaefer approach hence we postulate that this may be due to ideal packing. This will be discussed in greater detail in 0. For these particles another type of packing was observed, much simpler to rationalize. Indeed, preliminary results on the STM images of C14:C6ol 1:1 seem to indicate that there are regions where the nanoparticles are oriented with the hydrophilic part facing up. This configuration is expected as the upper surface of the NP monolayer is the one that was in the contact with water during the monolayer formation on Langmuir trough. Figure 60c shows an example of a C14:C6ol 1:1 NP monolayer in which the hydrophilic parts of the NPs are facing up. Figure 60d shows a profile of one of those NPs in which the different parts can be appreciated.

Figure 60e shows the result form a MD simulation of the same C14-C6ol system. Once more, the formation of a Janus particle through the crystallization of the ligands is demonstrated. In this case, the two driving forces acting in the system favor the macrophase separation of the unlike surfactants. On the one hand, the immiscibility between them drives them to separate. If the surfactants were smaller (like the cases presented in previous chapters), the length difference between the surfactants would make them form stripes to maximize conformational entropy. However, in this case the ligands are long enough that they have crystallized. Therefore, the conformational entropy gains are no longer relevant, and the stripes are no longer an energy minimizing pattern. Both the immiscibility and the crystallization of the ligands favor the formation of a Janus NP.

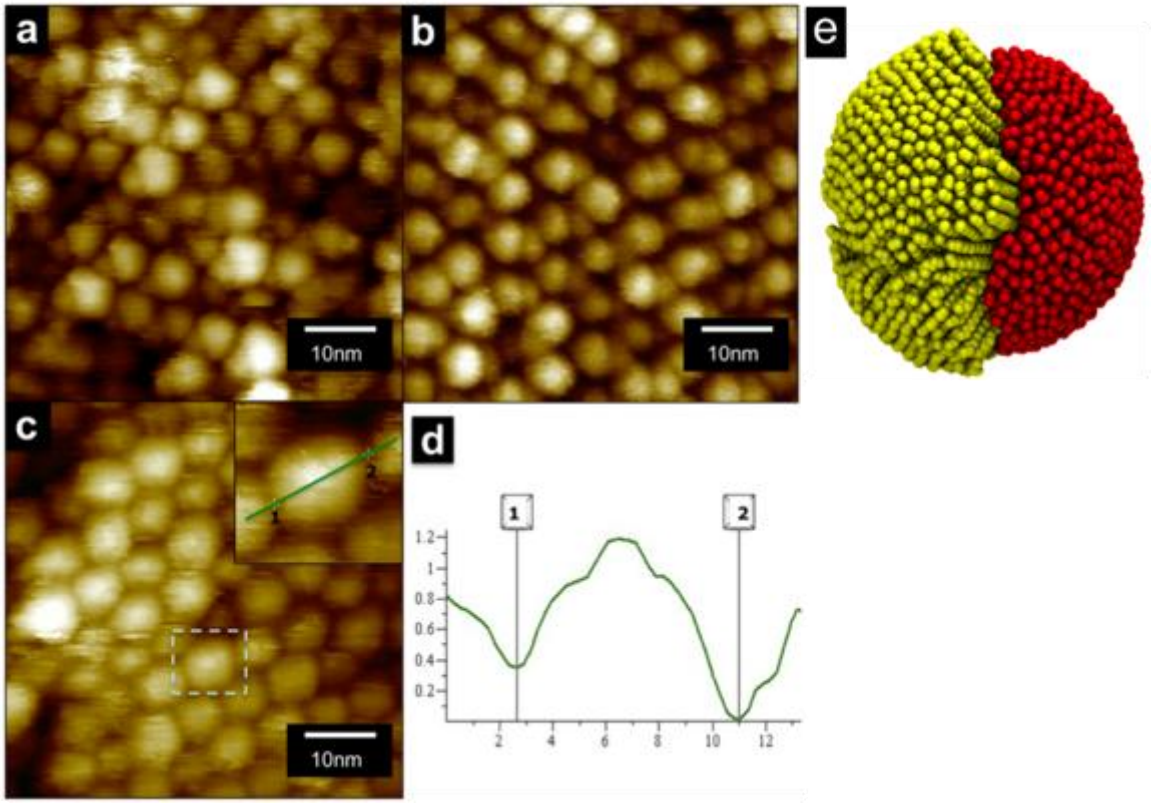

Figure 60. a) STM image of C14:C6ol 1:1 Janus NPs. b) STM image of C12:C4ol 1:1 Janus NPs. c) STM image of C14:C6ol 1:1 Janus NPs with the C6ol path facing up. Inset shows one of this NPs with an inner circle corresponding to the C6ol and an external part corresponding to C14 d) Smoothen profile of the line in the inset of c). Points 1 and 2 correspond to the limit of the nanoparticle and the higher part in the middle corresponds to the C6ol patch. e) MD simulation of a C14:C6ol NP showing the formation of a Janus pattern with crystallized surfactants. Yellow: long, red: short.

6.5. Effect of nanoparticle radius

All previous simulation results shown in this Chapter were done on a spherical nanoparticle with a radius of 38Å. We verified the effect of varying the NP radius and the results are shown in Figure 61. It can be seen than changing the NP radius does not affect the Janus pattern formed on the monolayer, as was expected since the crystallization of the surfactants only depends on the length of the surfactant

(*i.e*, sufficiently long surfactants crystallize on flat surfaces as well[40]). Furthermore, in Figure 61 we show how for small NP radius (28Å in this case), the clusters formed by the ligand tails become even more pronounced that they do for larger NP (48Å). This is again to be expected because of the increase on the radius of curvature of the NP. The NPs with larger radius resemble closest a flat surface, and it is well know that no such clusters are observed in flat surfaces. Indeed, for the limit when the NP radius $\rightarrow \infty$, the tilt angles of the surfactants tend to align all in the same direction, as seen on Figure 61 (left).

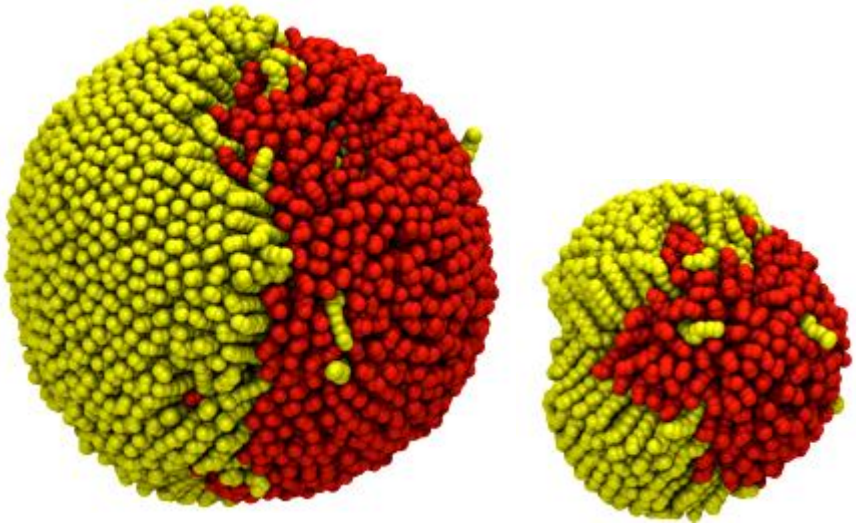

Figure 61 Crystallization of SAMs on NPs of radius 48Å (left) and 28Å (right). C12:C6 1:2. Yellow: long, and red: short surfactant. NPs no shown to scale.

6.6. Summary

Through collaboration with the Stellacci group, we have shown that SAMs of mixed alkanethiols with different length on gold nanoparticles can be used to produce Janus NPs through a novel one-step method with high yield. STM images of NPs at varying composition or ligand length mismatch are in good agreement with MD simulations. In our opinion the phase separation in Janus morphology is likely due to the crystallization of the long ligands overcoming the configurational and

conformational entropy. Finally, Janus nanoparticles with acetylenes as functional groups were synthesized, demonstrating the formation of dimers as additional evidence of the two-sided Janus morphology and as a demonstration of the potential of this method to obtain a high yield of designer Janus NPs with tailored functionality.

Chapter 7. Crystallization of patchy particles

In this Chapter we study the alignment and ordering of multiple patterned NPs assembled into two-dimensional monolayers. This study was inspired by the packing of Janus particles presented in Chapter 6. We first investigate this phenomenon through interaction and shape arguments. Afterwards, we utilize the sticky and repulsive interaction points of the patchy particles presented in Chapter 4 and Chapter 5 to guide the self-assembly of those NPs into ordered structures.

7.1. Alignment of Janus nanoparticles

As shown in Chapter 6, it was observed experimentally that the Janus NPs always arranged in the same manner when assembled into a Langmuir-Blodgett film. The particles showed a closed-packing configuration, and the patches of long surfactants were all pointed in the same direction. The only exception occurred when one the surfactants was terminated with an alcohol group, in which case that side of the Janus NP was always exposed to the water (Figure 60). In this section we investigate the forces that are acting between the Janus NPs that cause them to arrange in this fashion.

1.1.1 Interactions between two NPs

We first simulated just two NPs adjacent to each other. The particles were initialized with their patches pointing in the same direction (Figure 62a left) and opposite directions (Figure 62b left). The particles are treated as rigid bodied, and allowed to move freely in a very small box that forces them to interact with each other in all dimensions. The non-bonded interactions between surfactants were the same used to generate the Janus patterns in Chapter 6. The rightmost images from Figure 62 show the final configurations of the NPs. We observe a tendency of the patches of long (yellow) surfactant to point towards the short (red) surfactant of the other NP. We also note a tendency for the NPs to maximize the contact points between them, *i.e.* instead of minimizing contact points as shown in Figure 62a left, they rotate with respect to each other to increase the shared surface between them as seen in Figure 62a right. We believe this is due in part to the attractive term of the Lennard-Jones potential acting between the alkane chains.

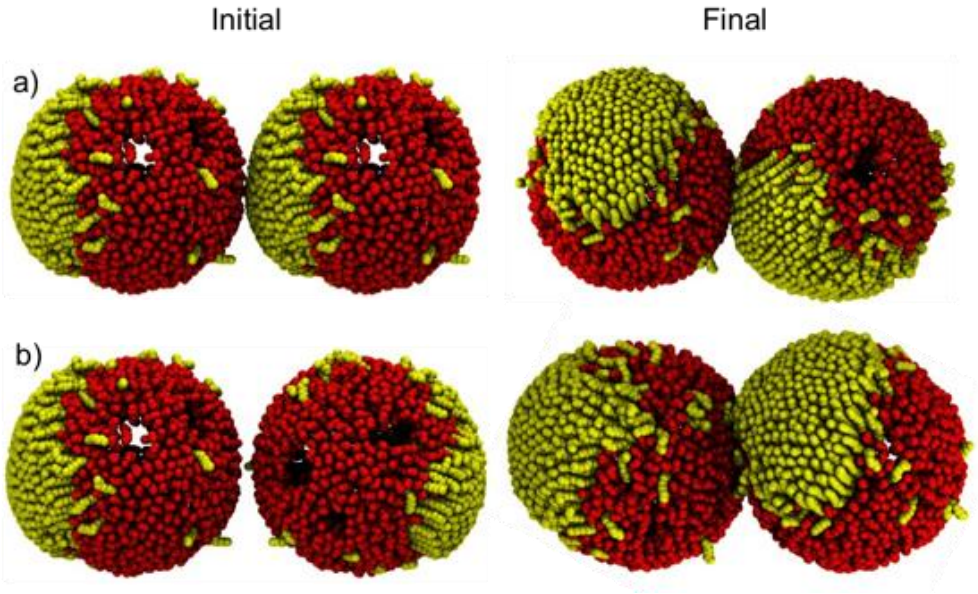

Figure 62 Initial (left) and final (right) configurations for two Janus NPs initialized with the long surfactant (yellow) patches pointing in a) the same and b) opposite directions.

7.1.1. Assembly of multiple NPs

To verify the preliminary results presented in Figure 62, we simulated the self-assembly of 6x6 Janus NPs uniformly distributed in a square box. The Janus patterns were frozen on the NPs using the rigid bodies constrain, and the NPs were trapped between two walls to keep them restrained to a two dimensional interface. The NPs were allowed to move freely inside the quasi-two dimensional box. This system size was chosen because it was the maximum number of NPs allowed by the GPUs memory. Each simulation was run over 15 million time steps, taking about 96 GPU hours to complete. The simulations were initiated from three different initial configurations, shown in Figure 63. Figure 63a and b show two configurations in which the Janus NPs are evenly distributed across the simulation box, not on a close-packed configuration but in a square lattice. In Figure 63b the Janus NPs are distributed in rows pointing in opposite directions, and in Figure 63a the NPs are all pointing in the same direction. To generate the random configuration form Figure 63c, the system was simulated for a long time with only repulsive interactions. After the system had randomized, the attractive interactions were turned back on and Figure 63c was used as an initial configuration for simulations with the full Lennard-Jones potential.

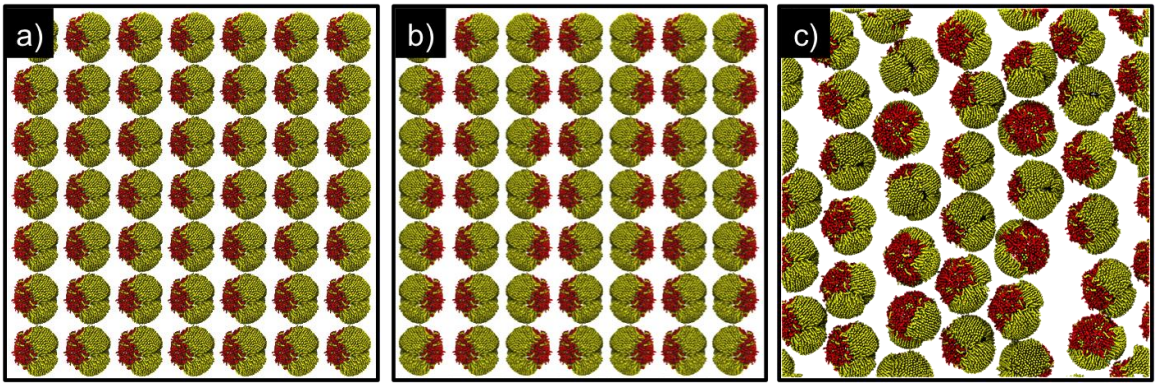

Figure 63 Examples of initial configurations for the Janus NPs with a 2:1 mixture of C12 (yellow) and C6 (red) surfactants.

Figure 64 shows the results for Janus NPs using with the same interaction potentials described in Section 2.2.1 (which were also the same used to obtain the Janus patterns in the previous Chapter). As can be seen in Figure 64, the Janus NPs are attracted to each other and arrange in a close-packed configuration, rather than occupying all the empty space in the box. This indicated that the attractive part of the Lennard-Jones potential plays an important role in the self-assembly of these NPs. Furthermore, we see a similar arrangement to what was observed experimentally (Chapter 6) in which we see a specific preference for the short (red) surfactant to interact with the long (yellow). We postulate that this arrangement maximizes the interaction points between two neighboring NPs.

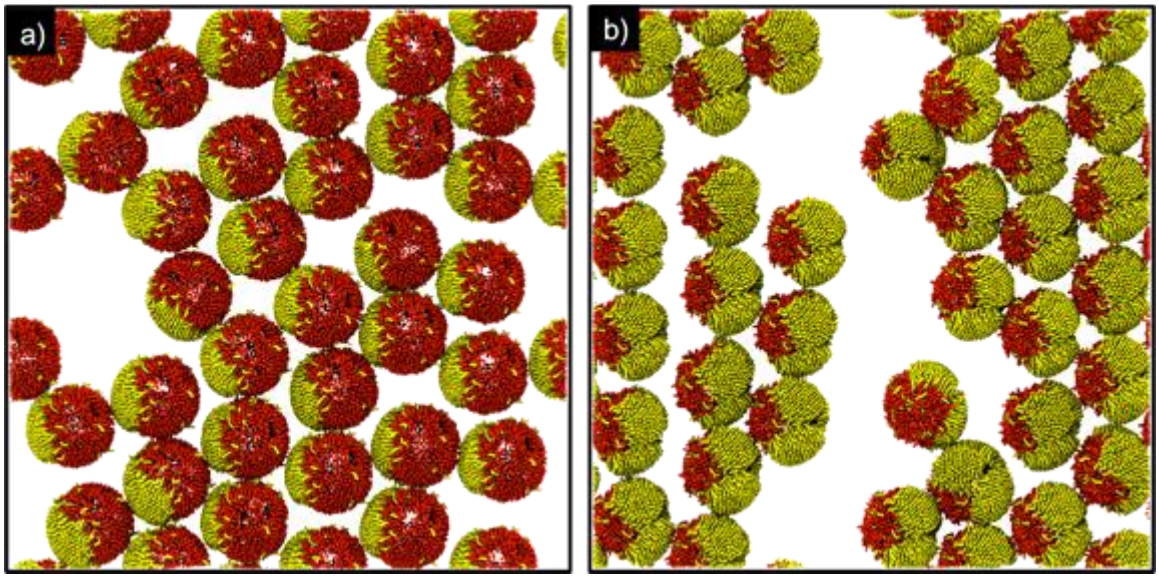

Figure 64 Assembly of 6x6 Janus NPs coated with a)1:2 and b)2:1 mixture of C12 (yellow) and C6 (red) surfactants.

To verify the alignment of the NPs, we calculated the order parameter (S) defined by Equation 31:

$$S = \left\langle \frac{3\cos^2(\theta) - 1}{2} \right\rangle \qquad \textbf{Equation 31}$$

This order parameter is an average of the orientation of the NPs with respect to the preferred orientation of the system. To calculate it, we first found the vector that unites the centers of mass of the C12 and C6 patches of the NPs. For each NP in the system, we found the center of mass of the short and long surfactants, and connected those two points with a line, which we call the orientation vector. We then calculated the angle between the orientation vector for each NP and the mean of all the orientation vectors (*i.e.* the preferred direction of the system). We expect that if all the NPs have the same orientation, that angle should be 0 degrees or very close to 0 degrees, and therefore the order parameter should be very close to 1. For completely disordered systems, the order parameter should be 0. For order liquid crystals, this order parameter is usually expected to fall between 0.3 and 0.8.[102] To study the alignment of the Janus NPs, we study both the distribution of the angles in the system, and the values of the order parameter. The order parameters for all cases presented in this section are summarized in Table 7.

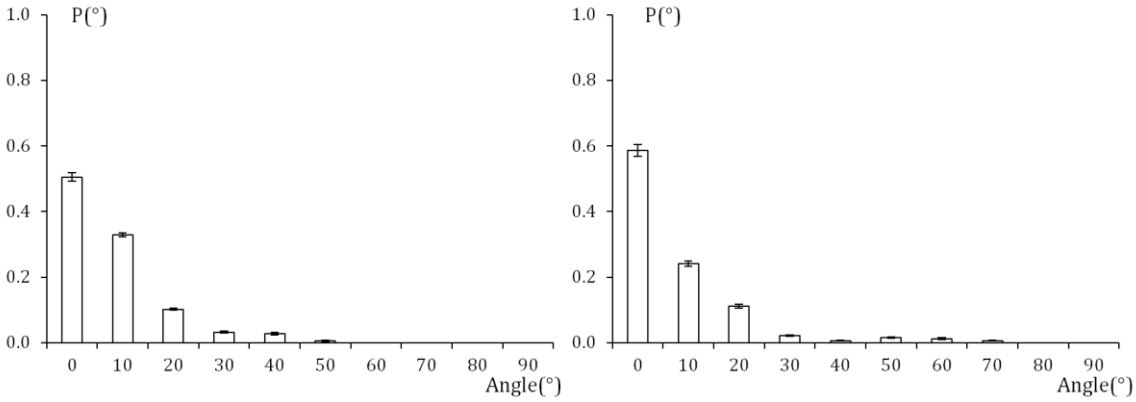

Figure 65 Probability distribution of the angles between the orientation vector of each NP and the preferred direction of 6x6 NPs Janus coated with 1:2 (left) and 2:1 (right) mixture of C12 and C6 surfactants as shown in Figure 64.

In Figure 65 we plot the probability distribution of the angles between the orientation vectors and the preferred direction for the configurations presented in Figure 64. As can be seen in Figure 65, this distribution peaks at a 0 degrees, as is expected for NPs aligned with the preferred direction of the system. The peak is more pronounced for the 2:1 stoichiometry (Figure 65 left), which indicates a better

ordering of the NPs than for the 1:2 case. This indicates that the shape of the NPs may be playing a role in their ordering, since the 2:1 Janus NPs shape is less-spherical than the 1:2 NPs. The distributions shown in Figure 65 were averaged over ten runs for each system.

7.1.1.1. Effect of the interaction potential

To verify the role of the Lennard-Jones potential in the arrangement of the NPs, we conducted two additional studies. In the first one, we diminished the strength of the interaction potential by 50%, *i.e.*, in Equation 14 we used 50% of the value shown in Table 1 for ε. These results are shown in Figure 66a for a 2:1 mixture of surfactants. If we compare Figure 64b and Figure 66a (in which the only difference is the strength of the Lennard-Jones potential) we observe that the NPs present a very similar behavior.

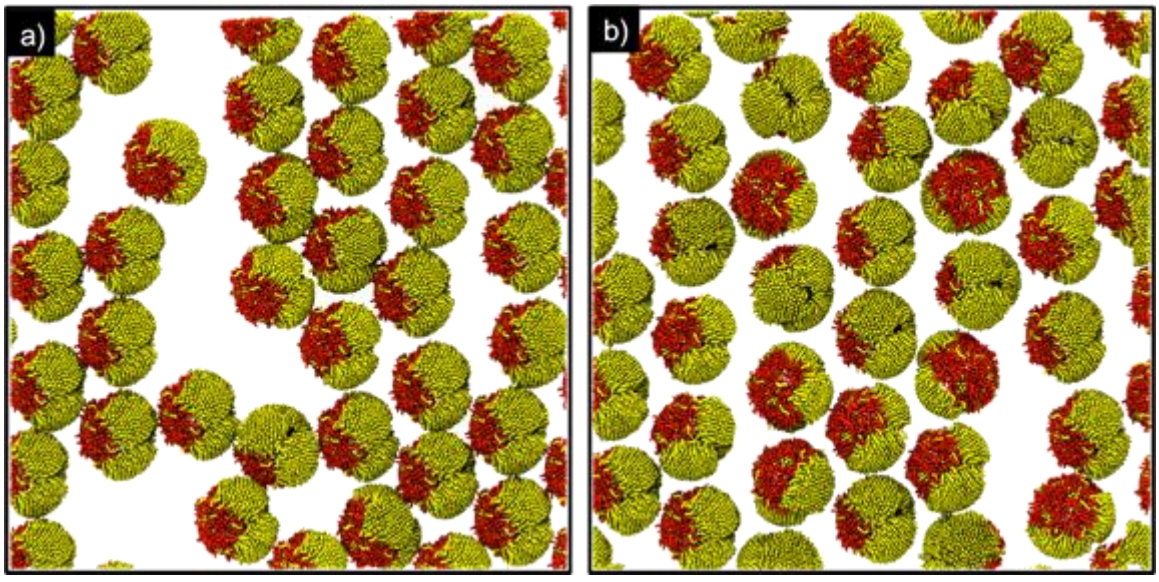

Figure 66 Assembly of 6x6 Janus NPs coated with a 2:1 mixture of C12 (yellow) and C6 (red) surfactants with different interactions: a) Lennard-Jones potential is 50% of the one shown in Figure 64b; and b) Lennard-Jones potential without the attractive well.

The other modification to the potential consisted in using a Lennard-Jones interaction without the attractive well, as shown in Equation 30. The results are

shown in Figure 66b, and it can be seen that in this case the ordering of the NPs is lost. Without the attractive well, the NPs no longer attract each other, so they are uniformly distributed occupying all space (not minimizing the distance between them). We also observe no ordering of the NPs, with no preferential orientation of the short (red) surfactants. This last test confirms the importance of the attractive interactions between the NPs for their alignment into a closed-pack and oriented configuration.

We then again calculated the probability distribution of the angles between the orientation of each NP and the preferred direction of the system for the assemblies presented in Figure 66 to verify the alignment of the NPs. The results are presented in Figure 67. When we compare Figure 65(left) to Figure 67(right) we see that by diminishing the strength of the interactions between the NPs, the general shape of the probability distribution remains the same. However, the peak shown in Figure 67(right) for the reduced potential is not as pronounced as the one seen in Figure 65(left) for the normal inter-particle interactions. This is expected as well, as we postulate that the strength of the potential plays an important role in the ordering of the NPs.

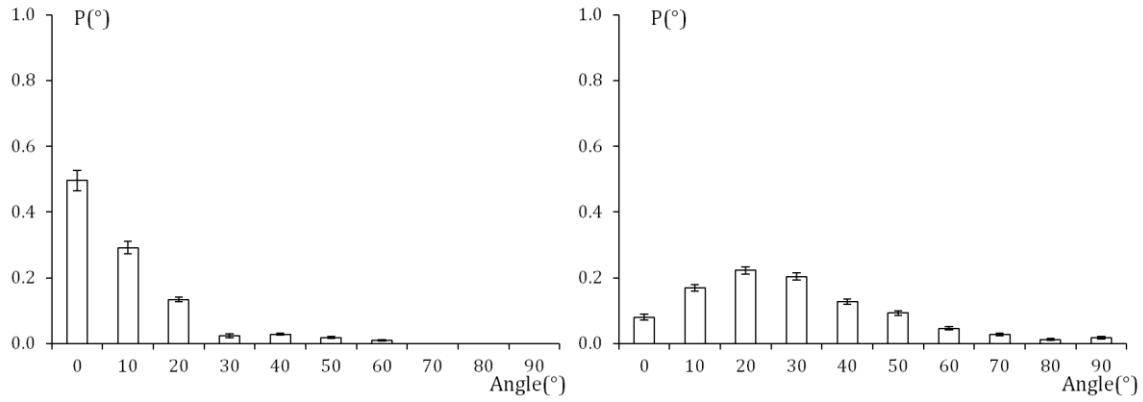

Figure 67 Probability distribution of the angles between the orientation vector of each NP and the preferred direction of the 6x6 NPs Janus coated with a 2:1 mixture of C12 and C6 surfactants with different interactions (as shown in Figure 66): right) Lennard-Jones potential is 50%; and left) Lennard-Jones potential without the attractive well.

As we look at Figure 67(left), in which there are only repulsive interactions between the NPs, it becomes evident that the ordering has been lost. There is no peak at 0 degrees form preferred orientation of the NPs in the box anymore, as can be seen in Figure 66b. This once again confirms the importance of the role played by the interactions between the Janus NPs in guiding their ordering. Figure 67(left) shows no preferred ordering of the NPs, but a fairly regular distribution of angles.

7.1.1.2. Effect of the NP shape

To take the role of shape into consideration we shrank the box starting from a disordered configuration like the one showed in Figure 66b, to force the NPs to come close together and organize. These simulations were performed while maintaining only the repulsive part of the Lennard-Jones potential, so that no attractive interactions were acting between the NPs, and in the NPT ensemble. Figure 68 summarizes the results from these simulations, showing that the NPs begin to align once more and become oriented as the spacing between is reduced and they are forced to organize in a close packed configuration, which will allow them to pack better and fill space (Figure 68a).

Figure 68b shows the probability distribution of the angles between the NPs orientation and the preferred direction of the system shown in Figure 68a. We see an improvement in the ordering of the NPs from the configuration shown in Figure 66b, however the peak in the structure factor is still not as clear as it was when the full attractive and repulsive interactions were considered in Figure 64b.

The comparison between all these cases is summarized in Figure 69 for both stoichiometries (1:2 and 2:1). It can be seen than in both cases, when there are only repulsive interactions between the NPs there is no preferred orientation for the system. In all other three cases (full Lennard-Jones interaction, 50% Lennard-Jones interactions, and repulsive interactions while shrinking the box) the probability distribution follows a very similar pattern, confirming that all three possibilities produce a similar ordering of the NPs.

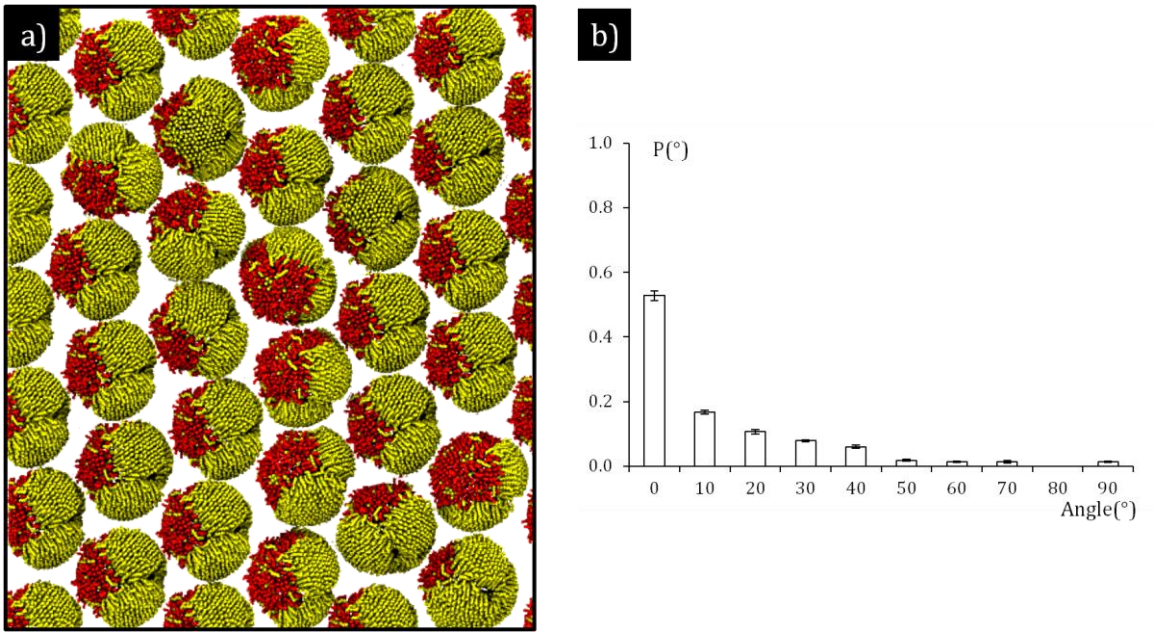

Figure 68 a) Assembly of 6x6 Janus NPs coated with a 2:1 mixture of C12 (yellow) and C6 (red) surfactant with only repulsive interactions between the beads, and b) probability distribution of angles between the orientation of each NP in (a) and the preferred direction of the system.

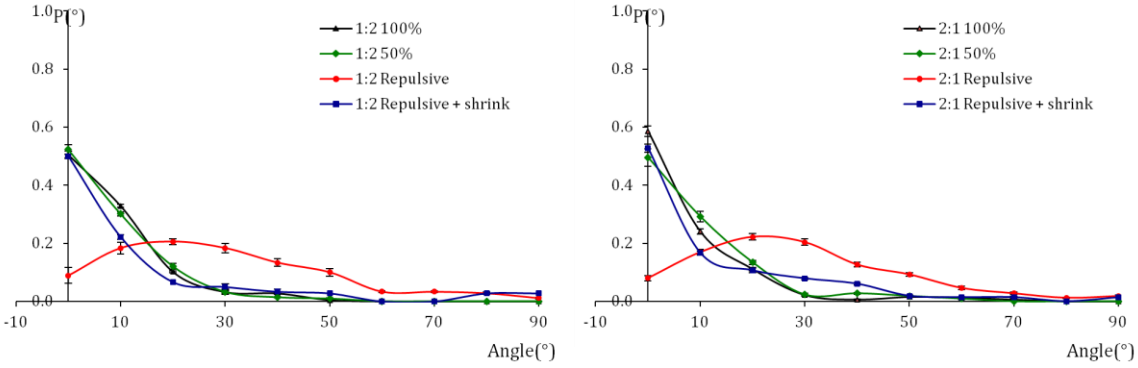

Figure 69 Comparison of the probability distribution of the angle between the NP orientation vector and the preferred vector for the systems discussed in this section and summarized in Table 7 for a system of 6x6 NPs Janus coated with 1:2 (left) and 2:1 (right) mixture of C12 and C6 surfactants and different interactions between the NPs.

Finally, in Table 7 we present the order parameter calculated for all the systems studied in Section 7.1.1. The values of the order parameter demonstrate once more the results presented in Figure 69. They show good alignment of the NPs when there

are attractive interactions in the system, and for system with only repulsive interactions and a small box that force the NPs to order because of shape effects. The alignment of the NPs is lost when there are only repulsive interactions but the box is not shrunk.

Table 7 Order Parameters for the Assembly of Janus NPs on two-dimensional interfaces

Stoichiometry (C12:C6)	Interactions Between the NPs	Order Parameter S (± 0.1)
1:2	Lennard-Jones	0.8
	50% Lennard-Jones	0.9
	Only repulsive	0.4
	Only repulsive, shrinking the box	0.8
2:1	Lennard-Jones	0.9
	50% Lennard-Jones	0.8
	Only repulsive	0.3
	Only repulsive, shrinking the box	0.8

7.2. Two dimensional assembly of patchy nanoparticles

Inspired by the previous results of assembly of multiple Janus NPs into ordered structures, we performed simulations to study the assembly of other types of patchy NPs, with the intention of exploiting the repulsive and attractive patches resulting from immiscible tail end groups to guide the self-assembly of the NPs. Like before, the striped pattern was maintained by using rigid bodies. The tails were not

considered in these simulations because the surfactants are very short (less than 12 carbons) and therefore not expected to crystallize. The number of NPs simulated was again limited by the available GPU memories. The simulations were run for over 30 million time steps each, taking about 50 GPU hours to complete. The results are presented in Figure 70.

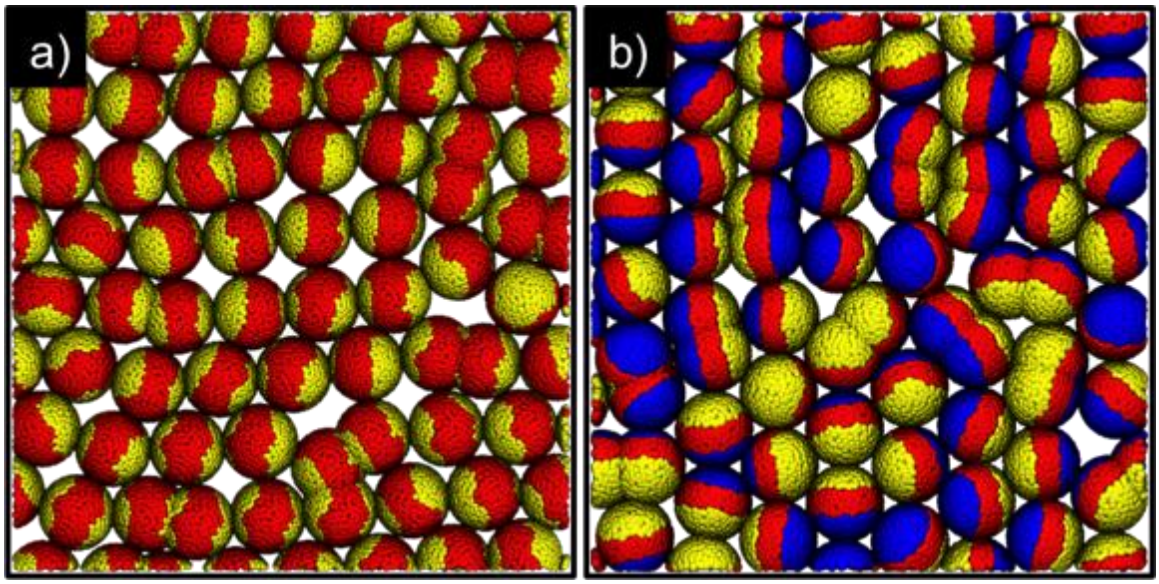

Figure 70 Assembly of 8x8 a) binary and b) ternary striped NPs constrained to a two-dimensional interface. Tails not shown. Red: short, blue: medium, and yellow: longest surfactant.

Figure 70a shows the assembly of binary NPs with a single stripe in the middle of the NP. This pattern is produced by relatively short surfactant with high interbead repulsion between unlike surfactants (as shown in Figure 48). The NPs arrange in a closed-packed configuration, with some NPs overlapping with other because of the soft-repulsion between DPD beads. In general, we see good alignment of the NPs. In Figure 70b we see a similar behavior for ternary Neapolitan particles. However, we observe many more grains in the system, with the NPs organizing with the stripes perpendicular to each other (Figure 71a and b) and aligned perpendicular to the plane of the wall, or with the stripes aligned parallel to the plane of the wall. This last configuration can be seen in Figure 71c for a larger system (10x10 NPs), and occurs when only one surfactant (in this case the medium, blue) can be seen from

the angle the image was rendered. Figure 71c is not an equilibrated simulation and is only included here to show the possible arrangement of the NPs.

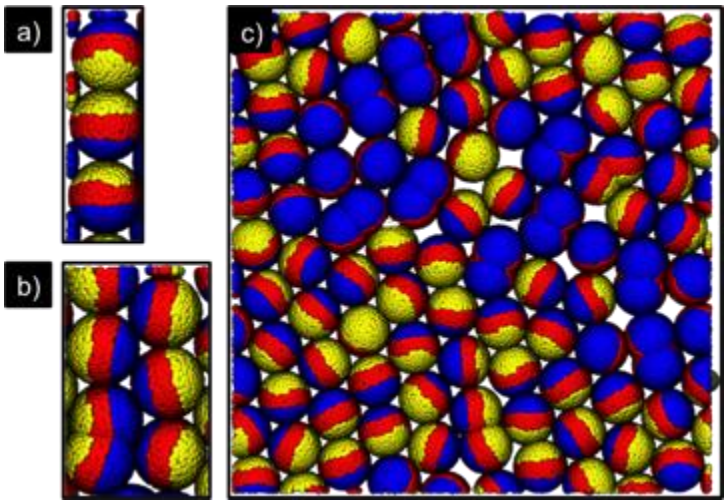

Figure 71 Possible orientations observed in the assembly of Neapolitan particles. Tails not shown. Red: short, blue: medium, and yellow: longest surfactant.

We observe that as the number of surfactants in the system increases, it becomes increasingly more difficult for the NPs to orient in the same way, because multiple orientations become possible, and therefore grains appear in the system.

7.2.1. Assembly of patchy particles on a fixed hexagonal lattice

To facilitate the assembly of the NPs, we fixed them to points in a hexagonal lattice defined by the diameter of the NPs. The particles were not treated as rigid bodies, meaning that the tails and heads of the surfactants were allowed to move freely (although they remained constrained to their spherical gold shell). The interactions between surfactants were the same DPD interactions considered on Chapters 4 and 5. The results are shown in Figure 72. As expected, the patches of like surfactants aligned, with some defects arising for the ternary case shown in Figure 72b.

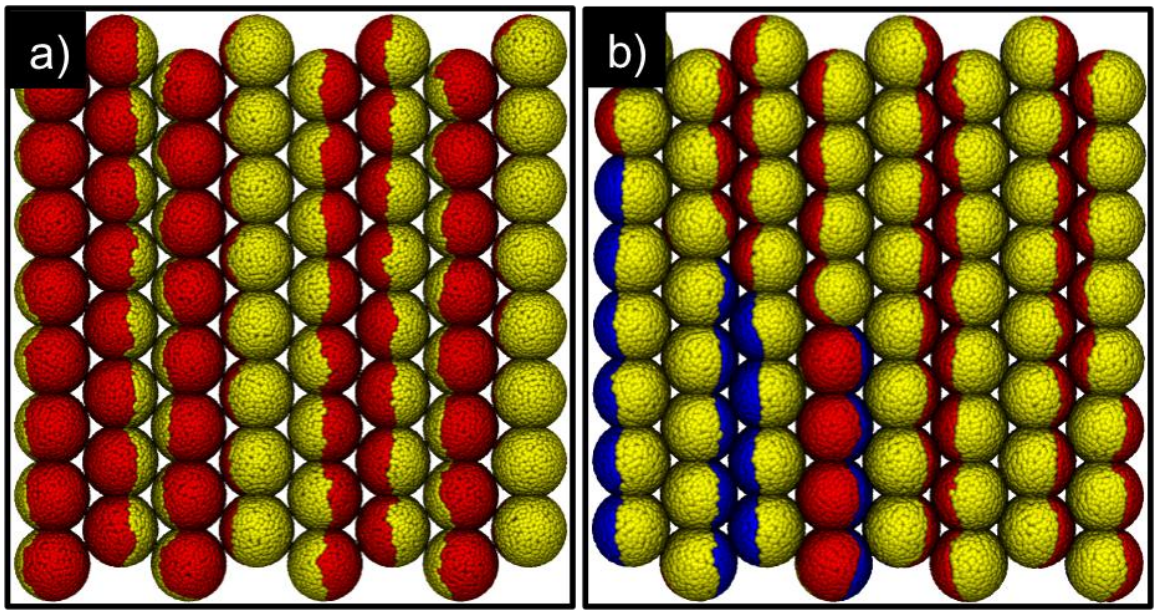

Figure 72 Assembly of 8x8 a) Janus and b) Cerberus NPs constrained to a two-dimensional interface and a hexagonal lattice. Tails not shown. Red: short, blue: medium, and yellow: longest surfactant.

Figure 72 shows a good improvement in the ordering of the NPs with respect to Figure 70. Having the NPs fixed on a lattice helps prevent some of the kinetic traps shown in Figure 71. However, the alignment of the NPs is not perfect (like the example shown in Figure 73a) because we are dealing with a single monolayer, so only the direct points of contact between them define their orientations. Because of the short-ranged nature of the DPD interactions used to simulate this system, configurations a and b shown in Figure 73 result in the exact same potential energy, because in both cases the yellow beads are far away enough from the red ones as to no interact with them. The third left-most NP shown in Figure 73b shows a possible configuration for the interaction between red beads. The force a configuration like the one shown in Figure 73a, it would be necessary to add additional layers of NPs on the z-direction.

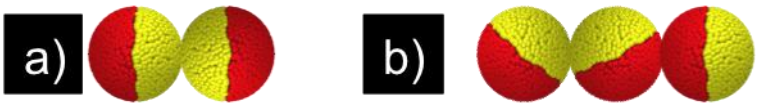

Figure 73 Possible orientations of the Janus NPs resulting in the same potential energy. Red: short, and yellow: longest surfactant. Tails not shown.

Having the patchy particles constrained to the hexagonal lattice allows for good and rapid alignment of the NPs, but ignores the shape effects that arise from the different lengths of the surfactants tails. To take these into account, we performed the simulations that we will discuss in the next section.

7.2.2. The effect of shape on the assembly of patchy particles

To take the shape anisotropy of the patchy particles into consideration, the patterned NPs were frozen into rigid bodies once more, and allowed to freely move inside a small box. The box dimensions were such that the NPs did not interact along the z-dimension, but they did on the other two through periodic boundary conditions. The same DPD interactions as in the previous sections were utilized for this system. The number of NPs in the system was limited by the available GPU memory, and simulations took 15 GPU hours to complete 30 million time-steps. The results are shown in Figure 74.

Figure 74 shows the assembly of Neapolitan (a) and Brahma (b) NPs that are modeled as rigid bodies in a two-dimensional interface. The assembly of the Neapolitan particles is in good agreement to the one observed in Figure 70b for a system in which the tails were not considered. In this case however, the addition of the tails in the simulation allows to improve the ordering of the NPs, which are aligned with much less defects than the ones seen in Figure 70b. The stripe formed by the short (red) surfactant is in this case aligned with the xy-plane, while the

patches of the medium length (blue) surfactant are all on the top side of the simulation. There is only one important defect towards the top of Figure 74a, in which one of the NPs is inverted with respect to the other showing the patch of the long (yellow) surfactant. The inclusion of the tails in the simulations allows to correct for the orientation defects discussed in Figure 71, and produces a much more precise orientation of the NPs.

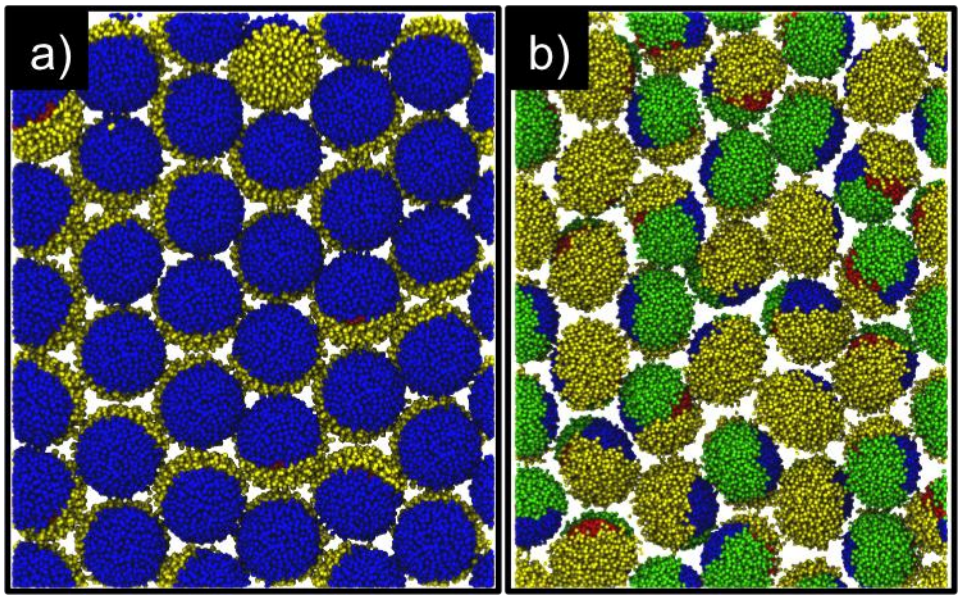

Figure 74 Assembly of 6x6 a) Neapolitan and b) Brahma NPs constrained to a two-dimensional interface. Red: short, blue: medium, green: long, and yellow: longest surfactant.

Figure 74b shows similar results but in this case for Brahma NPs. We see the formation of stripes of particles that are showing their longest (yellow) or second longest (green) surfactant patches on the top of the simulation. There are more defects in this case then there were for the Neapolitan particles of Figure 74a, but this is expected as it was noted earlier that increasing the number of surfactants increases the number of ways in which two particles can come together, and therefore increases the number of grain boundaries and defects in the system.

In Figure 74b we also see some frustration because of the competition between the interactions and the best packing due to the shape. Because of the interactions

between the four unlike surfactants, the preferred orientation of the NPs would be into a square lattice. However, because of the shape the NPs are forced into a hexagonal lattice to maximize the packing fraction of the system. This is an interesting effect due to the scale of the NPs. If this were a colloidal system, the coating would be so small compared to the size of the particles that it would not play an important role in their packing preference. However, in the nanoscale the particles become very fuzzy because the length of the coating is comparable to the length of the NPs, and therefore influences the way in which they want to pack.

7.3. Summary

In this chapter we simulated the self-assembly of multiple NPs constrained to a two-dimensional interface. We conducted these simulations for both Janus particles produced through crystallization of the long surfactants, and for patchy particles produced through different tail end groups. In both case we saw a prevalence of the closed-packed configuration expected for spherical NPs. The patches in the system guided the orientation of the NPs. In the case of patchy particle with sticky and repulsive points of interactions, constraining the NPs to a hexagonal lattice and taking into account the surfactant tails improved the assembly of the NPs. In both cases, the shape and composition of the monolayer played an important role in the packing of the NPs because of the similar length scales of the coating and the particles.

Chapter 8. Conclusions and outlook

In this chapter we summarize the contributions of this dissertation on the design rules and self-assembly of patterned NPs. We also present possible directions for future research exploiting the new ideas and findings derived from this work.

8.1. Contributions

In this dissertation work we used dissipative particle dynamics and molecular dynamics to study the self-assembled patterns that form on the monolayers of thiol-surfactants protected gold nanoparticles. We focused on understanding the effect of parameters like:

- curvature of the nanosurface (from small spherical nanoparticles to nanorods and flat surfaces),
- number of surfactants in the monolayer (from binary to quaternary mixtures),
- immiscibility between surfactants (from surfactants with the same end group to amphiphillic mixtures),
- length difference between surfactants,
- and stoichiometric composition of the monolayer.

These parameters can be easily controlled in experiments. For example, the synthesis method determines the geometry of the nanosurface.[102] The length of the surfactants can be changed by using longer hydrocarbon chains in the tails of the surfactants. The immiscibility is controlled by using different end groups for the alkane chain of the surfactants, *i.e.*, -CH_3, -OH, -COOH, etc. The number of surfactants

in the monolayer correspond to the number of surfactants in the initial solution used to stabilize the nanoparticles, and the stoichiometric composition is determined by the time allowed for the monolayers to equilibrate in solution. Therefore, the studies conducted in this thesis are useful guidelines for designing experiments to obtain the desired nanoscale patterns on the nanoparticles.

Our simulations of ternary and quaternary monolayers of surfactants revealed a large number of possible patterns. We identified six mayor families of patterns, all of which include multiple possible variations depending on the combination of parameters used. The patterns were verified by using different simulation methods (dissipative particle dynamics and molecular dynamics), and by changing the geometry of the nanosubstrate (spheres, cylinders and flat surfaces). Some of the patterns were analogous to previous results known both through simulations and experiments for binary monolayers, but most were novel patterns never observed before and unique to monolayers with more than two surfactants in them. The families of patterns presented in this thesis are as follows:

- Decorated striped patterns: These patterns are characterized by stripes in the system. They could be macrophase separated in which each surfactant forms one single stripe, forming three stripes (Neapolitan particles) or four stripes on the nanoparticle. Or they could be microphase separated patterns, in which multiple stripes are formed in the system. For binary systems, that consists in forming multiple simple stripes of both surfactants. For ternary systems, that means forming Alternating stripes, in which one surfactant forms one single stripe, which coils around the nanoparticle, and that stripe is decorated by a thinner stripe of the shortest surfactant to separate it from the longest surfactant.
- Decorated Janus patterns: The Janus patterns are characterized by the macrophase separation of two surfactants into two different hemispheres of the nanoparticle, diving the nanoparticle in half. The decorated Janus patterns occur when a third or forth surfactant are added to the system, and even though the Janus pattern remains, the additional surfactants for stripes on one or two sides

of the Janus. It can also occur when one of the sides of the Janus nanoparticle has alternating stripes, and the other side has simple binary stripes.

- Decorated Cerberus patterns: Similar to the Janus patterns, the Cerberus pattern corresponds to the macrophase separation of three surfactants on the nanoparticle. In this case, when a fourth surfactant is added it can form additional stripes in the system, for example just separating the three sides of the Cerberus, or forming stripes with one, two, or three of the other surfactants.
- Spotted patterns: These patterns occur for high stoichiometric ratios of one of the surfactants, usually the smallest one. Under these conditions, the surfactant that is present in the highest ratio forms a continuous matrix, and the other(s) surfactant(s) form 2D-micelles dispersed in said matrix.
- Tetrahedral patterns: This is one of the ways in which quaternary surfactants can macrophase separate on a monolayer. In this case, each surfactant shares an interface with all others. The top of the nanoparticle looks like a Cerberus pattern, and the fourth surfactant covers the bottom of the nanoparticle, in a tetrahedral configuration.
- Brahma patterns: This is the second way in which quaternary surfactants macrophase separate. In this case, each surfactant occupies a different quadrant of the nanoparticle, therefore only sharing an interface with two other surfactants, but not with all three of them.

Tetrahedral and Brahma patterns could be further decorated by adding additional surfactants to the monolayer, following the same design rules that were identified in this dissertation for ternary and quaternary mixtures.

All the patterns discussed in this work arise from a competition between two driving forces: the immiscibility due to the different end groups of the surfactants, which drives them towards macrophase separation and minimizing the interface length between unlike surfactants; and the conformational entropy gains at interfaces due to the length differences between unlike surfactants, which drives them towards maximizing the interface length. A balance between these two

competing effects determines the pattern that will minimize the free energy of the system, and be therefore the preferred equilibrium pattern. In all cases, microphase separation occurs only when the entropic gains at interfaces are enough to compensate for the energetic penalties derived from creating such interfaces between immiscible surfactants.

Based on all the simulation parameters discussed earlier, we constructed phase diagrams for ternary and quaternary monolayers of surfactants. These phase diagrams show the robustness of the patterns and define the range in which each specific pattern is possible. They also allowed us to enumerate the design rules that guide the formation of the patterns. We used these design rules to choose combinations of parameters to form new patterns, and even predict the behavior of monolayers formed by mixtures of five surfactants.

Once the design space for ternary and quaternary monolayers was exhaustively explored, we introduced the concept of immiscibility through crystallization of monolayers of nanoparticles. This was the result of a direct collaboration with the experiments performed by the Stellacci group. In this case, we eliminated the different end groups as a source of immiscibility in the system by using surfactants with the same end group, $-CH_3$. Unlike previous studies though, the surfactants in this system had much larger length differences between them (at least six carbons), and were larger with respect to the nanoparticle size. We found that the longer surfactants were long enough to form a crystalline monolayer, while the shorter ones remained disordered following a behavior that was originally observed both on flat surface and in homoligand monolayers on nanoparticles. The surfactants therefore macrophase separated into a Janus nanoparticle, with one side formed by the ordered long surfactants, and the other by the disordered short surfactants.

We showed both through simulations and experiments that this phase separation was independent of nanoparticle size, stoichiometry ratio of the monolayer, and miscibility between surfactants (*i.e.*, even for different end groups, crystallization will be the driving force of the separation when the length differences are enough).

We showed that the separation only depends on the length difference between surfactants, requiring at least a six-carbon length difference to occur.

Finally, it was observed experimentally that these Janus nanoparticles arranged into a closed-packed configuration with clear orientation of the patterns when the nanoparticles were deposited into a Langmuir-Blodgett film. We were able to reproduce this behavior with our molecular dynamics simulations of multiple nanoparticles confined to a quasi-two dimensional surface. We showed how the attractive interactions between the nanoparticles were key in their assembly into an ordered configuration. We extended that study to other types of patterns, in which the attractive and repulsive patches due to different end groups could guide the assembly of the nanoparticles into different configurations.

8.2. Directions for future research

In this dissertation we presented an exhaustive discussion of the types of patterns available to this system, the parameters that should be considered both in experiments and simulations, and the design rules that guide the formation of such patterns. We also confirmed the formation of some of those patterns in flat surfaces and cylinders. However, we did not perform studied of similar monolayers on faceted particles, such as cubes, tetrahedrons, and other faceted polyhedra. Some preliminary studies exist for such geometries and extreme stoichiometric cases,[59] showing interesting behavior on the vertices between facets. Since there are no vertices in any of the geometries studied in this dissertation, we expect there to be some differences between the patterns formed on faceted surfaces and the patterns presented in this work. It will definitely be an interesting area of study in the future to further explore and understand the design rules of monolayers on faceted polyhedra.

Another interesting direction for this research to continue consists in performing all-atom solvent explicit simulations. So far, most of the work performed in this

system had been highly coarse-grained, and that has been enough to provide an initial guidance and explanation to the real experimental system. However, as the system complicates and we begin to understand better then interactions and the governing forces, it might become relevant to include more detailed and fully-atomistic studies. For examples, the crystallization of the ligands could have never been studied by using our highly simplified dissipative particle dynamics model. We could only reproduce the true behavior of our system through more complicated and detailed molecular dynamics simulations. Performing solvent explicit simulations might allow us to have a deeper understanding of the system. Some similar studies have already shown how the micropatterns affect the wetting behavior of the solvent,[90] some of its useful properties,[104] and even the shape of the monolayer depending on the type of solvent used.[49] However, no study so far has been performed to observe the self-assembly of the pattern with explicit solvent. So far, all explicit-solvent simulations of non-homoligand monolayers have used pre-assembled striped patterns that are not allowed to change during the course of the simulation. Therefore, reproducing known patterns using explicit solvent will be a novel and interesting study, not to mention modeling challenge due to high computational costs. But once a standard procedure for such simulations has been found, it will be interesting to study the interactions of the patterns with different solvents, and how the presence of the solvent guides the alignment and ordering of multiple nanoparticles.

Finally, it will also be interesting to study some of the lesser-known properties of patterned nanoparticles. For example, it was observed experimentally that the striped nanoparticles could go through cell membranes without disrupting them or damaging the cell,[56] offering great potential applications for directed drug delivery.[57] However, not much is understood about the interactions between the striped nanoparticles and the lipid bilayers of the cells. It is believed that the amphiphillic composition of the stripes resembles the structure of the lipid bilayer, and therefore plays an important role in allowing the translocation of the cell membrane without being trapped by endocytosis. Computational studies could

elucidate this phenomenon, and help in further studies towards targeted drug delivery.

To simulate the interactions between the striped nanoparticle and the cell membrane, even dissipative particle dynamics and united-atom molecular dynamics could prove to be useful tools. The formation of lipid bilayers has already been investigated,[105] as well as the interaction of nanoparticles with vesicles[106], engulfing of Janus nanoparticles by lipid bilayers,[107] interactions of nanorods with lipid bilayers,[108] and even the formation of bilayers and vesicles in the presence of nanoparticles with explicit solvent.[109] These studies show the usefulness of dissipative particle dynamics to create a simple but qualitatively accurate model of the interactions between patterned nanoparticles of different shapes with lipid bilayers in solvent. It would be interesting to extend this model to study the penetration of lipid bilayers by striped nanoparticles, showing the disruption of the membrane by the nanoparticle, and its later rearrangement once the nanoparticles are through. It could also be useful to observe the arrangement of multiple nanoparticles suspend inside the lipid bilayer, in which the nanoparticles are experimentally thought to exhibit a certain degree of long range ordering.

Bibliography

1. Glotzer, S.C., and Solomon, M. Anisotropy of building blocks and their assembly into complex structures. Nature Materials 6, pp. 557-562 (2007)
2. Wang, Y.; Wang, Y.; Breed, D.R.; Manoharan, V.N.; Feng, L.; Hollingsworth, A.D.; Weck, M.; Pine, D.J.; Colloids with valence and specific directional bonding. Nature 491, pp. 51-56 (2012)
3. Sacanna, S.; Irvine, W.T.M; Rossi, L., Pine, D.J. Lock and key colloids through polymerization-induced buckling of monodisperse silicon oil droplets. Soft Matter 7, pp. 1631-1634 (2011)
4. Rossi, L.; Sacanna, S.; Irvine, W.T.M.; Chaiking, P.M.; Pine, D.J.; Philipse, A.P. Cubic crystals from cubic colloids. Soft Matter 7, pp. 4139-4142 (2011)
5. Auyeung, E.; Cutler, J.I.; Macfarlane, R.J.; Jone, M.R.; Wu, J.; Liu, G.; Zhang, K.; Osberg, K.D.; Mirkin, C.A. Synthetically programmable nanoparticle superlattices using a hollow three-dimensional spacer approach. Nature Technology 7, pp. 24-28 (2012)
6. Zhang, Z., and Glotzer, S.C. Self-assembly of patchy particles. Nano Letters 4(8), pp. 1407-1413 (2004)
7. Hong, L.; Cacciuto, A.; Luijten, E.; Granick, S. Clusters of charged Janus spheres. Nano Letters 6(11), pp. 2510-2514 (2006)
8. Jackson, A.M., Myerson, J.W., and Stellacci, F. Spontaneous assembly of subnanometre-ordered domains in the ligand shells of monolayer-protected nanoparticles. Nature Materials 3, pp. 330-336 (2004)
9. Singh, C., Ghorai, P.K., Horsch, M.A., Jackson, A.M., Larson, R.G., Stellacci, F. and Glotzer, S.C. Entropy-mediated patterning of surfactant-coated nanoparticles and surfaces. Physical Review Letters 99, 226106 (2007)

10. Singh, C., Jackson, A.M., Stellacci, F., and Glotzer, S.C. Exploiting substrate stress to modify nanoscale SAM patterns. Journal of the American Chemical Society 131, pp. 16377-16379 (2009)
11. DeVries, G.A., Brunnbaur, M., Hu, Y., Jackson, A.M., Long, B., Neltner, B.T., Uzun, O., Wunsch, B.H., and Stellacci, F., Divalent metal nanoparticles. Science 315, pp. 358-361 (2007)
12. Ingram, R.S., Hostetler, M.J., and Murray, R.W. Poly-hetero-ω-functionalized alkanethiolate-stabilized gold cluster compounds. Jounral of the American Chemical Society 119, pp 9175-9178 (1997)
13. Hoogerbrugge, P.J., and Koelman, J.M.V.A. Simulating microscopic hydrodynamic phenomena with dissipative particle dynamics. Europhysics Letters 19 (3), pp. 155-160 (1992)
14. Español, P., and Warren, P. Statistical mechanics of dissipative particle dynamics. Europhysics Letters 30 (4), pp. 191-196 (1995)
15. Soddemann, T., Dünweg, B., and Kremer, K. Dissipative particle dynamics: A useful thermostat for equilibrium and nonequilibrium molecular dynamics simulations. Physical Review E 68, 046702 (2003)
16. Groot, R.D., and Madden, T.J. Dynamic simulation of diblock copolymer microphase separation. Journal of Chemical Physics 108 (20), pp. 8173-8724 (1998)
17. Jury, S., Bladon, P., Cates, M., Krishna, S., Hagen, M., Ruddock, N., and Warren, P. Simulation of amphiphilic mesophases using dissipative particle dynamics. Physical Chemistry Chemical Physics 1, pp. 2051-2056 (1999)
18. Prinsen, P., Warren, P.B., and Michels, M.A.J. Mesoscale simulations of surfactant dissolution and mesophase formation. Physical Review Letters 89 (14), 148302 (2002)
19. Wijmans, C.M., Smit. B., and Groot, R.D. Phase behavior of monomeric mixtures and polymer solutions with soft interaction potentials. Journal of Chemical Physics 114 (17), pp. 7644-7654 (2001)

20. Marsh, C.A., Backx, G., and Ernst, M.H. Static and dynamic properties of dissipative particle dynamics. Physical Review E 56 (2), pp. 1676-1691 (1997)
21. Español, P. Hydrodynamics from dissipative particle dynamics. Physical Review E 52(2), pp. 1734-1742 (1995)
22. Jorgensen, W.L., and Tirado-Reves, J. The OPLS force field for proteins. Energy minimizations for crystals of cyclic peptides and crambin. Journal of the American Chemical Society 110(6), pp. 1657-1666 (1988)
23. Jorgensen, W.L, Maxwell, D.S., and Tirado-Reves, J. Development and testing of the OPLS all-atom force field on conformational energetics and properties of organic liquids. Journal of the American Chemical Society 118(45), pp. 11225-11236 (1996)
24. Ghorai, P.K., and Glotzer, S.C. Molecular dynamics simulation study of self-assembled monolayers of alkane-thiol surfactants on spherical gold nanoparticles. Journal of Physical Chemistry C 111(43), pp. 15857-15862 (2007)
25. Jorgensen, W.L. Intermolecular potential functions and Monte Carlo simulations for liquid sulfur compounds. Journal of Physical Chemistry 90, pp. 6379-6388 (1986)
26. Nath, S.K.; Banaszak, B.J.; de Pablo, J.J. A new united atom force field for α-olefins. Journal of Chemical Physics 114(8), pp. 3612-3616 (2001)
27. Frenkel, D., and Smit, B. Understanding molecular simulations. Academic Press, pp.417-421 (1997)
28. Templeton. A.C., Wuelfing, W.P., and Murray, R.W. Monolayer-protected cluster molecules. Accounts of Chemical Research 33 (1), pp. 27-36 (2000)
29. Ryckaert, J.P., Ciccotti, G., and Berendsen, H.J.C. Numerical integration of the Cartesian equations of motion of a system with constraints: molecular dynamics of n-alkanes. Journal of Computational Physics, 23(3), pp. 327-341 (1997)
30. HOOMD-blue web page: http://codeblue.umich.edu/hoomd-blue

31. Anderson, J.A., Lorenz, C.D, and Travesset, A. General purpose molecular dynamis simulations fully implemented on graphics processing units. Journal of Computationl Physics 227(10), pp. 5342-5359 (2008)
32. Phillips, C.L., Anderson, J.A., and Glotzer, S.C. Pseudo-random number generation for Brownian Dynamics and Dissipative Particle Dynamics simulations on GPU devices. Journal of Computational Physics 230(19), pp. 7191-7201 (2011)
33. Nguyen, T.D., Phillips, C.L., Anderson, J.A. and Glotzer, S.C. Rigid body constraints realized in massively-parallel molecular dynamics on graphics processing units. Computer Physics Communications 182(11), pp. 2313-2307 (2011)
34. http://lammps.sandia.gov/
35. http://www3.imperial.ac.uk/ict/services/hpc/highperformancecomputing/documentation/applications/dl%20poly
36. Brust, M.; Kiely, C.J. Some recent advances in nanostructure preparation from gold and silver nanoparticles: a short topical review. Colloids and Surfaces A: Physicochemical and Engineering Aspects 202, pp. 175-186 (2002)
37. Jadzinsky, P.D.; Calero, G.; Ackerson, C.J.; Bushnell, D.A.; Kornberg, R.D. Structure of thiol monolayer-protected gold nanoparticle at 1.1Å resolution. Science 318, pp. 430-433 (2007)
38. Porter, M.D.; Bright, T.B.; Allara, D.L.; Chidsey, C.E.D. Characterization of n-alkyl thiol monolayers on gold by optical ellipsometry, infrared spectroscopy, and electrochemistry. Journal of the American Chemical Society 109, pp. 3559-3568 (1987)
39. Nuzzo, R.G; Allara, D.L. Adsorption of bifunctional organic disulfides on gold surfaces. Journal of the American Chemical Society 105, pp. 4481-4483 (1983)
40. Bain, C.D.; Troughton, E.B.; Tao, Y.T.l Evall, J.; Whitesides, G.M.; Nuzzo, R.G. Formation of monolayer films by the spontaneous assembly of organic thiols from solution onto gold. Journal of the American Chemical Society 111, pp. 321-335 (1989)

41. Hautman, J.; Klein, M.L. Simulation of a monolayer of alkyl thiol chains. Journal of Chemical Physics 91(80, pp. 4994-5001 (1989)
42. Siepmann, I.J.; McDonald, I.R. Monte Carlo studies of the properties of self-assembled monolayers formed by adsorption of CH3(CH2)15SH on the (111) surface of gold. Molecular Physics 79(3), pp. 457-473 (1993)
43. Hautman, J.; Klein, M.K. Microscopic wetting phenomena. Physical Review Letters 67(13), pp. 1763-1766 (1991)
44. Eustis, S. and El-Sayed, M.A. Why gold nanoparticles are more precious than pretty gold: Noble metal surface Plasmon resonance and its enhacement of the radiative and nonradiative properties of nanocrystals of different shapes. Chemical Society Reviews 35, pp. 209-217 (2006)
45. Sperling, R.A., Rivera Gil, P., Zhang, F., Zanella, M., and Parak, W.J. Biological applications of gold nanoparticles. Chemical Society Reviews 37, pp. 1896-1908 (2008)
46. Heiz, U., and Schneider, W.D. Nanoassembled model catalysts. Journal of Physics D: Applied Physics 33, pp. R85-R102 (2000)
47. Pyykkö, P. Theoretical chemistry of gold. Angewandte Chemie 43, pp. 4412-4456 (2004)
48. Jackson, A.M., Hu, Y., Silva, P.J., and Stellacci, F. From homoligand- to mixed-ligand-monolayer-protected metal nanoparticles: A scanning tunneling microscopy investigation. Journal of the American Chemical Society 128 (34), pp. 11135-11149 (2006)
49. Lane, J.M.; Grest, G.S. Spontaneous asymmetry of coated spherical nanoparticles in solution and at liquid-vapor interfaces. Physical Review Letters 104, pp. 235501(4) (2010)
50. Bain, C.D.; Whitesides, G.M. Correlations between weattability and structure in monolayers of alkenthiols adsorbed on gold. Journal of the American Chemical Society 110, pp. 3665-3666 (1988)
51. Mizutani, W.; Ishida, T.; Tokumoto, H. Monte Carlo simulation of phase-separated self-assembled films. Applied Surface Science 130-132, pp. 792-796 (1998)

52. Bain, C.D.; Evall, J.; Whitesides, G.M. Doemation of monolayers by the coadsorption of thiols in gold – variation in the head group, tail group and solvent. Journal of the American Chemical Society, 111 (18), pp. 7155-7164 (1989)
53. Folkers, J.P.; Laibinis, P.E.; Whitesides, G.M.; Deutch, J. Phase-behavior of 2-component self-assembled monolayers of alkanethiols on gold. Journal of Physical Chemistry 98 (2), pp. 563-571 (1994)
54. Centrone, A., Hu, Y., Jackson, A.M., Zerbi, G., and Stellacci, F. Phase separation on mixed-monolayer-protected metal nanoparticles: A study by infrared spectroscopy and scanning tunneling microscopy. Small 3, pp. 814-817 (2007)
55. DeVries, G.A., Talley, F.R., Carney, R.P, and Stellacci, F. Thermodynamic study of the reactivity of the two topological point defects present in mixed self-assembled monolayers on gold nanoparticles. Advanced Materials 20, pp. 4243-4247 (2008)
56. Verma, A., Uzun, O., Hu, Y., Hu, Y., Han, H.S., Watson, N., Chen, S., Irvine, D.J., and Stellacci, F. Surface-structure-regulated cell-membrane penetration by monolayer-protected nanoparticles. Nature Materials 7, pp. 588-595 (2008)
57. Xia, T., Rome, L., and Nel, A. Particles slip cell security. Nature Materials 7, pp. 519-520 (2008)
58. Singh, C. Computational studies of surfactant self-assembly on nanostructured surfaces. Thesis (2010)
59. Santos, A.; Millan, J.A.; Glotzer, S.C. Faceted patchy particles through entropy-driven patterning of mixed ligand SAMS. Nanoscale 4, pp. 2640-2650 (2012)
60. Carney, R.P., DeVries, G.A., Dubois, C., Kim, H., Kim, J.Y., Singh, C., Ghorai, P.K., Tracy. J.B., Stiles, R.L., Murray. R.W., Glotzer, S.C., and Stellacci, F. Size limitations for the formation of ordered striped nanoparticles. Journal of the American Chemical Society 130, pp. 798-799 (2008)
61. Pons-Siepermann, I.C.; Glotzer, S.C. Design of patchy particles using ternary self-assembled monolayers. Soft Matter 8, pp. 6226-6231 (2012)
62. Pons-Siepermann, I.C.; Glotzer, S.C. Design of patchy particles using quaternary self-assembled monolayers. ACS Nano 6 (5), pp. 3919-3924 (2012)

63. Daniel, M.C.; Astruc, D. Gold Nanoparticles: Assembly, supramolecular chemistry, quantum-size-related properties, and applications toward biology, catalysis, and nanotechnology. Chemical Reviews 104, pp. 293–346 (2004)
64. Wynne, J.H.; Lloyd, C.T.; Cozzens, R.F. Synthesis of colloidal gold, silver, and cadmium coating block polymers. Abstract of Papers of the American Chemical Society 223, pp. U420-U420 (2002)
65. Pfau, A.; Sander, R.; Kirsch, S. Orientational ordering of structured polymeric nanoparticles at interfaces. Langmuir 18, pp. 2880-2887 (2002)
66. Cayre, O.; Paunov, V.N. ; Velev, O.D. Fabrication of asymmetrically coated colloid particles by microcontact printing techniques. Journal of Materials Chemistry 13, pp. 2445-2450 (2003)
67. Lu, Y.; Xiong, H.; Jiang, X.; Xia, Y. Asymmetric dimers can be formed by dewetting half-shells of gold deposited on the surfaces of spherical oxide colloids. Journal of the American Chemical Society 125, pp. 12724-12725 (2003)
68. Wooley, K.L.; Hawker, C.J.; Frechet, J.M.J. Unsymmetrical 3-dimensional macromolecules - Preparation and characterization of strongly dipolar dendritic macromolecules. Journal of the American Chemical Society 115, pp. 11496-11505 (1993)
69. McIntosh, C.M; Espostio, E.A; Boal, A.K.; Simard, J.M; Martin, C.T.; Rotello, V.M. Inhibition of DNA transcription using cationic mixed monolayer protected gold clusters. Journal of the American Chemical Society 123, pp. 7626-7629 (2001)
70. Gu, H.W.; Yang, Z.M.; Gao, J.H.; Chang, C.K.; Xu, B. Heterodimers of nanoparticles: Formation at a liquid-liquid interface and particle-specific surface modification by functional molecules. Journal of the American Chemical Society 127, pp. 34-35 (2005)
71. Pickering, S.U. Emulsions. Journal of the Chemical Society 91, pp. 2001-2021 (1907)
72. Binks, B.P.; Fletcher, P.D.I. Particles adsorbed at the oil-water interface: A theoretical comparison between spheres of uniform wettability and "Janus" particles. Langmuir 17, pp. 4708-4710 (2001)

73. Glaser, N.; Adams, D.J.; Boker, A.; Krausch, G. Janus particles at liquid-liquid interfaces. Langmuir 22, pp. 5227-5229 (2006)
74. Crossley, S.; Faria, J.; Shen, M.; Resasco, D.E. Solid nanoparticles that catalyze biofuel upgrade reactions at the water/oil interface. Science 327, pp. 68-72 (2010)
75. Takei, H.; Shimizu, N. Gradient sensitive microscopic probes prepared by gold evaporation and chemisorption on latex spheres. Langmuir 13, pp. 1865-1868 (1997)
76. Wang, Y.; Hernandez, R.M; Bartlett, D.J.; Bingham, J.M.; Kline, T.R.; Sen, A.; Mallouk, T.E. Bipolar clectrochemical mechanism for the propulsion of catalytic nanomotors in hydrogen peroxide solutions. Langmuir 22, pp.10451-10456 (2006)
77. Golestanian, R.; Liverpool, T.B.; Ajdari, A. Propulsion of a molecular machine by asymmetric distribution of reaction products. Physical Review Letters 94 (2005)
78. Salem, A.K.; Searson, P.C.; Leong, K.W. Multifunctional nanorods for gene delivery. Nature Materials 2, pp. 668-671 (2003)
79. Duguet, E.; Desert, A.; Perro, A.; Ravaine, S. Design and elaboration of colloidal molecules: an overview. Chemical Society Reviews 40, pp. 941-960 (2011)
80. Li, F.; Josephson, D.P.; Stein, A. Colloidal assembly: The road from particles to colloidal molecules and crystals. Angewandte Chemie-International Edition 50, pp. 360-388 (2011)
81. Perro, A.; Reculusa, S.; Ravaine, S.; Bourgeat-Lami, E.B.; Duguet, E. Design and synthesis of Janus micro- and nanoparticles. Journal of Materials Chemistry 15, pp. 3745-3760 (2005)
82. Lattuada, M.; Hatton, T.A. Synthesis, properties and applications of Janus nanoparticles. Nano Today 6, pp. 286-308 (2011)
83. Walther, A.; Muller, A.H.E. Janus particles. Soft Matter 4, pp. 663-668 (2008)
84. Hong, L.; Cacciuto, A.; Luijten, E.; Granick, S. Clusters of amphiphilic colloidal spheres. Langmuir 24, pp. 621-625 (2008)

85. Jiang, S.; Chen, Q.; Tripathy, M.; Schweizer, K.S.; Granick, S. Janus particle synthesis and assembly. Advanced Materials 22, pp. 1060-1071 (2010)
86. Yoon, J.; Lee, K.J.; Lahann, J. Multifunctional polymer particles with distinct compartments. Journal of Materials Chemistry 21, pp. 8502-8510 (2011)
87. Roh, K.H.; Martin, D.C.; Lahann, J. Biphasic Janus particles with nanoscale anisotropy. Nature Materials 4, pp. 759-763 (2005)
88. Hugonnot, E.; Carles, A.; Delville, M.H.; Panizza, P.; Delville, J.P. "Smart" surface dissymmetrization of microparticles driven by laser photochemical deposition. Langmuir 19, pp. 226-229 (2003)
89. Gangwal, S.; Cayre, O.J.; Velev, O.D. Dielectrophoretic assembly of metallodielectric Janus particles in AC electric fields. Langmuir 24, pp. 13312-13320 (2008)
90. Kuna, J.J.; Voitchovsky, K.; Singh, C.; Jiang, H.; Mwenifumbo, S.; Ghorai, P.K.; Stevens, M.M.; Glotzer, S.C.; Stellacci, F. The effect of nanometre-scale structure on interfacial energy. Nature Materials 8, pp. 837-842 (2009)
91. Miller, W.L.; Bozorgui, B.; Klymko, K.; Cacciuto, A. Free energy of alternating two-component polymer brushes on cylindrical templates. Journal of Chemical Physics 135 (2011)
92. Egorov, S.A. Microphase separation of mixed polymer brushes physisorbed on cylindrical surfaces. Soft Matter 8, pp. 3971-3979 (2012)
93. Singh, C.; Hu, Y.; Khanal, B.P.; Zubarev, E.R.; Stellacci, F.; Glotzer, S.C. Striped nanowires and nanorods from mixed SAMS. Nanoscale 3, pp. 3244-3250 (2011)
94. Kim, H.; Carney, R.P; Regurea, J.; Ong, Q.K.; Liu, X.; Stellacci, F. Synthesis and Characterization of Janus Gold Nanoparticles. Advanced Materials 24 (28), pp. 3857-3863 (2012)
95. Guarino, G.; Rastrelli, F.; Scrimin, P.; Mancini, F. Lanthanide-based NMR: a tool to investigate component distribution in mixed-monolayer-protected nanoparticles. Journal of the American Chemical Society (17), pp. 7200-7203 (2012)

96. Liu, X.; Yu, M.; Kim, H.; Stellacci, F. Determination of monolayer protected gold nanoparticles' ligand shell morphology via NMR. (In preparation).
97. Schreiber, F. Structure and growth of self-assembling monolayers. Progress in Surfacne Science 65, pp. 151-256 (2000)
98. Zheng, N.; Fan, J.; Stucky, G.D. One-step one-phase synthesis of monodisperse noble-metallic nanoparticles and their colloidal crystals. Journal of the American Chemical Society 128, pp. 6550-6551 (2006)
99. Harkness, K.M.; Balinski, A.; McLean, J.A.; Cliffel, D.E. Nanoscale phase segregation of mixed thiolates on gold nanoparticles. Angewandte Chemie-International Edition 50, pp. 10554-10559 (2011)
100. Ohara, P.C.; Leff, D.V.; Heath, J.R.; Gelbart, W.M. Crystallization of ppals from polydisperse nanoparticles. Physical Review Letters 75, pp. 3466-3469 (1995)
101. Chen, S.F.; Li, L.Y.; Boozer, C.L; Jiang, S.Y. Controlled chemical and structural properties of mixed self-assembled monolayers of alkanethiols on Au(111). Langmuir 16, pp. 9287-9293 (2000)
102. Ghosh, S.K. A model for the orientational order in liquid crystals. Il Nuovo Cimento D 4 (3), pp. 229-244 (1984)
103. Grzelczak, M.; Pérez-Juste, J.; Mulvaney, P.; Liz-Marzán, L.M. Shape control in gold nanoparticle synthesis. Chemical Society Review 37, pp. 1783-1791 (2008)
104. Cho, E.S.; Kim, J.; Tejerina, B.; Hermans, T.M.; Jiang, H.; Nakanishi, H.; Yu, M.; Patashinski, A.Z.; Glotzer, S.C.; Stellacci, F.; Grzybowski, B.A. Ultrasentive detection of toxic cations through changes in the tunnelling current across films of striped nanoparticles. Nature Materials 11, pp. 978-985 (2012)
105. Goetz, R.; Lipowsky, R. Computer simulations of bilayer membranes: Self-assembly and interfacial tension. Journal of Chemical Physics 108 (17), pp. 7397-7409 (1998)
106. Smith, K.A.; Jasnow, D.; Balazs, A.C. Designing synthetic vesicles that engulf nanoscopic particles. The Journal of Chemical Physics 127, p. 084703 (2007)
107. Alexeev, A.; Uspal, W.E.; Balazs, A.C. Harnessing Janus nanoparticles to create controllable pores in membranes. ACS Nano 2 (6), pp. 1117-1122 (2008)

108. Dutt, M.; Kuksenok, O.; Little, S.R.; Balazs, A.C. Forming transmembrane channels using end-functionalized nanotubes. Nanoscale 3, pp. 240-250 (2011)
109. Dutt, M.; Kuksenok, O.; Nayhouse, M.J.; Little, S.R.; Balazs, A.C. Modeling the self-assembly of lipids and nanotubes in solution: forming vesicles and bicelles with transmembrane nanotube channels. ACS Nano 5(6), pp. 4769-4782 (2011)